Charles University in Prague
Faculty of Mathematics and Physics

MASTER THESIS

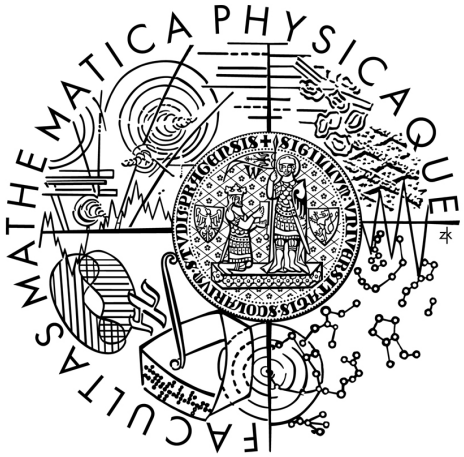

Vojtěch Witzany

Chaos in Deformed Black-Hole Fields

Institute of Theoretical Physics

Supervisor of the master thesis: Oldřich Semerák

Study programme: Physics

Specialization: Theoretical Physics

Prague 2015

I would like to thank my supervisor Oldřich Semerák for the numerous consultations and collaboration on the paper published along this thesis, for which I would also like to thank Petra Suková. I also appreciate the consultations on related topics with David Heyrovský, Georgios Lukes-Gerakopoulos, Emilio Tejeda and Jiří Podolský. Last but not least, I would like to thank my friends and family for their sustained support in the endeavour required for the writing of this thesis.

Access to computing and storage facilities owned by parties and projects contributing to the National Grid Infrastructure MetaCentrum, provided under the programme "Projects of Large Infrastructure for Research, Development, and Innovations" (LM2010005), is greatly appreciated. I am also grateful for support from the GAUK-2000314 and SVV-260211 grants.

I declare that I carried out this master thesis independently, and only with the cited sources, literature and other professional sources.

I understand that my work relates to the rights and obligations under the Act No. 121/2000 Coll., the Copyright Act, as amended, in particular the fact that the Charles University in Prague has the right to conclude a license agreement on the use of this work as a school work pursuant to Section 60 paragraph 1 of the Copyright Act.

In ..... date ..... signature of the author

Název práce: Chaos v polích deformovaných černých děr
Autor: Vojtěch Witzany
Katedra: Ústav teoretické fyziky
Vedoucí diplomové práce: doc. RNDr. Oldřich Semerák, DSc., Ústav teoretické fyziky

Abstrakt: Tato diplomová práce zkoumá dvě zásadní aproximace používané ve fyzice akrečních disků poblíž černých děr. První z těchto aproximací jsou efektivní „pseudo-newtonovské“ potenciály napodobující chování černé díry, které zkoumáme za pomoci numerických simulací i analytických metod. Druhá testovaná aproximace je zanedbání gravitace hmoty poblíž černé díry v akrečním procesu.

Nejdříve jsou diskutována témata jako integrabilita, rezonance a chaos, a poté je odvozena zcela obecná „pseudo-newtonovská“ limita geodetického pohybu. Tato limita je pak záhy použita na případ světelných geodetik v poli svítícího toroidu a na časupodobné geodetiky v Kerrově metrice. Dále je představen nový Newtonovský gravitační potenciál pro nesingulární toroidy a je diskutována jeho použitelnost v takzvaných Weylových prostoročasech. V poslední části je představen nový pseudo-newtonovský potenciál, který je pak s dalšími známými potenciály použit zcela analogicky jako v předchozích přesných relativistických studiích v modelech volného testovacího pohybu poblíž černé díry s diskem nebo prstencem; studované modely potvrzují předchozí závěry o chaosu v modelech disku/prstence a černé díry. Pseudo-newtonovský přístup dokáže reprodukovat řadu zásadních rysů původního relativistického systému, a silnější rozpory nastávají pouze jako důsledek extrémně silných nebo singulárních vnějších perturbací černé díry.

Klíčová slova: gravitace,relativita, černé díry, chaos, akreční disky

Title: Chaos in Deformed Black-Hole Fields
Author: Vojtěch Witzany
Department: Institute of Theoretical Physics
Supervisor: doc. RNDr. Oldřich Semerák, DSc., Institute of Theoretical Physics

Abstract: The consequences of two key approximations of accretion-disc physics near black holes are studied in this thesis. First, the question of effective “pseudo-Newtonian” potentials mimicking a black hole is investigated both through numerical simulations and analytical means, and second, the neglect of additional gravitating matter near accreted-upon black holes and its consequences are put to test.

After some broader discussion of integrability, resonance and chaos, a general ”pseudo-Newtonian” limit for geodesic motion is derived, and applied for the case of null geodesics near a glowing toroid and for time-like geodesics in the Kerr metric. Afterwards, a new Newtonian gravitational potential for non-singular toroids is proposed and its usefulness for the so-called Weyl space-times is discussed. Finally, a new pseudo-Newtonian potential is introduced and applied alongside already known potentials in models of free test particle motion in the field of a black hole with a disc or ring, in complete analogy with previous exact-relativistic studies, and the previous conclusion of chaos in disc/ring-hole models is confirmed. Overall, the pseudo-Newtonian framework is able to reproduce a number of key features of the original systems with notable differences arising only as a consequence of extremely strong or singular perturbation of the black hole.

Keywords: gravitation, relativity, black-hole physics, chaos, accretion discs

Contents

Introduction and outline

The onset of relativistic accretion-disc physics is best marked by the observation and confirmation of quasars, highly redshifted "quasi-stellar" sources brightly shining throughout the spectrum, more than fifty years ago. From the various explanations for quasars one victor has so far emerged; the source of radiation is a so-called active galactic nucleus, a particular system of matter inspiralling upon a black hole canonically described by models such as the α-prescription accretion disc of Shakura and Sunyaev (1973) or it's relativistic counterpart Novikov and Thorne (1973).

However, this black hole at a galactic centre powering the brightly shining quasar, and in general any astrophysical black hole, is not isolated. Various perturbations such as halos of faraway stars and gas, ring-like structures, or even the accretion disc itself may deform the gravitational fields of black holes found in various astrophysical situations. Such a deformation may not seem to be so significant to a local observer but may amass over long timescales into a notable effect for satellites orbiting the black hole; the result may be resonant or even chaotic motion. The consequences of such deformations on orbits near black holes have already been studied in literature (see Section 2.1 for a review), and particularly in the papers Semerák and Suková (2010, 2012); Suková and Semerák (2013), where the black hole was superposed with a gravitating disc or ring to observe the chaotization of geodesics. This thesis represents a continuation of the thread of research presented in the latter papers.

One of the tools often used to mimic astrophysical black holes in an accretion situation are the so-called pseudo-Newtonian potentials which, by a suitable modification of the usual Newtonian gravitational potential, are able to reproduce some of the essential features of motion in a black-hole space-time. Namely, the potentials usually reproduce the possibility of a black-hole in-fall (*not* possible in the case of a Newtonian potential), and an innermost stable circular orbit thus providing a natural inner edge of an accretion disc.

It is then interesting to study how a very loosely reconstructed dynamical system, such as the motion in the field of a pseudo-Newtonian potential superposed with a Newtonian gravitational potential of a disc or ring, can correspond to the original system, the geodesic motion in the exact space-time of a black hole with a disc or a ring. Is the mere reproduction of the positions of a few key orbits and an overall qualitative correspondence enough for a dynamical system to have the same properties under perturbation (the disc or ring)? Will the fine-tuned pseudo-Newtonian potentials work as well in a more general context than they were designed for? Surprisingly, the answer presented in this thesis is yes, at least for some of the potentials and in a loose and qualitative sense.

The secondary result of this thesis stumbled upon when thinking about some recently published results and when simply playing around with some potentials is the proposal of a new pseudo-Newtonian potential reproducing exactly the angular-momentum distribution of circular orbits in the Schwarzschild space-time, and even a completely general "pseudo-Newtonian framework" for motion in arbitrary space-times. The most effective pseudo-Newtonian potentials so far were only able to reproduce the properties of orbits of massive particles in the Schwarzschild metric; the new pseudo-Newtonian framework shows satisfactory properties for null geodesics in stationary space-times and produces a promising "pseudo-Kerr" dynamics corresponding to the motion in the field of

a spinning black hole.

The contents of this thesis represent more a set of loosely related investigations than a “monograph” of some kind. Concepts are introduced on the go and the structure is admittedly best characterized as a merged set of “work in progress” notes edited for a continuous tone.

The outline is the following. After some discussion and review of integrability, resonance and chaos in general systems in Chapter 1 and specifically in axially symmetric fields in Chapter 2, a general ”pseudo-Newtonian” limit for geodesic motion is derived in Chapter 3, and applied for the case of null geodesics near a glowing toroid and for time-like geodesics in the Kerr metric.

Afterwards, a review of the so-called Weyl space-times is given in Chapter 4 along with a new Newtonian gravitational potential for non-singular toroids; the usefulness of the toroid potential for Weyl space-times is discussed. Finally, in Chapter 6 a new pseudo-Newtonian potential is introduced and applied alongside already known potentials in models of free test particle motion in the field of a black hole with a disc or ring, in complete analogy with previous exact-relativistic studies, and the previous conclusion of chaos in disc/ring-hole model is confirmed.

1 Integrability and chaos

In this chapter we quickly develop a minimal treatment of non-integrability in Hamiltonian systems from the view-point of a gradually perturbed integrable system. We dare to define chaos only by non-integrability, even though the close-orbit divergence (a usual definition of chaos) has not been rigorously proven to be in undefiable connection with Hamiltonian non-integrability. Hence, in this chapter as in the whole text "non-integrability" is often used as a synonym of "chaoticity" without further comment.

1.1 Integrability

1.1.1 Integrable and hyperintegrable systems

In Hamiltonian systems, integrable trajectories are bound by either local or global integrals of motion into hypersurfaces in the phase space and when the number of integrals is exactly equal to the number of degrees of freedom of the system, the motion in the remaining phase space is diffeomorphic to a product of translations and rotations. However, when the number of integrals is *larger* than the number of degrees of freedom, the motion becomes rather restricted. The former of the statements is expressed mathematically as the Liouville-Arnold theorem (Arnold et al., 2007):

Let $\boldsymbol{M}, \boldsymbol{\omega}$ be a symplectic manifold of dimension $2n$ and $F_{(1)}, ...F_{(n)}$ functions on the manifold with linearly independent gradients and in pairwise involution

$$\{F_{(i)}, F_{(j)}\} \equiv \boldsymbol{\omega}(\mathrm{d}F_{(i)}, \mathrm{d}F_{(j)}) \equiv \omega^{lk}\partial_l F_{(i)}\partial_k F_{(j)} = 0, \ , \ \ i, j = 1...2n\,, \tag{1.1}$$

and let the flows of the vector fields $\omega^{lk}\partial_k F_{(i)}$ be complete (i.e. extendible to $\pm\infty$ in the time parameter). Then:

1. *Each of the flows $\dot{z}^l = \omega^{lk}\partial_k F_{(i)}$ is solvable by quadratures.*
2. *Each connected component of the hypersurfaces $\boldsymbol{M}_f = \{z \in \boldsymbol{M}, F_{(i)}(z) = f_{(i)}\}$ is diffeomorphic to a product of a k-dimensional torus and an $n-k$ dimensional real space $\mathbb{T}^k \times \mathbb{R}^{n-k}$ (and the motion is restricted to these hypersurfaces).*
3. *On every connected component of $\boldsymbol{M}_f$ there exist coordinates $\phi_1, ...\phi_k \bmod 2\pi,\ y_1, ..., y_{n-k}$ such that the equations of motion $\dot{z}^l = \omega^{lk}\partial_k F_{(i)}$ take form*

$$\dot{\phi}^m = \Omega^m_{(i)},\ \dot{y}_n = c^n_{(i)},\ \ (\Omega, c = \text{const. on } \boldsymbol{M}_f). \tag{1.2}$$

Since we are interested only in bound systems, we will concern ourselves mainly with the case of $\boldsymbol{M}_f \sim \mathbb{T}^n$; this set of $\boldsymbol{M}_f$ hypersurfaces (topological tori) will be called a Liouville foliation. The coordinates $\phi_1, ..., \phi_n$ along with their canonical conjugates $I_1, ..., I_n$ (for which $\dot{I} = 0$) are then usually called action-angle coordinates.

The motion on the $\sim \mathbb{T}^n$ hypersurfaces is generally quasi-periodic, i.e. the frequencies Ω^m are not necessarily commensurate and, as a consequence, the trajectory usually densely winds the torus. However, when Ω^m vary in a smooth and non-degenerate way throughout the different hypersurfaces M_f, there is necessarily a dense set of periodic trajectories (cases where the frequencies Ω^m are commensurate). The tori wound by periodic trajectories are then often called *resonant tori*.

It is not possible to have more than n pairwise commuting independent integrals of motion in a system with n degrees of freedom (Arnold, 1989) but it is possible to have more than n integrals of motion which are linearly independent. A system for which there are two gradient-distinct sets of n pairwise commuting independent integrals of motion is called a multi-integrable or hyperintegrable[1] dynamical system.

Since there are two distinct complete sets of integrals of motion, there are also two distinct Liouville foliations of the phase space. However, as the trajectory must fall in both of these foliations, it is necessarily restricted to a smaller subspace than $\sim \mathbb{T}^n$. The only way the trajectory can perform an n-dimensional rotation in a smaller-dimensional space is when the motion is periodic in some subspace. Hence, multi-integrable systems are characterized by (partially) periodic trajectories degenerately spanning the phase space.

For example in the case of a 3D isotropic harmonic oscillator one can introduce a Liouville foliation based on spherical coordinates and the spherical symmetry of the system, or a Liouville foliation based on Cartesian coordinates in which every direction is treated as an independent harmonic oscillator. A third type of Liouville foliation is obtained by using the cylindrical symmetry of the system around any axis which separates the system into a 2D and 1D harmonic oscillator. Even though a naive interpretation of the Liouville-Arnold theorem would suggest that the oscillations will be densely winding $\sim \mathbb{T}^3$ in phase space, the motion will be in fact strictly periodic and bound to a loop $\sim \mathbb{T}^1 \equiv S^1$ due to the mentioned degeneracy.

1.1.2 Geometric interpretation of integrability

The question of integrability can be made analogous to finding a potential of a vector field by noting that the Poisson bracket can be in fact expressed as a "symplectic differential product" with the "metric" ω^{ij}. When the coordinates on the phase space are canonical momenta and coordinates (p_i, q_i), the symplectic metric $\boldsymbol{\omega}$ reads

$$\omega^{ij} = \begin{pmatrix} 0_n & -\mathbb{1}_n \\ \mathbb{1}_n & 0_n \end{pmatrix}, \tag{1.3}$$

where we keep the indices in the notation to make clear the distinction between ω^{ij} and it's inverse ω_{ij}.

Once a set of k pairwise Poisson-commuting integrals of motion $G_{(1)}, ..., G_{(k)}$ is found, one is then looking for a differential 1-form $\boldsymbol{\alpha}$ so that

$$\omega^{ij}\alpha_i\partial_j G_{(l)} = 0\,,\ l = 1...k\,,\ \boldsymbol{\alpha} \notin \mathrm{span}(\mathrm{d}G_{(1)}, ..., \mathrm{d}G_{(k)})\,,\ \mathrm{d}\boldsymbol{\alpha} = 0\,. \tag{1.4}$$

That is, the form $\boldsymbol{\alpha}$ is "symplectic-orthogonal" to the known integrals of motion and linearly independent from them which restricts it into a $2n - 2k$-dimensional fibre at every point of the phase

[1] However, the term *hyperintegrable* or *superintegrable* is often used for a system with $> n$ independent integrals of motion which are not necessarily pairwise commuting (Miller Jr et al., 2013).

space. A form fulfilling all the stated conditions on some hypersurface of constant $G_{(1)}, ..., G_{(k)}$ can then be integrated to obtain a local integral of motion.

On the other hand, the motion is non-integrable when no such $\boldsymbol{\alpha}$ can be found along the given hypersurface. For example, in the case of an autonomous Hamiltonian system with two degrees of freedom there is one integral "for free", the Hamiltonian H, and the form $\boldsymbol{\alpha}$ corresponding to another possible integral of motion is then restricted to 2-dimensional fibres in the tangent bundle of the phase space. Consequently, the condition that an integral-generating form has to satisfy $\mathrm{d}\boldsymbol{\alpha} = 0$ is analogous to the requirement that a potential vector field $\vec{V}$ on a 2-dimensional plane has to satisfy $\mathrm{curl}\vec{V} = 0$.

By analogy, this argument might lead us to the conclusion that autonomous Hamiltonian systems with two degrees of freedom will be always integrable since we can always choose a two-dimensional potential vector field $\vec{V}$ in the plane. However, the topological structure of the restricted fiber bundle on the surfaces of constant $G_{(1)}, ..., G_{(k)}$ might be non-trivial thus allowing no form $\boldsymbol{\alpha}$ fulfilling the given conditions.

1.1.3 Near-integrability

Physical effects often cause a dynamical system to possess a high degree of symmetry which, however, is approximate. An often frugal approach is to idealize the symmetries to perfection and introduce the imperfection perturbatively. Nonetheless, the zero-perturbation limit of the phase space structure my be ill-convergent. Generally, the effects of a smooth perturbation of an analytical non-degenerate system are $\mathcal{O}(\sqrt{\epsilon})$, where ϵ is the dimensionless perturbation parameter. I.e., in certain cases the effects of a small dynamical perturbation are "stronger" than linearised ($\mathcal{O}(\epsilon)$).

The formal statement of these facts is given by the Kolmogorov-Arnold-Moser (KAM) theorem which can be found e.g. in Arnold et al. (2007) along with a proof or in Lowenstein (2012). Nevertheless, the theorem addresses only analytical Hamiltonians with sufficiently smooth perturbations. In the case of our study, the motion directly encounters non-smooth perturbations and the strict applicability of the theorem is broken. Hence, instead of giving the full-fledged theorem, the perturbation-theory techniques used for it's constructive proof will be sketched and their failure in the case of resonances discussed.

We consider the simplest and historical perturbation method of Lindsted as reformulated and summarized by Poincaré (1899). The perturbation problem is formulated as solving the equations of motion of the Hamiltonian[2]

$$H(p,q) = H_0(p,q) + \epsilon P(p,q,\epsilon)\,, \tag{1.5}$$

where $P(p,q,\epsilon)$ is a quantity of order $\mathcal{O}(\epsilon^0)$. The main idea of the majority of canonical perturbation techniques is to transform the system into the action-angle coordinates J, ϕ of the unperturbed system (yielding $H_0 = H_0(J)$) and performing a series of perturbative canonical transformations to the action-angle variables of the perturbed system. We are thus looking for a transformation $J, \phi \mapsto I, \psi$ given by a generating function $S(I,\phi)$ so that

$$J = I + \epsilon\frac{\partial S}{\partial \phi}\,,\ \psi = \phi + \epsilon\frac{\partial S}{\partial I}\,, \tag{1.6}$$

$$S(I,\phi,\epsilon) = S_1(I,\phi) + \epsilon S_2(I,\phi) + ..., \tag{1.7}$$

$$\mathcal{H}(I,\epsilon) = \mathcal{H}_0(I) + \epsilon\mathcal{H}_1(I) + ... \tag{1.8}$$

[2]Indices indicating multiple coordinates are suppressed throughout this subsection.

Equating terms of same order in ϵ we obtain an infinite set of linear equations whose one particular solution is

$$\mathcal{H}_0 = H_0(I),\ \mathcal{H}_1 = \langle P\rangle_\phi,\ S_1 = -\{P\}_\phi, \tag{1.9}$$

$$\mathcal{H}_j = \langle F_j\rangle^\phi,\ S_j = -\{F_j\}_\phi,\ \ j \geq 2, \tag{1.10}$$

where F_j is a polynomial in $\partial S_1/\partial\phi, ..., \partial S_{j-1}/\partial\phi$ and $\langle\cdot\rangle_\phi, \{\}_\phi$ are the so-called averaging and integration operator. The averaging operator is simply defined as the average over the unperturbed Liouville torus

$$\langle f\rangle_\phi(J) = \int_{\mathbb{T}} f(J,\phi)\,\mathrm{d}\phi \tag{1.11}$$

and the integration operator is the solution to the equation

$$\left(\partial_\phi\{f\}_\phi\right)\cdot\Omega = f - \langle f\rangle_\phi, \tag{1.12}$$

where Ω is the frequency vector on the unperturbed Liouville torus $\Omega \equiv \partial H_0/\partial J$. The integration operator has a formal solution if we expand f into Fourier coefficients

$$f(I,\phi) = \sum_k \exp(\mathrm{i}k\cdot\psi) f^{(k)}(j), \tag{1.13}$$

where k are integer vectors and one can easily see that $f^{(0)} = \langle f\rangle_\phi$. Then the integration operator formally reads

$$\{f\}_\phi = \sum_{k\neq 0} \frac{f^{(k)}(J)}{k\cdot\Omega}\exp(\mathrm{i}k\cdot\psi). \tag{1.14}$$

However, the integration operator has no solution for cases when there is some k such that $k\cdot\Omega$ is zero and the coefficient $f^{(k)}(J)$ is non-zero. Hence, in the general case the formal solution in equations (1.9), (1.10) does not exist on a dense subset of the phase space. The problem of small $k\cdot\Omega$ is called the *small divisor* or *small denominator* problem.

For a good meaning of the formal Lindsted series, one first needs to expand the perturbation term into a Fourier series grouped by absolute magnitude of terms

$$\epsilon P(J,\phi,\epsilon) = P^{(1)}(J,\phi,\epsilon) + P^{(2)}(J,\phi,\epsilon) + ..., \tag{1.15}$$

where $P^{(i)}$ is a trigonometric polynomial in the ϕ-Fourier expansion which is bound by a quantity of order ϵ^i. The connection between the smallness of $P^{(i)}$ and ϵ can be mostly understood as a purely formal identification possible due to the smallness of the higher order Fourier coefficients for a smooth P. Then, including only terms of order ϵ^i in every iteration of the canonical transformation (1.9), (1.10), the solution fails only on a finite subset of the phase space in every iteration and the whole perturbative method does not break down.

Lindsted's method has a convergence rate as $\sim \epsilon^{m+1}$ for an m-th iterate of the canonical transformation and diverges in the general case. The methods of KAM theory are very similar to the Lindsted series but employ a few tricks to achieve superconvergence as $\sim \epsilon^{2^m}$ with the m-th iterate. Along with some smoothness and non-degeneracy conditions, the KAM methods are able to prove convergence of the iterations on the phase space up to an $\mathcal{O}(\sqrt{\epsilon})$ patch of the phase space. These small patches are then the resonances where the small denominator problem redefines the phase-space structure (see next subsection).

Hence, one can understand the problem of a non-smooth perturbation as a problem of large high-order coefficients of it's Fourier expansion. We know that for a C^k function the asymptotic behaviour of it's nth Fourier coefficients for large n is bound by $\sim n^{-(k+1)}$ and for C^∞ the decay is faster than any polynomial. In our case the perturbation will be discontinuous (the disc) and with a logarithmic singularity (the ring) which cannot be guaranteed to have any kind of reasonable Fourier-coefficient decay. Thus, it can be expected that the non-smooth perturbations will, even for very small perturbation strengths, create a relatively large number of resonances of non-negligible size. Furthermore, the $\mathcal{O}(\sqrt{\epsilon})$ behaviour might be broken in some cases and even "wilder" dependence on parameters might be observed.

Apart from the small regions of discontinuity or singularity, however, the perturbations will be C^∞ and the somewhat predictable evolution of phase space under growing perturbation is to be expected. Hence, observing closely which of the tori intersect the non-smooth parts of the perturbation and which do not will be an important part of the qualitative analysis.

1.2 Resonance and chaos

1.2.1 Resonant layer

In this subsection we loosely follow the treatment of Zaslavsky (2008) to demonstrate the nature of resonances. The example we choose is a system with two degrees of freedom of which, however, one is degenerate before perturbation. This is typically the case of the so-called 1.5 degrees of freedom systems where a system, such as a non-linear oscillator, with one degree of freedom is subject to a time-dependent perturbation ("kick"). Nevertheless, the same formal treatment as will be introduced here can be, at least to linear order, applied to a system with spherical symmetry under an axially symmetric perturbation.

Let I, ϕ be the action-angle variables of the original unperturbed degree of freedom, θ a 2π-periodic coordinate of the newly activated degree of freedom and L the momentum conjugate to θ. At least to linear order in perturbation, it is then always possible to time-reparametrize the trajectories so that $\dot{\theta} = 1$ (see Section 2.2 in next chapter for details). Hence, we consider the following simple Hamiltonian[3]

$$H(I, \phi, \theta, \epsilon) = H_0(I) + L + \epsilon V(I, \phi, \theta). \tag{1.16}$$

Since ϕ and θ are both periodic, we can Fourier expand V as

$$V(I, \phi, \theta) = \frac{1}{2} \sum_{k,l} V_{k,l} e^{\mathrm{i}k\theta + \mathrm{i}l\phi}, \tag{1.17}$$

where $V^*_{k,l} = V_{-k,-l}$. The equations of motion for I, ϕ then read

$$\dot{I} = -\epsilon \frac{\partial V}{\partial \phi} = \frac{\mathrm{i}\epsilon}{2} \sum l V_{k,l} e^{\mathrm{i}k\theta + \mathrm{i}l\phi}, \tag{1.18}$$

$$\dot{\phi} = \frac{\partial H_0}{\partial I} + \epsilon \frac{\partial V}{\partial I} = \Omega_\phi(I) + \frac{\epsilon}{2} \sum \frac{\partial V_{k,l}}{\partial I} e^{\mathrm{i}k\theta + \mathrm{i}l\phi}, \tag{1.19}$$

$$\dot{\theta} = \frac{\partial H_0}{\partial L} = \Omega_\theta(I, L) \tag{1.20}$$

[3] Note that the perturbation has no non-linear dependence on ϵ and no dependence on L, it is thus a "linearly superposed external potential".

where $\Omega \equiv \partial H_0/\partial I$ is the unperturbed frequency. Now consider a certain I_0 for which the resonance condition $k_0\Omega(I_0) + l_0 = 0$ holds for certain k_0 and l_0. We rewrite the equations of motion in the form

$$\dot{I} = \epsilon l_0 V_0 \sin(k_0\theta + l_0\phi + \varphi) + \sum_{k\neq\pm k_0,\, l\neq\pm l_0} \ldots , \tag{1.21}$$

$$\dot{\phi} = \Omega(I) + \epsilon\frac{\partial V_0}{\partial I}\cos(k_0\theta + l_0\phi + \varphi) + \sum_{k\neq\pm k_0,\, l\neq\pm l_0} \ldots , \tag{1.22}$$

where $V_0 \equiv |V_{k_0,l_0}|$ and $\varphi = \arg V_{k_0,l_0}$ and we have taken out the resonant $k = \pm k_0$, $l = \pm l_0$ from the sum. As sketched in the last subsection, the terms for which the resonance condition does not hold can be eliminated by an iterative averaging procedure but at the resonance the resonant mode will become dominant and cannot be averaged out. We will thus drop the non-resonant terms and study only the proximity of I_0.

Now consider the linearisation $I(t) = I_0 + \Delta(t)$, $\Omega(I) \approx \Omega(I_0) + \Omega'\Delta(t)$ and the "co-moving phase" $\psi = k_0\theta + l_0\phi + \varphi$. The meaning of ψ is the angle-deviation from a particular trajectory on the resonant orbit. With the application of the resonance condition, the equations of motion can be rearranged as

$$\dot{\Delta} = \epsilon l_0 V_0 \sin\psi \,, \tag{1.23}$$

$$\dot{\psi} = l_0\Delta\Omega' + \epsilon\frac{\partial V_0}{\partial I}\cos\psi \,. \tag{1.24}$$

Now taking a time derivative of equation (1.24), substituting from both (1.23) and (1.24), and keeping only $\mathcal{O}(\Delta, \epsilon)$ terms, we obtain the following equation of motion

$$\ddot{\psi} = \epsilon l_0^2 V_0 \Omega' \sin\psi \,, \tag{1.25}$$

which is the equation of motion of a non-liner harmonic oscillator. The width of the resonance can be defined as the maximum Δ on the separatrix of the non-linear oscillation, which can be easily found as

$$\Delta_s = \sqrt{\frac{2\epsilon V_0}{\Omega'}} \,. \tag{1.26}$$

It should be noted that this estimate is not fully rigorous because if $\Delta \sim \sqrt{\epsilon}$ then we should not be able to neglect $\sim \Delta^2$ terms and keep $\sim \epsilon$ ones. However, even under these considerations the stated resonance width (1.26) would be the leading order contribution.

We can see from equation (1.26) that the resonance width is indeed $\mathcal{O}(\sqrt{\epsilon})$ and this will be the portion of the phase space impossible to cover with the torus-deformation process. Another interesting fact is that the resonance width goes as $1/\sqrt{\Omega'}$. In the case of a degenerate frequency spectrum we have $\Omega' \to 0$ and Δ cannot be treated in a perturbative mode. Hence, the frequency gradient Ω' can be understood as a certain "stiffness" of the dynamical system with respect to resonances. From this argument it is clear why does the KAM theorem need additional conditions on the non-degeneracy of Ω.

The qualitative picture of the resonance in the p, q section (corresponding to I, ϕ) is shown in figure 1.1. The coordinate ψ makes l_0 full loops when circling around $\phi \in [0, 2\pi)$ and would make k_0 full loops for $\theta \in [0, 2\pi)$ in a different section. Hence, we see l_0 copies of the "co-moving" non-linear harmonic oscillator from eq. (1.25) in the section with l_0 saddle points and l_0 stable equilibria.

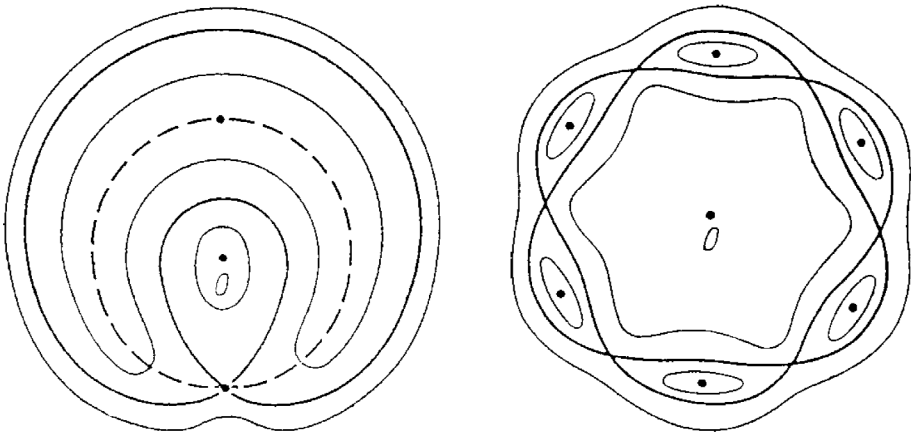

Figure 1.1: A sketch of a surface of section through resonant tori. The sketch shows a k:($l = 1$) resonance on the left and a k:($l = 6$) resonance on the right. However, it is impossible to read off k from the surface of section. (Taken from Zaslavsky (2008).)

The l_0 copies of a stable equilibrium correspond, in fact, to a single stable periodic trajectory and each of the l_0 copies of the unstable hyperbolic point correspond to a single unstable orbit.

Only one of the resonance-integers is possible to read off from a surface of section and the other one must be obtained by either a different section or some other tools. Furthermore, in the case of an additional discrete symmetry of the phase space, the "read-off" can be presented with some other difficulties, see Section 2.3 in the next chapter.

1.2.2 Homoclinic tangle and chaos

So far, the discussion only addressed the question of resonances and not chaos. Here, only a brief informal discussion of chaos generating mechanisms will be given and the reader may find more in the textbooks of Zaslavsky (2008), Haller (2012), or from a wider introductory viewpoint, in Alligood et al. (1997) and Hirsch et al. (2004).

Hamiltonian chaos is associated mainly with unstable equilibria and their stable and unstable manifolds. A stable manifold is a hypersurface in the phase space which tends to the equilibrium as $t \to \infty$ and the unstable manifold is a hypersurface which tends to the equilibrium as $t \to -\infty$. Under a perturbation these two manifolds may transversally intersect and create a so-called homoclinic point.

To understand the importance of homoclinic points consider a Poincaré surface of section[4] of an autonomous dynamical system with two degrees of freedom and the hyperbolic equilibrium as an unstable periodic trajectory. The stable and unstable manifolds are then represented as lines on the surface of section and the homoclinic intersection as a point (cf. the separatrices in figure 1.1).

The property of being on a stable or an unstable manifold is by definition invariant under the time-flow of the system and thus is the stability or instability of the points under the iterations of

[4] A Poincaré surface of section is a surface in phase space which is intersected an infinite number of times by every bound trajectory in the system. The successive intersections of a given trajectory with the surface may be understood as a Hamiltonian map.

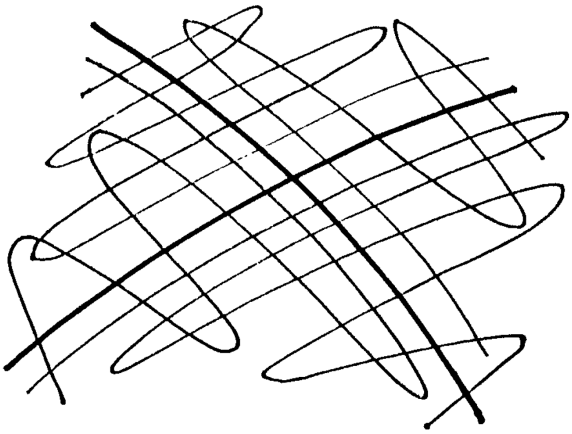

Figure 1.2: A sketch of a homoclinic tangle. The bold lines represent the original unperturbed stable/unstable manifolds asymptotically converging to the equilibrium at their crossing. The wiggly thin lines then represent the stretched and folded manifolds forming the "tangle" once a transversal intersection is induced by a perturbation. (Taken from Zaslavsky (2008).)

the Poincaré surface of section. The homoclinic point on the surface of section is by definition not fixed or periodic and it's every Poincaré-surface iterate corresponds to another intersection of the lines representing the stable and unstable manifolds. Hence, there must be an infinite number of homoclinic points implied by the single one. The corresponding structure of infinitely tangled stable and unstable manifolds is illustrated in fig. 1.2.

Another kind of tangle is a heteroclinic tangle which differs from the homoclinic tangle only in the fact that it is formed by an intersection of stable and unstable manifolds of *different* unstable equilibria.

Most of the unstable equilibria responsible for chaos are usually formed only after perturbation in the form of unstable periodic trajectories in resonances, but sometimes unstable equilibria are present in the dynamical system beforehand. That is because when the system changes between two types of motion, it will necessarily have a singularity in the Hamiltonian $\mathrm{d}H = 0$, an equilibrium of a certain type. The different types of motion are then separated by a so-called separatrix, a stable or unstable manifold associated with the $\mathrm{d}H = 0$ point. In consequence, systems with such singularities and more than one type of motion will usually be more prone to become chaotic.

A particularly important example of "beforehand" unstable equilibria are the unstable circular orbits near black holes. There, the unstable circular orbit is a marker between bound motion or scattering near the black hole and a plunge-in into the event horizon. The homoclinic orbit then corresponds to a limit of an infinite "whirl-zoom" winding of the centre (infinitesimally close to the unstable circular orbit) or a diverging pericenter phase.

So far, only weak perturbation and chaos were discussed. In weak chaos, only thin layers of irregularity around hyperbolic equilibria and their stable/unstable manifolds emerge. As a consequence, chaotic trajectories stick very closely to regular trajectories in phase space and cannot be easily discerned from regular ones by short-term observations. The onset of strong chaos is then usually conventionally defined (Zaslavsky, 2008; Contopoulos, 2002) as the moment when two such layers

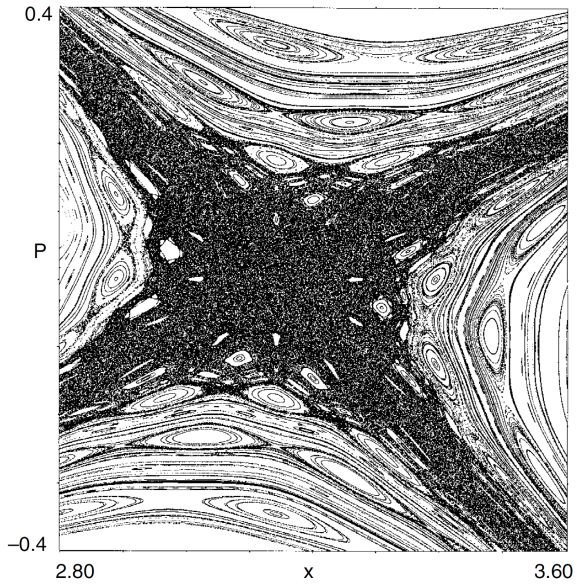

Figure 1.3: The area around the original unstable equilibrium in the so-called Standard map, a map formally equivalent to a Poncaré surface of section defined by periodic snapshots of a non-linearly kicked rotor. The image shows the complicated hierarchical structure at the edges of regular islands. (Taken from Zaslavsky (2008).)

corresponding to two different tangles intersect. A trajectory wandering in the connected layers then switches irregularly between very different modes of motion and is easily distinguished as chaotic.

1.2.3 Strange kinetics

In strong chaos, there is a number of rigorously unresolved phenomena such as stickiness, anomalous diffusion and "strange kinetics" (see Shlesinger et al. (1993) for a short review). To understand the reasons for the exotic behaviour of some chaotic trajectories, we first need to describe the background structures in phase space.

The "regular islands" as the regions of local integrability in a "chaotic sea" are usually enclosed with a complicated fractal-like structure (see fig. 1.3). First, the Fourier series of the perturbation is generally infinite which allows for resonances of any order. As a consequence, we observe resonances being iteratively created on already existing ones spanning virtually to infinite order of the resonance hierarchy. The resulting "fractal dust" on the edge of the regular islands may then be understood as an obstacle for a particle wandering near the island edge.

Second, there is an analytically documented case of an invariant structure in the phase space called a *cantorus* (Percival, 1980). The cantorus is a "broken torus" so that it spans only a Cantor-like set in the phase space leaving a dense set of gaps thus effectively acting as a semi-permeable barrier.

As a result of these structures, the numerically obtained chaotic trajectories exhibit intermittent behaviour between "free-roaming" in the general chaotic sea and being semi-captured in the so-called *sticky layer* of fractal structures near the regular islands. The sticky mode of the trajectory is characterized by an "almost regular" behaviour with longer times needed to discern the trajectory from a

regular one, be it in terms of divergence of nearby trajectories or time-series analysis (see Semerák and Suková (2012) for examples), whereas the "free roam" is characterized by a very immediate chaotic character.

The question of transport seems to be associated with a heft of fascinating phenomena but as is cautioned in the extensive study of MacKay et al. (1984), the numerical investigation of strange kinetics may yield deceiving results. For instance, the chaotic trajectories are known to be so-called "fat fractals" in the sense that their box-counting fractal dimension reaches the full dimension of the phase space freed by non-integrability (e.g. $2N$ for a fully non-integrable system of N degrees of freedom) in the $t \to \infty$ limit. A naive interpretation of this limit is that the trajectory fills the available non-integrable phase space somewhat uniformly in the $t \to \infty$ limit. On the other hand, it is not obvious how this fact should be reconciled with the stickiness and "higher trajectory density" in the sticky layers.

A second concern about the numerical study is the fact that strange kinetics is associated with non-standard statistics. Let τ be the escape time of a trajectory from a given sticky layer. A typical probability distribution obtained by numerical simulations yields the probability of an escape time $p(\tau)$ as a power-law $\sim \tau^{-\alpha}$, $\alpha > 1$ for large τ. This means, in particular, that certain moments of the distribution, $\langle \tau^n \rangle$, $n > \alpha - 1$, are infinite and a verification of the "fat polynomial tail" of the distribution is numerically ill-convergent.

To elaborate this point a little bit further, we will consider an example from MacKay et al. (1984): A power law can be obtained as an infinite sum of "usual" diffusion processes

$$p(\tau) \sim \sum_{n=-\infty}^{\infty} a^{-n} \exp(-b^n \tau) = t^{-\log_b a} Z(\log_b t)\,, \tag{1.27}$$

where $Z()$ is some 1-periodic function. But we will obtain a power-law-like behaviour of $p(\tau)$ even when summing a finite number of terms, and the difference would surface only very far along the tail $\tau \gg 1$. Hence, there is no way to discern numerically a sum of an extremely large number of exponentials from a power law. One could then imagine that in sufficiently smooth systems an analogous sum to that in equation (1.27) is effectively truncated or regularized but we simply do not know because of finite numerical times. As there is no strictly analytical treatment of stickiness (i.e. without any "empiric" assumptions), the question of the true nature of stickiness and the asymptotic picture of the phase space including sticky regions is rigorously unresolved.

2 Axisymmetric perturbations

The remarkable nature of the case of isolated stationary black holes is that the test particle motion is fully integrable even in the case of the axially symmetric field of the Kerr black hole which, as is also demonstrated by the original results of this thesis, is not to be assumed or expected. In general, axisymmetric systems are at least weakly chaotic with no "guaranteed" additional integral of motion apart from the conserved Hamiltonian and an integral obtained from the rotation symmetry. On the other hand, the motion of a particle in an axially symmetric time-independent field has 2 effective degree of freedom with the energy conservation constraint, which allows the motion to cover at most a 3D phase space. This, by virtue of the Poincaré-Bendixson theorem (Bendixson, 1901), means that the motion in an axially symmetric field is a *minimal* example of chaos which is also the easiest to study. The literature on chaotization in two degrees of freedom is vast, so we only review the papers studying situations strictly analogous to that of Chapter 6, axially symmetric perturbations (deformations) of black hole fields, in Section 2.1.

In the following Section 2.2, we briefly discuss and demonstrate, at least in principle, how chaotization is proven via the so-called Melnikov integral or Melnikov function in the case of a Newtonian particle in the field of a spherically symmetric potential under an axially symmetric perturbation; the treatment loosely follows the general description of Guckenheimer and Holmes (1983). The Melnikov integral along the homoclinic orbit[1] is proportional to a linear approximation of the distance between the parts of the homoclinic manifold. Thus, a zero of the Melnikov function means that there is (to linear perturbation order) a transversal intersection and a homoclinic tangle implying chaos (cf. Chapter 1).

The last Section 2.3 then discusses the phenomenology and theory of the resonances which are expected to emerge under the axially symmetric perturbation, discussing reflection-symmetric perturbations in particular. The general theory of resonances under axially symmetric perturbation is hard to find in literature, so the presented arguments are original.

2.1 Chaos near axisymmetrically perturbed black holes

Let us now review previous results in literature on test particle motion in axially symmetric fields, focusing exclusively on physical or physically motivated perturbations of black holes. I.e., we will only mention systems which have effectively two degrees of freedom and no additional activated „internal" degree of freedom such as spin, and whose methods thus directly apply to the presented study. In return, a more detailed review of the results is given. A number of further references on different kinds of relativitistic systems with chaos can be found in Semerák and Suková (2010) and Contopoulos (2002).

[1] Assuming of course that the unperturbed system does have a homoclinic orbit in the phase space.

2.1.1 Multipole perturbations

The first thread of research are the various studies of multipole-perturbed black holes and the induced chaoticity. Here, it is important to realize that there are two kinds of multipoles considered, the "internal multipoles" representing an additional structure around the black hole as influencing a particle far away, and the "external", "shell" or "halo" multipoles representing the effects of a structure far away from the black hole (the studied particle *between* the black hole and the external gravitating source). Obviously, the external multipoles have a more straightforward physical interpretation, whereas the internal multipoles, at least if the particles are interacting closely with the system, can be outright non-physical.

An exact Weyl-space-time superposition (see Chap. 4) of a Schwarzschild black hole with external quadrupoles and octupoles was considered by Vieira and Letelier (1996). The 2^{2n}-poles are reflectionally symmetric whereas the 2^{2n+1} are not, so the quadrupolar term did not break reflection-symmetry around the equatorial plane whereas the octupolar did. As a result, the quadrupole superposition was found not to chaotize the particle motion (at least not strongly and for the given parameter ranges studied) whereas the less-symmetric octupole induced strong chaos. The external dipolar perturbation was added in Vieira and Letelier (1997) resulting in a relatively strong chaotization of the phase space which was contrasted with the Newtonian case (which is well known to be completely integrable). To improve the realisticity of the model, small black-hole spin was later added to the hole-dipole system with the numerical observation of counter-rotating orbits being very slightly more chaotic than corotating (Letelier and Vieira, 1997). This particular set of results was reviewed and revisited with a useful discussion in Vieira and Letelier (1999); investigating also *prolate* rather than only the oblate quadrupole deformations, the authors have come to the conclusion that oblate deformations do not induce strong chaos whereas the prolate do.[2]

Studying a different aspect of the multipolar models, de Moura and Letelier (2000) investigated the chaotic *scattering* of orbits via basin-boundary methods. For time-like geodesics chaotic scattering appeared for all studied multipoles, not, however, for the *oblate* case of the quadrupole (somewhat confirming the results of Vieira and Letelier (1999)). Null geodesics, on the other hand, proved to be harder to chaotize, with chaotic scattering observed only for prolate quadrupole and octupole perturbations. A "pseudo-Newtonian revisit" of the model from Vieira and Letelier (1997) was conducted by Guéron and Letelier (2001) with the conclusion that when the centre of the hole-dipole model is simulated by the Paczyńsky-Wiita potential, the result is even more chaotic than the relativistic case, with an additional chaotization due to special-relativistic dynamics of the particle. Finally,[3] Guéron and Letelier (2002) investigated the system of an arbitrarily spinning black hole superposed with an external dipole, quadrupole and octupole, and an *internal* quadrupole. Once again, the prolate *internal*-quadrupole deformation was shown to generate stronger chaos whereas the oblate not.

2.1.2 Disc superpositions

Even though a gravitating source can be decomposed in the so-called Weyl space-times into a multipolar expansion to obtain the metric by a certain procedure, there *are* non-linear superposition

[2] It should be noted, however, that due to the large parameter spaces and limited computation capacities at the time, the conclusions were drawn only from very particular examples.

[3] Note that we do not give any space to the sometimes cited studies of Chen and Wang (2003) and Wu and Zhang (2006) because the study of Chen and Wang (2003) is not on a satisfactory numerical level and Wu and Zhang (2006) seem to have an outright error in the model because their surfaces of section violate the symmetry of the system.

effects applying in the resulting space-time. Hence, another thread of research is to try to add at least remotely physical specific sources to the black holes rather than their "faraway" effective multipoles.

Saa and Venegeroles (1999); Saa (2000) superposed infinite "homogeneous" disks (at least in terms of a naive interpretation of Weyl coordinates, see Chapter 4) in the equatorial plane with a Schwarzschild black hole to find the chaotization of geodesics. In the first paper, the disc was considered to be only infinitely thin and thus created by a reflectionally symmetric "sewing" of the uniform gravitational fields in the equatorial plane (uniform again in a naive Weyl-coordinate sense). A natural consideration was to compare the influence of the "non-sewn" (without a field jump) uniform reflection-asymmetric field with the influence of its reflection-symmetric counterpart, the disc. Surprising as it may be, the singular disc induced no strong chaos whereas the extremely simple "homogeneous" field did. This is in lines with the previous results, where the reflection-breaking octupole or dipole always caused chaotization, whereas the oblate and reflection-symmetric quadrupole did not. In the second paper, Saa expanded the model by introducing a finite thickness of the discs by a smooth and non-smooth sewing technique. The dependence of the resulting models on the various control parameters was then found to be more nuanced; in some cases the disc thickness lead to chaotization whereas very wide discs lead to an attenuation of chaos; in every case, an additional dipole perturbation lead to rather strong chaos.

It seems that the sole *relativistic* study of geodesics in the space-times of *finite-mass* discs superposed with black holes was conducted in Semerák and Suková (2010, 2012); Suková and Semerák (2013). In the latter, however, the reflectional symmetry was never broken and the portrait of the dynamics roughly corresponds to the disc/oblate quadrupole cases mentioned above.

2.1.3 Deformed Kerr metrics

Another particular line of investigation is to study some of the deformed-Kerr space-times. Dubeibe et al. (2007) studied the Tomimatsu-Sato metric along with another deformation corresponding to a particular case of the more general Manko et al. metric, the deformed metrics motivated mainly as specific models of neutron stars and similar astrophysical objects. The metric has a formal quadrupole-deformation parameter where for the oblate cases geodesic motion was observed to be chaotic and for the prolate case regular (in contrast to the findings cited above). However, Han (2008) reiterated that the chaos of Dubeibe et al. was found in the area of the interior of an eventual neutron star. On the outside of the eventual neutron star, on the other hand, Han observed numerically the *prolate* case to be chaotic and the *oblate* to be regular.

Letelier and Vieira (1998) studied the Taub-NUT space-time with an external dipole perturbation. The external dipole, as per usual, introduces the chaos in the system, whereas the gravitomagnetic Taub-NUT parameter (introducing strong dragging) attenuates the chaos. Another contribution to the "quadrupole discussion" was obtained in Contopoulos et al. (2011) where the authors observed very weak chaos in the quadrupole-oblate case of the Manko-Novikov metric. The Zipoy-Voorhes (also known as the "bumpy black hole") metric was studied by Lukes-Gerakopoulos (2012) and conclusively shown that the metric is very weakly, but indeed, chaotic (for previous controversy see therein).

2.1.4 Magnetic fields near black holes

Last but not least, the orbits near a black hole may not be perturbed only by gravitation but also, as is subject to astrophysical interest, by electromagnetic fields. An early study in this respect was

presented by Karas and Vokrouhlický (1992) for the case of a charged particle in the Ernst space-time (static black hole immersed in a *non-test* magnetic field) with a conclusion of chaoticity. Another short investigation into the motion of charged particles in the magnetic field of a current loop near the Kerr black hole was given by Nakamura and Ishizuka (1993). Nevertheless, the analyses in the two cited papers were conducted with insufficient computational power and more persuasive results on chaos near black holes with magnetic fields were given by Takahashi and Koyama (2009); Kopáček et al. (2010) (see also the studies of orbits near black holes with axi-symmetry broken by magnetic fields in Kopáček and Karas (2014) and near the "Bonor magnetic dipole" in Kovář et al. (2013)).

Takahashi and Koyama (2009) studied the motion of charged test particles near a Kerr black hole perturbed by a test-magnetic dipole to find that the rotation suppresses the chaotization of phase space. Kopáček et al. (2010) then studied the chaotization of orbits near a Kerr black hole in an asymptotically uniform test magnetic field and near a Schwarzschild black hole with a test rotating dipole; with the assistance of the so-called recurrence plots (see Chap. 6), they were able to classify the chaoticity of trajectories in various dynamical states; energy of the particles proved to be an important "chaotization parameter" in both cases. Unlike in the case of Takahashi and Koyama (2009), the black hole spin, when properly adjusting for the shifts in the effective potential, did not show chaos-attenuating (or any other unambiguous) properties.

It is obvious that the research area of motion near perturbed black hole fields has only recently started to mature, mainly thanks to the recent growth in computational power. Nevertheless, new methods of analysis as well as the physical motivation for the precise manner of investigating the presented dynamical systems are needed (this point is further elaborated in the discussion in Concluding remarks).

2.2 Melnikov integral for potential perturbations

2.2.1 Unperturbed system

We are considering Newtonian test point-particle dynamics in the field of a spherically symmetric (mass-independent) gravitational potential. The Hamiltonian in spherical coordinates then reads

$$H = \frac{1}{2}p_r^2 + \frac{p_\theta^2}{2r^2} + \frac{p_\phi}{2r^2\sin^2\theta} + V(r) = \frac{p_r^2}{2} + \frac{L^2}{2r^2} + V(r) \tag{2.1}$$

where $p_r = \dot{r}$, $p_\phi = r^2\dot{\phi}\sin^2\theta$, $p_\theta = r^2\dot{\theta}$ and we can choose the set of three commuting integrals of motion $\mathcal{E} = H, \ell = p_\phi$ and $L^2 = p_\theta^2 + p_\phi^2/\sin^2\theta$. It can be easily shown that $\dot{r}$ is determined by r and the integrals of motion

$$\dot{r} = \pm\sqrt{2(\mathcal{E} - V_{\mathrm{eff}}(r))}\,, \tag{2.2}$$

where $V_{\mathrm{eff}} = V + L^2/(2r^2)$. The trajectory $r(t)$ is then given implicitly by quadrature

$$r(t) \;:\; t - t_0 = \int_{r(t_0)}^{r(t)} \frac{\pm \mathrm{d}r'}{\sqrt{2(\mathcal{E} - V_{\mathrm{eff}}(r'))}}\,. \tag{2.3}$$

Once $r(t)$ is known, it is possible to solve for θ from

$$\dot{\theta} = \frac{p_\theta}{r^2} = \pm\frac{1}{r^2}\sqrt{L^2 - \frac{\ell^2}{\sin^2\theta}}\,, \tag{2.4}$$

to obtain

$$\theta(t) \; : \; \int_{t_0}^{t} \frac{\mathrm{d}t'}{r^2(t')} = \int_{\theta(t_0)}^{\theta(t)} \frac{\pm \mathrm{d}\theta'}{\sqrt{L^2 - \ell/\sin^2\theta'}} \,. \tag{2.5}$$

The last step is to solve $\phi(t)$ as

$$\phi - \phi_0 = \ell \int_{t_0}^{t} \frac{\mathrm{d}t'}{r(t)^2 \sin^2\theta(t)} \,. \tag{2.6}$$

Since the motion is planar a common coordinate choice is to choose $\theta = \pi/2$ to coincide with the plane of motion and solve only for ϕ since $\dot{\theta} = 0$. However, this "coordinate gauge" is not very useful for the study of trajectories under axially symmetric perturbations, so the quadrature is presented here in full generality. The "coordinate gauge" actually most useful for the computation of the Melnikov integral is presented in the next subsection.

2.2.2 Coordinate choice for perturbation

Let us consider the usual Cartesian axes xyz and the perturbation symmetric with respect to a rotation around y. Keeping spherical coordinates one usually takes the ϕ-rotation axis as coinciding with y because then the axisymmetry of the perturbation is expressed simply as independence on ϕ. Nevertheless, we are interested in trajectories which are always somewhat inclined with respect to the plane of axisymmetry and for these the description would become rather complicated under the usual coordinate choice. Hence, we choose a coordinate system adapted for the study of a generally inclined trajectory.

Unlike the usual coordinate choice, the ϕ-rotation axis (now *not* representing the symmetry) is taken *perpendicular* to y, e.g. as z, and $\phi = 0$ is taken to coincide with the yz plane. The $\phi = const.$ planes are then planes under an inclination $\phi + \pi/2$ with respect to the rotational-symmetry axis y. The rotation around the axis of symmetry by an angle Δ is not as simple as with the usual coordinate choice (which would be simply $\phi' = \phi + \Delta$):

$$\theta' = \arccos(\cos\Delta\cos\theta - \sin\Delta\sin\theta\sin\phi) \,, \tag{2.7}$$

$$\phi' = \arccos[(1 - (\cos\Delta\cos\theta - \sin\Delta\sin\theta\sin\phi)^2)^{-1/2}\sin\theta\cos\phi] \,. \tag{2.8}$$

However, we do a "gauge fixing" and never perform this Δ-rotation. We take the families of trajectories with $\dot{\phi} = \ell = 0$ and $\phi = const.$ (the Melnikov integral is computed over the original unperturbed trajectories so the motion is always planar). Every trajectory moving in a plane inclined by κ with respect to y can be obtained by solving a $\phi = \mathrm{const.} = \kappa$ trajectory and performing a Δ-rotation because the dynamics are invariant with respect to the Δ-rotation. Thus, we can study only $\phi = const.$ trajectories without loss of generality.

The perturbations are usually stated either in the form of cylindrical coordinates ρ, z, Δ or spherical coordinates r, Θ, Δ with $\Theta = 0, \pi$ coinciding with y. The transformation rules are

$$\Delta = \arcsin((1 - \sin^2\theta\cos^2\phi)^{-1/2}\sin\phi\sin\theta) \,, \tag{2.9}$$

$$\rho = r\sqrt{1 - \cos^2\phi\sin^2\theta}, \; z = r\sin\theta\cos\phi \,, \tag{2.10}$$

$$\cos\Theta = \sin\theta\cos\phi \,. \tag{2.11}$$

I.e., we take the perturbing potential $P(\rho, z, \Delta)$ or $P(r, \Theta, \Delta)$ and substitute relations (2.9)-(2.11) into it to obtain the perturbation in the presented coordinates.

2.2.3 Reduction

In the $\dot{\phi} = 0$ gauge we have

$$H = \frac{p_r^2}{2} + \frac{p_\theta^2}{2r^2} + V(r)\,. \tag{2.12}$$

We can reduce the system in the following manner

$$\frac{\mathrm{d}r}{\mathrm{d}\theta} = \frac{\dot{r}}{\dot{\theta}} = -\frac{\partial H/\partial p_r}{\partial H/\partial p_\theta} = -\frac{\partial p_\theta}{\partial p_r}|_{\mathcal{E}=const.}\,, \tag{2.13}$$

$$\frac{\mathrm{d}p_r}{\mathrm{d}\theta} = \frac{\dot{p}_r}{\dot{\theta}} = \frac{\partial H/\partial r}{\partial H/\partial p_\theta} = \frac{\partial p_\theta}{\partial r}|_{\mathcal{E}=const.}\,. \tag{2.14}$$

I.e., we can take $-p_\theta$ as a new Hamiltonian with $H = \mathcal{E}$ fixed and a new time coordinate θ. The new Hamiltonian reads

$$I(r, p_r; \mathcal{E}) \equiv -p_\theta(r, p_r; \mathcal{E}) = r\sqrt{2(\mathcal{E} - V) - p_r^2}\,. \tag{2.15}$$

If we now introduce a perturbation to the original Hamiltonian

$$H^\epsilon = H(r, p_r; p_\theta) + \epsilon P(r, \theta; \phi)\,, \tag{2.16}$$

the reduced Hamiltonian will be to linear order

$$I^\epsilon(r, p_r, \theta; \phi, \mathcal{E}) = -p_\theta|_{\epsilon=0} + \epsilon\frac{P}{\dot{\theta}|_{\epsilon=0}} + \mathcal{O}(\epsilon^2) = r\sqrt{2(\mathcal{E} - V(r)) - p_r^2} + \epsilon\frac{rP(r, \theta; \phi)}{\sqrt{2(\mathcal{E} - V) - p_r^2}} + \mathcal{O}(\epsilon^2) \tag{2.17}$$

Variables behind semicolons are to be understood as external parameters of the dynamics. Omitting the dependence on $\mathcal{E}$ and ϕ, the reduced Hamiltonian (2.17) is exactly analogous to a Hamiltonian of a system with one degree of freedom under time-dependent perturbation. It should also be noted that θ is now no longer a periodic coordinate but is extended to $(-\infty, \infty)$ through it's universal covering.

2.2.4 Melnikov function

The Melnikov function for a Hamiltonian

$$\mathcal{H}^\epsilon(x, p, t) = \mathcal{H}(x, p) + \epsilon\mathcal{P}(x, p, t)\,, \tag{2.18}$$

with $\mathcal{P}$ periodic in t is (Guckenheimer and Holmes, 1983)

$$M(t_0) = \int_{-\infty}^{\infty} \mathrm{d}t\{\mathcal{H}, \mathcal{P}\}\,, \tag{2.19}$$

where the integral is taken along the homoclinic orbit and with t starting at t_0. I.e. the parametrization of the homoclinic orbit by t is arbitrary, but the initial phase of $P(x, p, t)$ is relevant for the result.

In our case we assume that we have found a specific homoclinic orbit which we want to test for a transversal intersection and chaotization. The "time" parametrization is through θ and the Melnikov function reads

$$M(\theta_0, \mathcal{E}, \phi) = \int_{-\infty}^{\infty} \mathrm{d}\theta\{\frac{rP(r, \theta - \theta_0; \phi)}{\sqrt{2(\mathcal{E} - V(r) - p_r^2)}}, r\sqrt{2(\mathcal{E} - V(r) - p_r^2)}\}\,, \tag{2.20}$$

where

$$\{f, g\} = \frac{\partial f}{\partial r}\frac{\partial g}{\partial p_r} - \frac{\partial f}{\partial p_r}\frac{\partial g}{\partial r}\,. \tag{2.21}$$

The Melnikov function thus reads

$$M(\theta_0, \mathcal{E}, \phi) = \int_{-\infty}^{\infty} \mathrm{d}\theta \frac{p_r r^3}{p_\theta^2}(2P + r\partial_r P)$$

Even though we know the shape of the homoclinic trajectory in the r, p_r space as $p_\theta(r, p_r; \mathcal{E}, \phi) =$ const., we need to know the parametrization $r(\theta)$ to know the measure along the phase-space trajectory.

The velocity is expressible as

$$p_r = p_r(r) = \sqrt{2(\mathcal{E} - V(r) - p_\theta^2/(2r^2))}\,, \tag{2.22}$$

so we can integrate the integral in r with $\mathrm{d}\theta = \mathrm{d}r/r'$ but care has to be taken around turning points $r' = 0$. In the case of potentials $V(r)$ for which the exact unperturbed trajectories are not known in any convenient form, it is better to ,verify chaos by direct numerical integration.

2.3 Structure and properties of resonances

2.3.1 Poincaré surfaces of section

For the numerical integration of orbits in axisymmetric systems it is best to keep the usual coordinate choice, i.e. ϕ-rotation as the symmetry of the system in either spherical or cylindrical coordinates, and suppress the ϕ coordinate in the description of dynamics. As can be seen from equation (2.6), the ϕ coordinate is periodically increasing if r and θ are periodic but this increase is virtually never a rational multiple of 2π and the shape of the full coordinate trajectory will not reflect the fundamental periodicity of the trajectory. Hence, not only is its immediate value dynamically unimportant but also the periodicity/non-periodicity in ϕ obscures the role of the trajectory in the dynamical system. In conclusion, it is more convenient to display the trajectory-shape only in the r, θ (or cylindrical ρ, z) plane.

However, the best tool for documenting the overall structure of the phase space are Poincaré surfaces of section. In the specific case of our models, the equatorial plane $\theta = \pi/2$ with fixed specific energy $\mathcal{E}$ and specific azimuthal angular momentum $\ell \equiv p_\phi$ is the only good surface of section since all the gravitating mass will be placed on the equatorial plane and every particle will thus sooner or later cross the attracting equatorial plane. The particle dynamics have three degrees of freedom but the ϕ coordinate is suppressed, we fix angular momentum ℓ and one other dimension is supressed by the constraint $\mathcal{E} =$ const. Furthermore, the angular position $\theta = \pi/2$ of the surface of section is fixed so that we have 4 constraints on a point on the surface of section in total. The system has 3 degrees of freedom (6 phase space dimensions), so a given point on the surface of section should have $6 - 4 = 2$ free dimensions left (and two parameters, $\ell, \mathcal{E}$, fixed throughout the entire section). Good candidates for these two dimensions are r and either p_r or p_θ.

By specifying the parameters $\mathcal{E}, \ell$, and $r, p_{r/\theta}$, the point on the surface of section should be unambiguously identified with an initial condition for a trajectory whose evolution to the next intersection

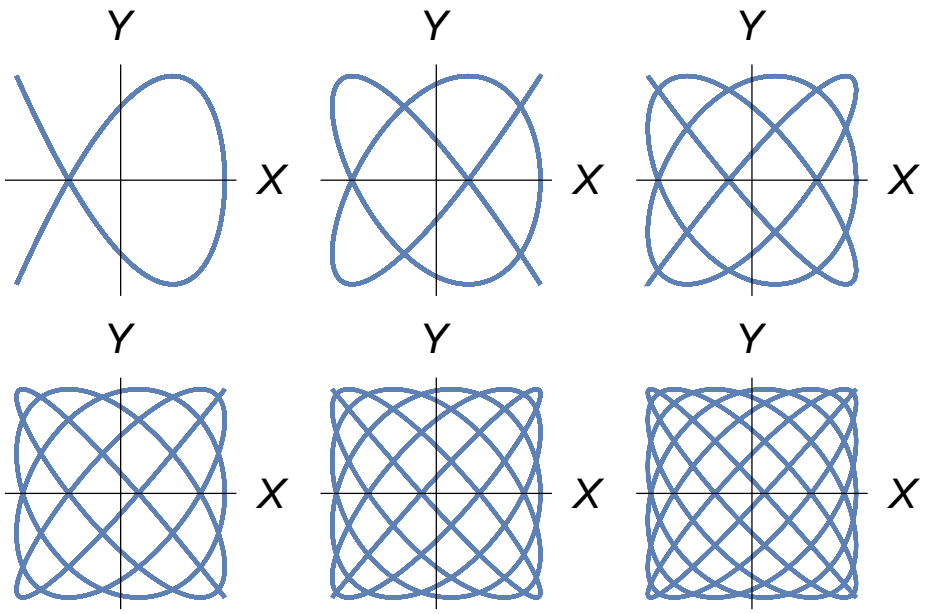

Figure 2.1: A sketch of parametrized curves from equation (2.23) with m:k from left to right 2:3, 4:5, 6:7 in the first row and 8:9, 10:11,12:13 in the second row. The phase ϕ is always set so that the curve is collapsed, i.e. "total-reversible", and the turning point at $X = 1$; the m, k are chosen to correspond to resonances most observed in the surfaces of section in Chapter 6.

defines the iteration of the Poincaré-surface map. Nevertheless, the sign of the remaining momentum $p_{\theta/r}$ is always undetermined because energy is quadratic in momenta. Here we can use another specific property of the studied models: reflectional symmetry about the equatorial plane.

In particular, the reflection-symmetry means that an initial condition different in the sign of p_θ in the equatorial plane will have the same shape up to a reflection about the equatorial plane and will intersect it with the same r, p_r. Hence, if we choose r, p_r as our Poincaré-surface coordinates, the corresponding trajectory could be in the northern hemisphere ($p_\theta > 0$, $\theta < \pi/2$) or in the southern hemisphere ($p_\theta < 0$, $\theta > \pi/2$). Either way, the two trajectories are reflectionally symmetric copies of each other and the next intersection with the equatorial plane will be identical up to the sign of p_θ. Hence, the r, p_r; ℓ, $\mathcal{E}$ Poincaré surface of section in the equatorial plane of a reflection-symmetric system defines an unambiguous Hamiltonian map.

Since the radial momentum for mass-independent dynamics is equal to the radial velocity $p_r = \dot{r} \equiv v^r$, we will mostly use the more "physical" notation v^r instead of p_r in the surfaces of section.

2.3.2 Coordinate shapes and resonances

Integrable trajectories with non-zero angular momentum have two fundamental frequencies, Ω_r determining radial oscillations, and Ω_θ determining vertical oscillations. n-fold resonant islands are grouped around either n or $2n$ intersections of a trajectory through $\theta = \pi/2$. The ambiguity between n or $2n$ is caused by the fact that a point on the surface of section can correspond to an intersection in either direction, from below or above $\theta = \pi/2$. One full period in the θ oscillation makes two such

intersections, one from below and one from above. The periodic trajectory at the center of an n-fold island thus completes either $n/2$ or n full vertical oscillations before it closes (the $n/2$ possibility is obviously allowed only if n is even). This means that an n-fold island corresponds to a periodic trajectory with a ratio of radial and vertical frequency oscillation $m : n/2$ or $m : n$ where m is an integer.

Amongst these, there are trajectories which create a set of islands which are asymmetric [4] with respect to $p_r \to -p_r$. This necessarily means that the resonance grouped around such a trajectory has a symmetric counterpart in the phase space obtained by $p_r \to -p_r$ since this is a symmetry of the Hamiltonian. Another symmetry of the Hamiltonian which can be violated by the periodic trajectory is the equatorial-plane reflection[5] which, however, is not discernible on our "both-direction" surfaces of section.

The ratios of frequencies can be best observed from the shape of trajectories in the $r\sin\theta, r\cos\theta$ space as illustrated by parametrized curves in fig. 2.1. For a periodic trajectory of frequency ratio $m : k$ the difference between making a k- or $2k$-fold island is only in a phase shift, where the more symmetric k-fold case happens only for special discrete values and is thus "of measure zero" (and for some k it is even not possible). However, first order perturbations generate only k-fold resonant islands and the $2k$-fold case is only possible in a non-linear perturbation mode (see e.g. chap. 3 of Zaslavsky (2008)).

Half of the phase choices making the trajectory generate a k-fold island make it *degenerate* in the sense of oscillating back and forth on a single line in coordinate space. Only these phase choices make a totally reversible record of intersections on the equatorial surface of section in the sense that for every $r, \dot{r}$ "from above" intersection there is a $r, -\dot{r}$ intersection "from below". Furthermore, the symmetry of these *total-reversible* trajectories with respect to equatorial-plane reflection turns out to be determined by the parity of the integers m and k. Let us demonstrate this fact on a simple toy model of an $m : k$ periodic trajectory. Consider a motion in two dimensions

$$X(t) = \sin(t + \phi),\ Y(t) = \sin(\frac{k}{m}t), \tag{2.23}$$

where $X(t)$ can be understood as a rescaled and shifted analogy of r and $Y(t)$ as a rescaled analogy of θ. Such a model will have a turning point $t_0 : \dot{X}(t_0) = \dot{Y}(t_0) = 0$ when the phase shift

$$\phi = \frac{\pi}{2}\left(2l + 1 - \frac{m}{k}(2j+1)\right),\ l, j \in \mathbb{Z}, \tag{2.24}$$

where the period of motion is $2m\pi$ so that we may impose without loss of generality $l \in \{0, ..., 2m-1\}$ and $j \in \{0, ..., 2k-1\}$. Exactly under this phase shift the trajectory is degenerate and repeats the same shape in coordinate space twice before finishing the period. We now want to find the second turning point and investigate the symmetry of the resulting trajectory. In our model the stationary points of the Y coordinate alone are only ± 1 in the points

$$t_i = \frac{\pi}{2}\frac{m}{k}(2i+1),\ i \in \mathbb{Z}, \tag{2.25}$$

where the sign of Y is negative for an odd i and positive for an even i. We may again impose $i \in \{0, ..., 2k-1\}$ which gives us all the unique stationary points of Y. By construction of ϕ, for

[4] See the $\mathcal{M} = 0.9$ section in fig. 6.4 where a 3-fold island asymmetric with respect to $p_r \to -p_r$ at the very edge of the chaotic sea is created by 6 intersection of a 2:3 periodic trajectory.

[5] See for example the 2-fold resonant island in the $\mathcal{M} = 0.9$ section in figure6.5 corresponding to a reflection-asymmetric $1 : 1$ periodic "tilted ellipse" in the $r\sin\theta, r\cos\theta$ space.

$i = j$ the trajectory has the turning point with $X(t_j) = 1$ for l even and $X(t_j) = -1$ for l odd. Considering the symmetry of the trajectory with respect to time-reversal around t_j, we arrive to the conclusion that the second turning point must be at t_h, $h = (j + k) \bmod 2k$.

Hence, if k is odd $Y(t_j) = -Y(t_h)$ and if k is even we have $Y(t_j) = Y(t_h)$. On the other hand, for the trajectories for which m is odd we have $X(t_j) = -X(t_h)$ and for m even $X(t_j) = X(t_h)$. This means that the trajectory shape is symmetric with respect to $Y \to -Y$ only if m is even and k is odd.

The only thing we need to map this XY toy model on our r, θ total-reversible trajectories is the assumption that the vertical[6] oscillation alone is symmetric with respect to equatorial-plane reflection.

This assumption is undoubtedly fulfilled for not-yet-resonant regular trajectories in the central island as they are part of a reflectionally-symmetric torus in the phase space whose action-angle evolution must be reflectionally symmetric. Thus, at least for the early life of resonances[7] in the central islands we may state the following: *A total-reversible periodic trajectory of frequency ratio $m : k$ generating a k-fold resonant island is symmetric with respect to reflection about the equatorial plane if and only if m is even and k is odd.* We will call such periodic trajectories *most-symmetric*.

Let us repeat some of the properties of these most-symmetric periodic trajectories, they are symmetric with respect to equatorial plane reflection but also with respect to the reversal of velocities in the sense that for every point of the trajectory in the phase space $r, \dot{r}, \theta, \dot{\theta}$ the trajectory also goes through the point $r, -\dot{r}, \theta, -\dot{\theta}$. We observe the most-symmetric resonances to be more abundant especially in the central island. However, be it in the central island or in the chaotic sea, we also find reflectionally asymmetric resonances[8].

As documented in the footnotes[9], this rough prediction of the character of resonances in the central island fails for strong chaos as resonances stranded deep in the chaotic sea group around periodic trajectories which can violate any of the mentioned symmetries. On the other hand, all of these symmetry-breakings seem to be describable as bifurcations of initially most-symmetric resonances associated with the presence of the very much non-smooth and non-weak disc edge (the ring perturbation).

[6] This "vertical oscillation" need not be given by the coordinate θ, it may be any θ-like coordinate ζ with the only condition that it covers r, θ with another "radial" coordinate R and the equatorial plane corresponds to a certain $\zeta = const$.

[7] But not for the late life, see footnote 5 where the respective trajectory buried deep in the chaotic sea is totally reversible but the vertical oscillation is not reflectionally symmetric.

[8] For an example of a reflectionally asymmetric resonance in the central islands, see the $3 : 4$ near-resonance in the fourth row of fig. 6.20 and the corresponding very thin 8-fold island in the $\mathcal{M} = 0.35$ surface of section in fig. 6.4.

[9] See fotnote 4 and 5.

3 A general pseudo-Newtonian limit

Pseudo-Newtonian potentials are a common tool in astrophysics used to avoid unnecessarily complicated relativistic formulas while at the same time salvaging at least some of the features of a strong-field gravitational situation in a Newtonian framework (see introduction of Tejeda and Rosswog (2013) or Artemova et al. (1996) for a review). Typically, the pseudo-Newtonian description is used for astrophysical simulations in which most of the dynamics happens in regions where a Newtonian description is fully appropriate but where the dynamics marginally pass into a strongly relativistic mode near a compact object such as a Schwarzschild black hole. Splitting the description into a Newtonian and relativistic part while preserving accuracy is often difficult to conceive, so the researcher has to choose between using a fully Newtonian or a fully relativistic code. Thus, if there is a modified "pseudo-Newtonian" dynamics mimicking relativity which seamlessly coincides with Newtonian dynamics in an appropriate limit, then it can be very useful for the purposes of such astrophysical models.

Even though pseudo-Newtonian potentials have been proposed since over 30 years (Paczyński and Wiita, 1980; Nowak and Wagoner, 1991; Artemova et al., 1996; Wegg, 2012), until recently the potentials were not able to accurately reproduce properties of general orbits or to accurately describe the field of a spinning black hole. However, Tejeda and Rosswog (2013, 2014) proposed a class of generalized (velocity-dependent) pseudo-Newtonian potentials accurately describing the motion of quite general test-particles in the Schwarzschild and generally any spherically symmetric space-time. By a similar but slightly more complicated argument, Ghosh et al. (2014) gave a generalized pseudo-Newtonian potential for test-particles in the equatorial plane in the field of a slowly spinning Kerr black hole.

Many questions arise in connection with the recent results: Are the potentials also applicable for null-geodesics, i.e. gravitational lensing? Is there a deeper pattern in the way the potentials are formulated? How do the potentials superpose with additional matter and forces such as electromagnetism? Is it correct to use these relativistic-like potentials along with non-modified Newtonian fluid dynamics? The aim of this chapter is to present the results of investigation of these questions.

3.1 Reparametrization of phase-space trajectories

It is a well known fact often utilized in the theory of classical and celestial mechanics that it is possible to reparametrize a trajectory by a given coordinate using it's conjugate momentum as a new Hamiltonian (this fact was already used in Chapter 2).

I.e. if we have a variable q with a conjugate p_q in the phase space of an autonomous dynamical system with a (time-parameter independent) Hamiltonian H and a coordinate λ with a conjugate momentum p_λ, it holds that

$$\frac{\mathrm{d}q}{\mathrm{d}\lambda} = \frac{\dot{q}}{\dot{\lambda}} = \frac{\frac{\partial H}{\partial p_q}}{\frac{\partial H}{\partial p_\lambda}}\Big|_{H=const.} = \frac{\partial(-p_\lambda)}{\partial p_q}\Big|_{H=const.}, \tag{3.1}$$

where the first equality holds only under the assumption of $\dot{\lambda} \neq 0$ and the last equality follows from the implicit function theorem.

Even though the resulting trajectory might be moving at a different pace with respect to the parameter λ, it will draw the same shape in the *full phase space* of coordinates and canonically conjugate momenta (q, p_q). Thus, for a given initial condition in the phase space variables, the shape of the original trajectory is reproduced exactly.

Nevertheless, we will use this reparametrization technique to obtain pseudo-Newtonian Hamiltonians and Lagrangians in a new pseudo-time with an interpretation of $\mathrm{d}q/\mathrm{d}\lambda$ as physical velocities. Hence, the velocities will be rescaled by $\mathrm{d}\lambda/\mathrm{d}\tau$ in comparison with the original proper velocities $\mathrm{d}q/\mathrm{d}\tau$. The motion in terms of coordinates q and canonical momenta p_q will be the same, but the conversion from p_q to the "new velocities" $\mathrm{d}q/\mathrm{d}\lambda$ will be often very different.

Once giving the initial condition in terms of coordinates and velocities, the trajectories will be different accordingly because before the reparametrization the initial velocity is plugged into initial $\mathrm{d}q/\mathrm{d}\tau$ whereas in the second case the initial velocity is inserted as the initial $\mathrm{d}q/\mathrm{d}\lambda$. I.e., each trajectory generated by these models will correspond to *some* exact trajectory in the original space-time, but with a rescaled velocity.

On the other hand, integrals of motion are always functions of the phase space which means that if we have a complete set of first integrals of motion, then by giving their values we obtain the exact relativistic orbit even under reparametrization. For instance, in many space-times there is a family of circular orbits uniquely characterized by their position (coordinate shape) and a set of angular momenta. As follows from the previous discussion, such a family of circular orbits will be exactly preserved under reparametrization in the sense of the same position and canonical angular momenta.

3.2 Geodesics in general space-times

The general-relativistic Lagrangian of a free test particle reads (we use the $G = c = 1$ units and $-+++$ sign convention)

$$L = \frac{1}{2} g_{\mu\nu} \dot{x}^\mu \dot{x}^\nu, \; \dot{x}^\mu \equiv u^\mu \equiv \frac{\mathrm{d}x^\mu}{\mathrm{d}s}, \tag{3.2}$$

where s is the proper time τ for massive particles and affine parameter λ for massless particles. Under a Legendre transform we obtain the Hamiltonian

$$H = \frac{1}{2} g^{\mu\nu} u_\mu u_\nu, \tag{3.3}$$

where u_μ is canonically conjugate with respect to x^μ. It is convenient that due to four-velocity normalization for all particles of a given kind we have $H = L = -\kappa/2$, where $\kappa = 1$ corresponds to massive particles and $\kappa = 0$ to massless particles.

Say we now have a convenient time coordinate t corresponding to the 0-component of the metric and spatial coordinates labelled by $i, j = 1, 2, 3$. In the following, it will be important that t is a "good" time coordinate in the sense of e.g. being the flat time in approximately flat regions of the space-time. Then we can invert the Hamiltonian to obtain

$$\tilde{H} = -u_0 \equiv \mathcal{E} = \omega^i u_i - \sqrt{(\omega^i u_i)^2 - (g^{ij} u_i u_j + \kappa)/g^{00}}, \tag{3.4}$$

where we have chosen the root which corresponds to particles travelling forward in time under the assumption $g^{00} < 0$, and where $\omega^i \equiv g^{0i}/g^{00}$ is the gravitomagnetic part of the metric. The expression (3.4) could be used as a "Newtonian" Hamiltonian as it will exactly reproduce the shapes of

trajectories in the 3-dimensional coordinate space parametrized by the coordinate time t as long as

$$\frac{\partial H}{\partial u_0} = g^{0\mu}u_\mu \equiv u^0 \neq 0. \tag{3.5}$$

Nonetheless, there is nothing Newtonian about the motion, which is fully relativistic.

To obtain an expression for the respective generalized velocity-dependent potential one has to pass back to Lagrangian formalism via a Legendre transform. Nevertheless, it should be kept in mind that

$$u_i \neq \frac{\mathrm{d}x^i}{\mathrm{d}t}, \tag{3.6}$$

and that Legendre transforming back to Lagrangian formalism requires expressing u_j from

$$\frac{\mathrm{d}x^i}{\mathrm{d}t} = u^i u^0 = g^{i\nu}u_\nu g^{0\mu}u_\mu \tag{3.7}$$

with the substitution of equation (3.4) for u_0. However, the complicated form of equation (3.4) seems not to allow such an inversion in general so one can only resort to approximations. The approximation used henceforth is that $\mathcal{E} = 1 + \delta$ where δ is a small quantity.

It should be noted that in nearly flat space-time and for massive particles this limit yields exactly the dynamics of a non-relativistic particle in the Newtonian gravitational fields. However, such an assertion is not true in strongly curved space-times which leads to the conclusion that the presented limit should be in fact called the "pseudo-Newtonian" limit. Taking the four-velocity normalization we obtain up to $\mathcal{O}(\delta^2)$

$$2g^{00}\delta - 2g^{0i}\delta u_i + g^{00} + g^{0i}u_i + g^{ij}u_i u_j = -\kappa \tag{3.8}$$

which can be rearranged as

$$H_{\mathrm{PN}} = 1 + \delta = -\frac{1}{2(1-\omega^i u_i)}\frac{g^{ij}}{g^{00}}u_i u_j - \frac{1}{2(1-\omega^i u_i)}\left(\frac{\kappa}{g^{00}} - 1\right). \tag{3.9}$$

Hence, we can use this expression as a new Hamiltonian which should up to $\mathcal{O}((\mathcal{E}-1)^2)$ reproduce the particle motion. However, one would like to know a better estimate of the error the trajectory is introduced to when taking expression (3.9) as a new Hamiltonian. For that we recover H_{PN} *exactly* in terms of δ

$$H_{\mathrm{PN}} = 1 + \delta + \frac{\delta^2}{2(1-\omega^i u_i)} = \mathcal{E} + \frac{(\mathcal{E}-1)^2}{2(1-\omega^i u_i)}. \tag{3.10}$$

If we take a coordinate q and it's canonically conjugate momentum p_q, Hamilton's equations yield

$$\begin{aligned} -\frac{\partial H_{\mathrm{PN}}}{\partial q} &= -\frac{\mathcal{E}+\omega^i u_i}{1+\omega^i u_i}\frac{\partial \mathcal{E}}{\partial q} + \frac{(\mathcal{E}-1)^2}{2(1+\omega^i u_i)}\frac{\partial}{\partial q}(\omega^i u_i) \\ &= \frac{\mathcal{E}+\omega^i u_i}{1+\omega^i u_i}\frac{\mathrm{d}p_q}{\mathrm{d}t} + \frac{(\mathcal{E}-1)^2}{2(1+\omega^i u_i)}\frac{\partial}{\partial q}(\omega^i u_i). \end{aligned} \tag{3.11}$$

Under the interchange $q \leftrightarrow -p_q$ we get a similar result for the other equation of motion. Thus, the pseudo-Newtonian Hamiltonian H_{PN} yields an approximate shape of the geodesic with an $\mathcal{O}(\delta)$-rescaled parametrization with respect to coordinate time and with an $\mathcal{O}(\delta^2)$ deformation term[1].

[1] It is possible to give more accurate iterations of the pseudo-Newtonian limit up to a general order $\mathcal{O}(\delta^n)$ yielding an $\mathcal{O}(\delta^{n-1})$ rescaling of time and $\mathcal{O}(\delta^n)$ deformation term albeit at the cost of more complicated Hamiltonians. Even so, such iterations yield very complicated expressions very much against the spirit of simplicity of pseudo-Newtonian frameworks.

The last remark is that in the case of massless particles the evolution of the light-ray depends only on the direction of the four-velocity and we are thus free to normalize the initial velocity u^μ so that $-u_0 = \mathcal{E} = 1$. In the case of a space-time stationary with respect to t, $\mathcal{E}$ is an integral of motion and the parametrization can be made exact along the whole curve by appropriate normalization. I.e. if we are given an initial direction of the light-ray in terms of $\tilde{u}_i$, we obtain the correct parametrization by using the initial momenta $u_i = \tilde{u}_i/\alpha$ with

$$\alpha = \omega^i \tilde{u}_i - \sqrt{(\omega^i \tilde{u}_i)^2 - g^{ij}\tilde{u}_i\tilde{u}_j/g^{00}}, \tag{3.12}$$

3.3 Time-diagonal space-times

We now investigate the class of metrics for which $g^{0i} = 0$. Such metrics correspond to static space-times, but also to e.g. cosmological or gravitational-wave metrics. For these equation (3.9) gives (up to a constant)

$$H_{\mathrm{PN}} = -\frac{1}{2} g_{00} g^{ij} u_i u_j - \frac{\kappa}{2} m(g_{00} + 1). \tag{3.13}$$

The resulting equations of motion can be related to the exact geodesics similarly as in equation (3.1)

$$\frac{\partial H_{PN}}{\partial p_q} = \mathcal{E}\frac{\mathrm{d}q}{\mathrm{d}t} = -g_{00}\frac{\mathrm{d}q}{\mathrm{d}s},\ s = \tau, \lambda, \tag{3.14}$$

and analogously for the equations of motion for momenta. Equation (3.14) implies that the shape of the orbit generated by this Hamiltonian will be an exact geodesic up to a rescaling of velocities and time. One can understand the rescaling either as a local deformation of proper time (affine parametrization) by $-1/g^{00}$ or a global rescaling of coordinate time by $\mathcal{E}$ (in the case $\mathcal{E}$ is a constant of motion)[2].

Additionally, under the assumption $g_{00} \to -1$ at infinity the Hamiltonian will also generate exact scattering with respect to initial conditions given in terms of proper-time velocities or in terms of canonically conjugate momenta. (Recall that the phase-space trajectory is reproduced exactly by the reparametrizing Hamiltonian.)

The corresponding Lagrangian reads

$$L_{\mathrm{PN}} = -\frac{1}{2} m \frac{g_{ij}}{g_{00}} \dot{x}^i \dot{x}^j + \frac{\kappa}{2} m(g_{00} + 1), \tag{3.15}$$

where in this case $\dot{x}^i \equiv \mathrm{d}x^i/\mathrm{d}\tilde{t}$ are the velocities with respect to the rescaled time $\mathrm{d}\tilde{t} = \mathrm{d}t/\mathcal{E}$. If we would like to identify a velocity-dependent pseudo-Newtonian potential, we must first identify a natural "flat" metric in the coordinate space d_{ij}. The Lagrangian is then simply rewritten into the form

$$L_{\mathrm{PN}} = \frac{1}{2} m d_{ij} \dot{x}^i \dot{x}^j 1 + m\Phi_{\mathrm{PN}}(x^i, \dot{x}^i), \tag{3.16}$$

$$\Phi_{\mathrm{PN}} = \frac{\kappa}{2}(g_{00} + 1) - \frac{1}{2}\left(\frac{g_{ij}}{g_{00}} + d_{ij}\right)\dot{x}^i \dot{x}^j. \tag{3.17}$$

[2] As a pedagogical note, one might use this discussion to show that Newtonian physics can be understood as forcing a global pseudo-time to parametrize every inertial system equivalently.

For example, in the case of an asymptotically flat space-time the pseudo-gravitational potential $\Phi_{\rm PN}$ goes asymptotically to zero if $g_{00} \to -1$ and $-g_{ij}/g_{00} \to d_{ij}$.

Another nice feature is the fact that for a gravitational source of mass M the first term of the pseudo-gravitational potential in SI units is a GM/r effect whereas the second one is a GMc^{-2}/r effect. Thus once neglecting $1/c^2$ terms, we gain exactly the well known non-relativistic weak-field relation $g_{00} = -1 - 2\Phi$.

Additionally, the specific form of the potential (3.17) allows for an intriguing intuitive interpretation. The first term in the pseudo-Newtonian potential is a purely potential term corresponding to the Newtonian gravitational potential, whereas the second term is a "geometrical correction" of the kinetic energy.[3] For instance, near a Schwarzschild black hole of mass M the centrifugal term $\ell^2/2r^2$ of a particle bearing an angular momentum ℓ at Schwarzschild radius r gets "geometrically corrected" as

$$\frac{\ell^2}{2r^2} \to \frac{\ell^2}{2r^2}\left(1 - \frac{2M}{r}\right). \tag{3.18}$$

One can then intuitively explain the in-fall into the black hole merely as a consequence of the geometry "turning off" the centrifugal barrier. The second point to be made on the intuitive interpretation of the structure of the potential (3.17) is that a photon, as a massless particle, is not affected by the purely potential term and only by the second "geometro-potential" term.[4]

It is only from the discussion in this section where the plausibility of the usage of expression (3.9) as a new Hamiltonian and it's Newtonian interpretation is imminent.

3.3.1 Spherically symmetric space-times

The first example which comes to mind is the Schwarzschild space-time for which the formula (3.15) gives

$$L_{\rm TR} = \frac{1}{2}\left(\frac{\dot{r}^2}{(1-2M/r)^2} + \frac{r^2(\sin^2\vartheta\,\dot{\phi}^2 + \dot{\vartheta}^2)}{1-2M/r}\right) + \kappa\frac{M}{r}, \tag{3.19}$$

which for $\kappa = 1$ coincides with the Lagrangian derived from the equations of motion in the Schwarzschild space-time by Tejeda and Rosswog (2013). (The $\kappa = 0$ light-ray case proposed only here.) Similarly, one obtains the same formula as in Tejeda and Rosswog (2014) once applying formula (3.15), $\kappa = 1$ to spherically symmetric space-times.

The authors have found that these pseudo-Newtonian descriptions reproduce exactly the relation between the radii of circular orbits and the particle energy and angular momentum. This is to be anticipated in light of the discussion in section 3.2. Furthermore, neither the Keplerian or epicyclic frequencies of circular orbits given by the pseudo-Newtonian Lagrangian have been found to differ by more than 10% from the values in the relativistic space-times considered by the authors. Once again, this concordance is easily explained by the fact that the reparametrization introduces a relative time-lag

$$\Delta t = 1 - \mathcal{E}, \tag{3.20}$$

with the frequencies of close oscillations scaling accordingly. For instance in the case of Schwarzschild, the tightest-bound circular orbit has $\mathcal{E} = \sqrt{8/9}$ yielding the highest relative time-lag $\Delta t \approx 0.06$. Similarly in any given space-time, the highest time lag will be given by the specific binding energy of the tightest bound orbit.

[3] It would be more accurate to talk about a *geometro-potential* correction due to the $1/g^{00}$ factor.

[4] On the other hand, invariance of light-rays with respect to conformal rescalings of the metric are more obvious from the form (3.15).

3.4 Applications and external forces

3.4.1 Superposition with axisymmetric sources

A class of astrophysical situations of interest can be described by a superposition of a central black hole and an additional axisymmetric structure such as a slowly rotating gravitating disk or torus. Exact relativistic superpositions of a static black hole with a disc were studied e.g. by Semerák et al. (1999b,a) and in this subsection, the pseudo-Newtonian counterpart is briefly investigated.

Static, axially symmetric vacuum space-times are described by the Weyl metric (Weyl and Bach, 1922)

$$\mathrm{d}s^2 = -e^{2\nu}\mathrm{d}t^2 + e^{2\lambda-2\nu}(\mathrm{d}\rho^2 + \mathrm{d}z^2) + e^{-2\nu}\rho^2\mathrm{d}\phi^2, \tag{3.21}$$

where the cosmological constant is necessarily set to zero, the metric function $\nu(\rho, z)$ satisfies the Poisson equation in cylindrical coordinates with respect to a matter distribution $w(\rho, z)$ and $\lambda(\rho, z)$ is obtained through a line integral of a function of derivatives of ν (see Chap. 4 for more details). For these metrics formula (3.15) yields

$$L_{\mathrm{W}} = \frac{1}{2}\left[e^{2\lambda-4\nu}(\dot\rho^2 + \dot z^2) + e^{-4\nu}\rho^2\dot\phi^2\right] + \frac{\kappa}{2}(1 - e^{2\nu}), \tag{3.22}$$

We would now like to see how do additional axially symmetric matter sources superpose with the Tejeda-Rosswog potential, i.e. the pseudo-Newtonian potential of a Schwarzschild black hole. In that case it is useful to interpret the additional sources as perturbations and switch to the pseudo-Schwarzschild coordinates r, ϑ, ϕ

$$\rho = \sqrt{r(r-2M)}\sin\vartheta, z = (r - M)\cos\vartheta \tag{3.23}$$

where M is the black hole mass. In such a case one obtains the pseudo-Newtonian Lagrangian

$$L_{\mathrm{sup}} = \frac{1}{2}\Big[\frac{e^{2\lambda_{\mathrm{E}}-4\nu_{\mathrm{E}}}}{(1-2M/r)^2}\dot r^2 + \frac{e^{-4\nu_{\mathrm{E}}}r^2}{1-2M/r}(e^{2\lambda_{\mathrm{E}}}\dot\vartheta^2 + \sin^2\vartheta\dot\phi^2)\Big] - \frac{1}{2}\Big[1 - e^{2\nu_{\mathrm{E}}}(1 - \frac{2M}{r})\Big], \tag{3.24}$$

where ν_{E} is the Newtonian potential of the external axially symmetric source and λ_{E} will once again be a function acquired by a line integral (but it will include *both* the black-hole and external potentials).

If the external source of mass $\mathcal{M}$ is light in comparison with the black hole, and nonsingular, then one can switch to SI units, neglect the $G\mathcal{M}/c^2$ effects, leave only the $G\mathcal{M}$ effects to linear order, and switch back to geometrized units to obtain

$$\begin{aligned} L_{\mathrm{suptrunc}} = \frac{1}{2}m\left[\frac{\dot r^2}{(1-2M/r)^2} + \frac{r^2(\dot\vartheta^2 + \sin^2\vartheta\dot\phi^2)}{1-2M/r}\right] \\ -m\left[\frac{M}{r} - \nu_{\mathrm{E}} + \frac{2M\nu_{\mathrm{E}}}{r}\right], \end{aligned} \tag{3.25}$$

where the $2M\nu_{\mathrm{E}}/r$ term is non-negligible only near the black hole for an external source close to the horizon. Nonetheless, up to the $2M\nu_{\mathrm{E}}/r$ term, expression (3.25) shows that a simple superposition of an external axially symmetric Newtonian potential with the Tejeda-Rosswog Lagrangian from equation (3.19) will actually work reasonably well for sufficiently light sources far away from the horizon[5].

[5]It should be noted that $\nu(\rho, z)$ is a Newtonian gravitational potential in Weyl coordinates ρ, z interpreted as the usual cylindrical coordinates, but that is not true for pseudo-Schwarzschild coordinates (see transformation in eq. (3.23)) interpreted as spherical coordinates. Once again this discrepancy vanishes for $r \gg 2M$.

3.4.2 Electromagnetic forces

The Hamiltonian of a charged particle with specific charge $c = e/m$ in an electromagnetic field A^μ reads

$$H_{\mathrm{EM}} = \frac{1}{2} g^{\mu\nu}(\pi_\mu - cA_\mu)(\pi_\nu - cA_\nu), \tag{3.26}$$

where $\pi_\mu = u_\mu + cA_\mu$ is canonically conjugate to x^μ. Analogously to Subsection 3.3 we invert the expression for the constant value of the Hamiltonian $H_{\mathrm{EM}} = -\kappa/2$ to get a Hamiltonian of coordinate-time parametrized electro-geodesics

$$\begin{gathered}\tilde{H} = -\pi_0 \equiv \mathcal{E}_{\mathrm{EM}} = \mathcal{E} + cA_0 = \\ \sqrt{-g_{00}(\kappa + g^{ij}(\pi_i - cA_i)(\pi_j - cA_j))} + cA_0.\end{gathered} \tag{3.27}$$

However, there seems not to be a satisfactory pseudo-Newtonian limit when $A_0 \neq 0$ i.e. when $\pi_0 \neq u_0$. In most astrophysical situations this will not be an issue because electrostatic fields play a negligible role in the dynamics. Alternatively, one can use the gauge freedom $A'_\mu = A_\mu + \partial_\mu \alpha$ to eliminate A_0. Once $A_0 = 0$, the pseudo-Newtonian limit gives trivially

$$H_{\mathrm{PN,EM}} = -\frac{1}{2(1 - \omega^i u_i)} \frac{g^{ij}}{g^{00}} u_i u_j - \frac{1}{2(1 - \omega^i u_i)} \left(\frac{\kappa}{g^{00}} - 1 \right), \tag{3.28}$$

with the substitution $u_i = \pi_i - cA_i$. Hence, the addition of electromagnetism up to the gauge fix $A_0 = 0$ is exactly in the lines of the usual minimal coupling.

3.4.3 Note on fluid dynamics

Consider the Boltzmann equation (BE) for a distribution $f(x^i, v^i)$ in the field of an arbitrary velocity-dependent acceleration field $\ddot{x}^i = a^i(x^i, v^i)$ and a collision term $\delta f/\delta t$

$$\frac{\partial f}{\partial t} + v^i \frac{\partial f}{\partial x^i} + a^i \frac{\partial f}{\partial v^i} = \frac{\delta f}{\delta t}. \tag{3.29}$$

When integrating the zeroth moment $\int ... \mathrm{d}^3 v$ of the BE one usually uses the fact that a^i can be factored out to yield $\int \nabla_v f \, \mathrm{d}^3 v = 0$ due to sufficiently fast fall-off of $f(x^i, v^i)$ for $v \to \infty$. However, this cannot be done in the case of velocity-dependent a and we obtain

$$\frac{\partial n}{\partial t} + \frac{\partial V^i}{\partial x^i} + \langle \frac{\partial a^i}{\partial v^i} \rangle_v = \frac{\delta n}{\delta t}, \tag{3.30}$$

where n is the number density, V^i the mean velocity and the assumption that af falls of sufficiently fast at infinity was used. Similarly the first moment $\int v^j ... \mathrm{d}^3 v$ yields

$$\frac{\partial V^j}{\partial t} + \frac{\partial T^{ij}}{\partial x^i} + A^j + \langle v^j \frac{\partial a^i}{\partial v^i} \rangle_v = \frac{\delta v^j}{\delta t}, \tag{3.31}$$

where T^{ij} is up to a factor of m the usual stress tensor and A^j the mean acceleration. The new terms $\langle v^j \partial a^i / \partial v^i \rangle_v$ and $\langle \partial a^i / \partial v^i \rangle_v$ seem to violate some of the basic physical properties of the fluid equations but since in our case a velocity-dependent a is based on a Hamiltonian single-particle formulation, it is obvious that these terms only express the fundamental inseparability of the phase space.

The need to include these terms into hydrodynamical codes is a drawback of the velocity-dependent pseudo-Newtonian potentials. However, exploring the issues with the implementation of velocity-dependent potentials in accretion studies is beyond the scope of the current thesis.

3.5 Image of a glowing torus under self-gravitation

One of the simplest examples of a Weyl space-time is the one of an infinitely thin ring with uniform density derived by Weyl and Bach (1922) for which the metric functions read

$$\begin{aligned} \nu_{\mathrm{BW}} &= -\frac{2MK(\mu)}{\pi l_2}, \\ \lambda_{\mathrm{BW}} &= \frac{M^2\mu^2}{4\pi^2 b^2 \rho}[(\rho+b)(-K^2+4\mu' K\dot{K}+4\mu\mu'\dot{K}^2) \\ &\quad -4\rho\mu^2\mu'(\mu'+2)\dot{K}^2], \\ K(\mu) &= \int_0^{\pi/2} \frac{1}{1-\mu\sin^2\psi}\mathrm{d}\psi, \\ \dot{K} \equiv \frac{\mathrm{d}K}{\mathrm{d}\mu},\ \mu' &= \left(\frac{l_1}{l_2}\right)^2,\ \mu = 1-\mu' = \frac{4\rho b}{(l_2)^2}, \\ l_{1,2} &\equiv \sqrt{(\rho\mp b)^2+z^2}, \end{aligned} \tag{3.32}$$

where b is a formal coordinate radius of the ring which we will use as the reference geometrical length. The Hamiltonian of a light-ray then reads

$$H_{\mathrm{LBW}} = \frac{1}{2}e^{4\nu_{\mathrm{BW}}-2\lambda_{\mathrm{BW}}}(k_\rho^2+k_z^2)+e^{4\nu_{\mathrm{BW}}}\frac{\ell^2}{2\rho^2}, \tag{3.33}$$

where $\ell = e^{-4\nu_{\mathrm{BW}}}\rho^2\dot{\phi}$ is an integral of motion. We now propose a following toy model: we take the Bach-Weyl ring as an exterior solution of a glowing torus and want to compute the image which is seen by an observer O at rest at some ρ_O, z_O (ϕ_O arbitrary).

We model the glowing torus as a Lambertian surface (subject to the cosine formula) of constant luminosity at $(\rho-b)^2+z^2=R^2$. The image of the torus is then computed by picking a point in the celestial sphere of observer O and integrating the light-ray in the corresponding direction normalized according to expression (3.12). If the light-ray hits the torus, the corresponding luminosity of the point on the celestial sphere is computed via the Lambert cosine formula. It should be noted, however, that we still use the relativistic metric for computing the angles of incidence on the torus and the angles on the celestial sphere, and the model is thus fully relativistic.

To integrate the equations of motion, we use a standard explicit Runge-Kutta scheme of 6th order (Iserles, 2009), integrating only the ρ, z variables, and varying the step by $1/(1+|\nu_{\mathrm{BW}}|)$. The angle of incidence is computed from $\dot{\rho}$, $\dot{z}$, $\dot{\phi} = \exp(4\nu_{\mathrm{BW}})\ell/\rho^2$. The code is very lightweight, the largest number of lines due to the computation of $\nu_{\mathrm{BW}}, \lambda_{\mathrm{BW}}$ and it's derivatives.

We then take an observer at $\rho_O = 10b, z_O = 10b$, fix[6] $R = 0.1b$ and investigate the effects of growing mass of the ring from the "Newtonian limit" $\mathcal{M}=0$ to $\mathcal{M}=b$.

In fig. 3.1 the actual image of the torus is plotted, fig. 3.2 shows the coordinate time it took for the light to arive to the observer and fig. 3.3 shows the initial z_i/Ron the torus from which the ray arrived to the observer.

The first effect observed in the images is that as the mass of the torus grows, the angular diameter of its image gets larger. The second effect is that for growing torus-mass, additional images emerge,

[6] As per usual, there is no unambiguous analogy between the relativistic and Newtonian system. For instance, one could also fix either the proper surface of the torus, the inner or outer proper radius or circumference or other invariant geometrical quantity thus effectively yielding $R = R(\mathcal{M})$.

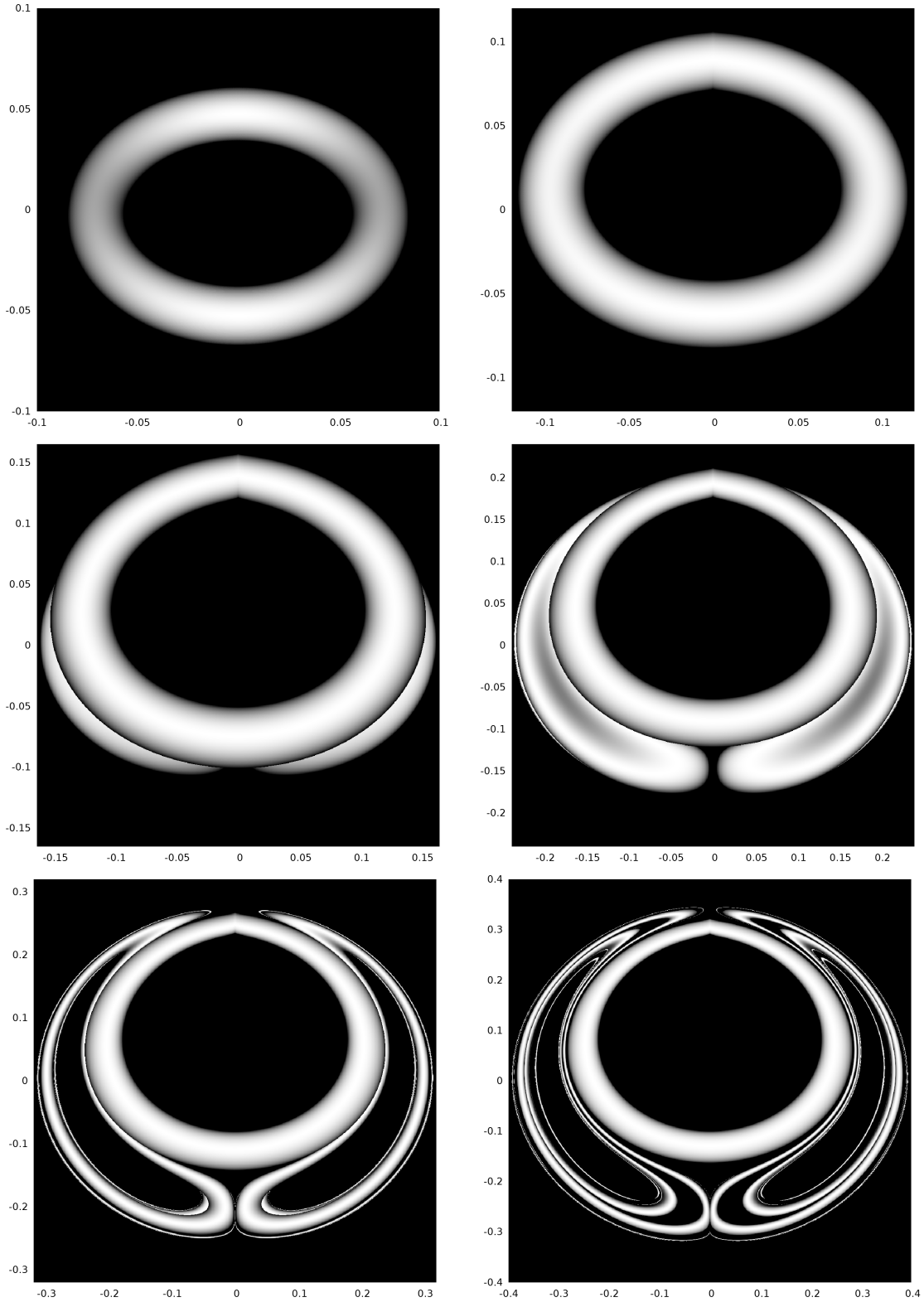

Figure 3.1: Physical images of tori under self-gravitation for the ring masses $\mathcal{M}/b = 0.2, 0.4, 0.6, 0.8, 1$, from left to right and from top to bottom respectively. The axes indicate the angular diameter of the image which grows with ring mass $\mathcal{M}$.

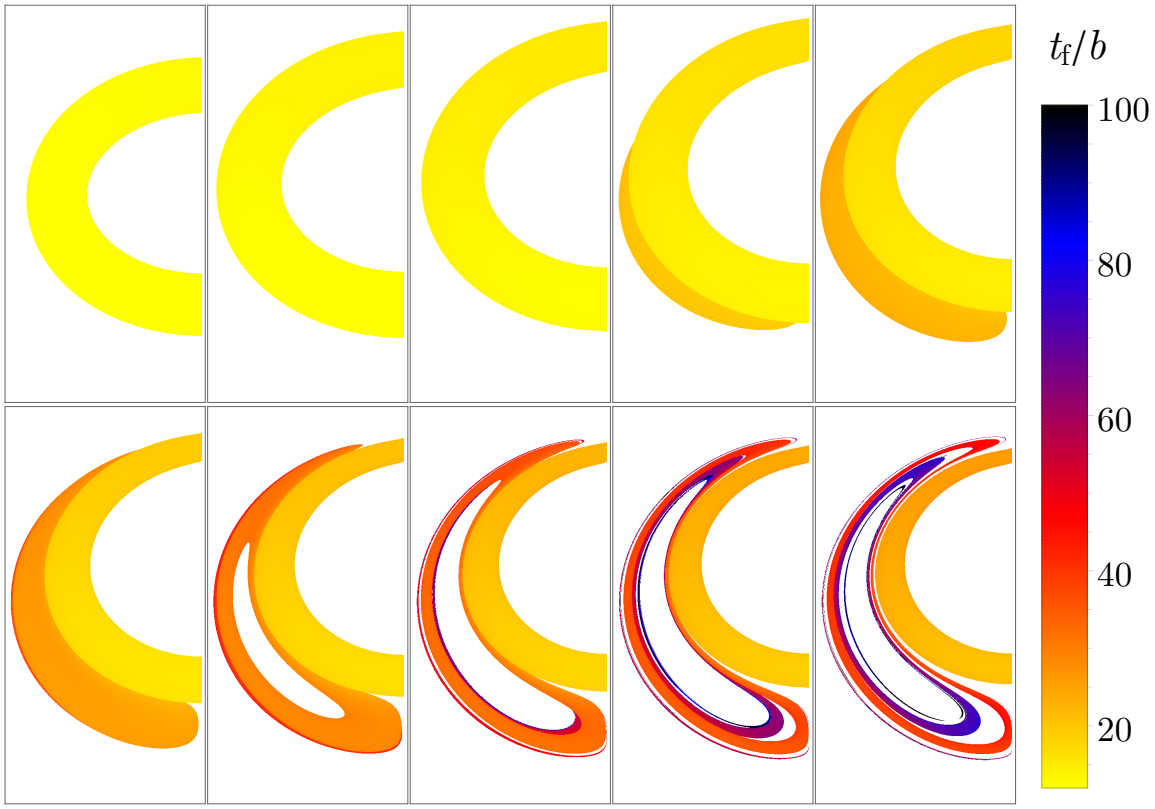

Figure 3.2: Coordinate time t_f taken for the light-ray to arrive to the observer for different parts of the torus image for $\mathcal{M}/b = 0.1, 0.2, ..., 1.0$, from left to right and from top to bottom respectively. The coordinate time of lfight gets generally longer with growing $\mathcal{M}$ and every "new" image seems to take more and more time to arrive to the observer.

corresponding to additional half-loops made by the light-ray around the torus. Every new image comes from a different part of the torus than the previous one (fig. 3.3) and takes a longer coordinate time to arrive to the observer (fig. 3.2).

As a result, an observer with a slightly blurred view of the torus will have the information about the surface of the torus smeared both on temporal and spatial scales; for $\mathcal{M} \approx b$ the different parts of the torus would be probably unrecoverable from the data and the time-dependent phenomena such as pulsations reverberated with $t \sim 10b$ delays. However, the object is far from astrophysically realistic so these conclusions are only demonstrative.

A particular effect observable in fig. 3.1 is that the image of the torus has a cusp at the top. This effect seems to be connected with the fact that the null-geodesic between the observer and the torus passing exactly through the axis becomes unstable for $\mathcal{M} \neq 0$. As a result, close orbits diverge exponentially which creates the cusp in this image. Of course, an alternative explanation is an error in the code, namely the implementation of the functions ν and λ (note that the effect is not present for $\mathcal{M} = 0$); the numerical precision has been tested by varying the integration step and altering step controllers but the cusp is unhindered by such variations.

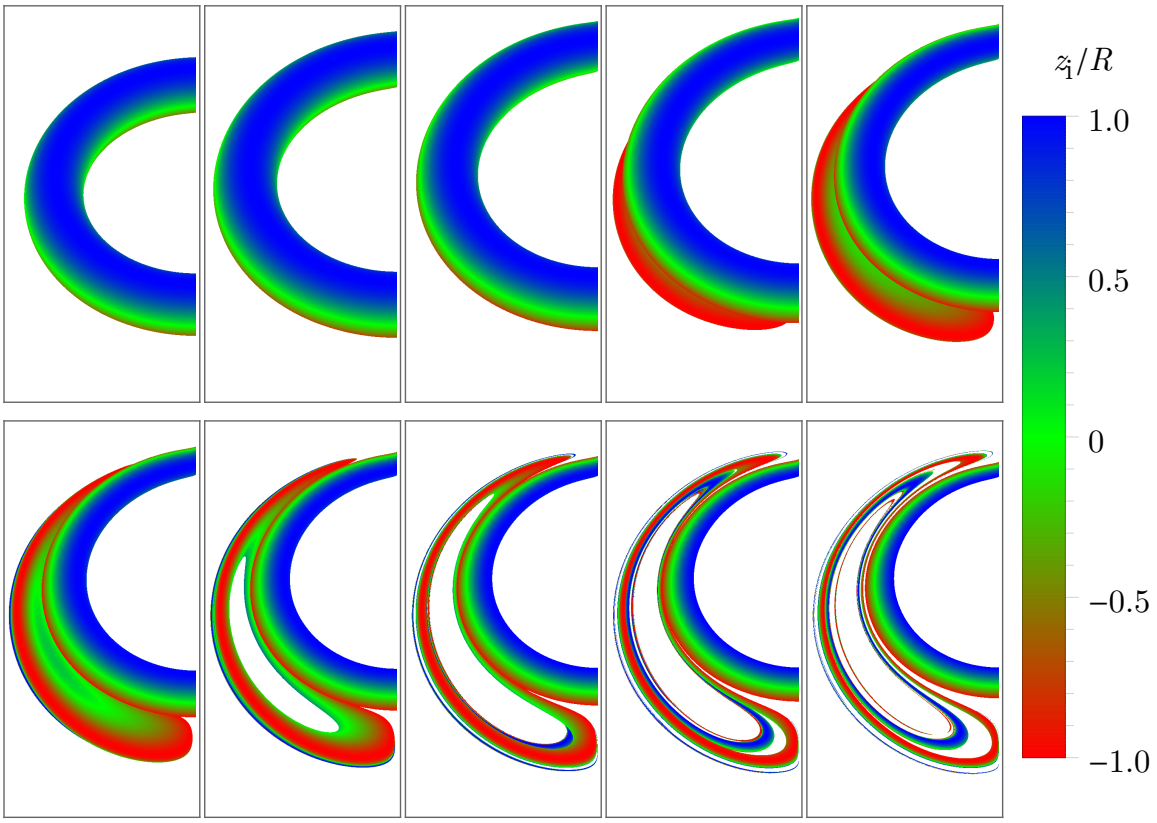

Figure 3.3: Part of the torus from which the given part of the observed image arrives for $\mathcal{M}/b = 0.1, 0.2, ..., 1.0$, from left to right and from top to bottom respectively. For small masses, the observer sees the torus only from the "top" ($z > 0$) but as the mass grows, the curved geodesics go around the torus to show the "bottom" ($z < 0$). The alternating colors along with the growing times in fig. 3.2 indicate that every "new" image corresponds to a geodesic completing another half-loop around the torus.

3.6 The Kerr space-time

In Boyer-Lindquist coordinates t, r, θ, ϕ we have the non-zero inverse metric components

$$\begin{aligned} g^{tt} &= -\frac{\mathcal{A}}{\Delta\Sigma}, \\ g^{rr} = \frac{\Delta}{\Sigma}, g^{\theta\theta} &= \frac{1}{\Sigma}, \\ g^{\phi\phi} &= \frac{\Delta - a^2 \sin^2\theta}{\Delta\Sigma \sin^2\theta}, \\ g^{t\phi} &= -\frac{2Mra}{\Delta\Sigma}, \end{aligned} \tag{3.34}$$

where $\Sigma = r^2 + a^2\cos^2\vartheta$, $\Delta = r^2 - 2Mr + a^2$ and $\mathcal{A} = (r^2+a^2)^2 - a^2\Delta\sin^2\vartheta$. The corresponding pseudo-Newtonian Hamiltonian (3.9) then reads

$$H_{\mathrm{PNK}} = \frac{1}{2\mathcal{A}(1-\omega u_\phi)}\left(\Delta^2 u_r^2 + \Delta u_\theta^2 + \frac{\Delta - a^2\sin^2\theta}{\sin^2\theta}u_\phi^2\right) + \frac{1}{2(1-\omega u_\phi)}\left(\frac{\Delta\Sigma}{\mathcal{A}} + 1\right), \tag{3.35}$$

where $\omega \equiv g^{t\phi}/g^{tt} = 2Mra/\mathcal{A}$. Because of a slightly simpler form, the presented Hamiltonian is equal to 1 for a particle at rest at infinity and thus represents the total particle specific energy including rest mass. The Hamiltonian is exactly equivalent to the Tejeda-Rosswog potential (3.19) at $a = 0$. To obtain a Lagrangian, one must first invert the relation between $\dot{x}^i$ and u_i,[7] namely the non-trivial

$$\dot{\phi} = \frac{\partial H_{\mathrm{PNK}}}{\partial u_\phi} \tag{3.36}$$

However, the resulting Lagrangian is too complicated to be of practical use so we do not give it's form.

3.6.1 Circular orbits in the equatorial plane

When considering the case $\omega u_\phi < 1$ and regions above the horizon $\Delta > 0$, the Hamiltonian is positive-definite in u_θ and u_r and we may use the following effective potential for analysing turning points of orbits in the equatorial plane $\theta = \pi/2$

$$\mathcal{V}_{\mathrm{eff}} = \frac{2a^2(M+r) - 2M\left(u_\phi^2 + r^2\right) + r\left(u_\phi^2 + 2r^2\right)}{2\left(a^2 r + 2aM(a-u_\phi) + r^3\right)}. \tag{3.37}$$

The circular orbits are given by the roots of $\mathcal{V}'_{\mathrm{eff}} = 0$, i.e.

$$r^4 - \frac{u_{\phi(\mathrm{C})}^2}{M}r^3 + (3u_{\phi(\mathrm{C})}^2 - 6au_{\phi(\mathrm{C})} + 2a^2)r^2 - 4Ma(a-u_{\phi(\mathrm{C})})r + a(a-u_{\phi(\mathrm{C})})(u_{\phi(\mathrm{C})}^2 - au_{\phi(\mathrm{C})} + a^2) = 0. \tag{3.38}$$

The discriminant of the polynomial in $u_{\phi(\mathrm{C})}$ in eq. (3.38) is positive for most r and a which means that there are three real u_ϕ corresponding to three distinct circular orbits at almost every r. Two of the roots correspond to the usual families of corotating and counter-rotating orbits[8] and the "third root" corresponds to a particular family of counter-rotating unstable circular orbits (thus yielding them less physical).

The physicality of a given root must also be verified by checking that the circular orbit with $r_{(\mathrm{C})}, u_{\phi(\mathrm{C})}, a$ is above the singularity of the effective potential (3.37), i.e.

$$a^2 r_{(\mathrm{C})} + 2aM(a - u_{\phi(\mathrm{C})}) + r_{(\mathrm{C})}^3 > 0\,. \tag{3.39}$$

[7] Note that the overdot $\dot{x}^i$ in this context again does not mean a proper-time or affine-parameter derivative but a derivative with respect to the new pseudo-time $\tilde{t}$.

[8] When applying the usual cubic formula by hand or in symbolic software such as *Maple* or *Mathematica*, the roots as parametrized by r, a have a more delicate non-smooth structure from which the smooth families of orbits must be "sewn" together.

3.6.2 Angular momentum, frequency and energy of circular orbits

In figure 3.4 the radial distribution of angular momenta of the usual corotating and counter-rotating circular orbits is compared with the exact Kerr distribution (Chandrasekhar, 1998)

$$u_{\phi(\mathrm{K})} = \frac{M^{1/2}r^{1/2} - 2Mar^{-1} + M^{1/2}a^2r^{-3/2}}{\sqrt{1 - 3Mr^{-1} + 2M^{1/2}ar^{-3/2}}}, \tag{3.40}$$

where the counter-rotating case is obtained by $a \to -a$. Both the stable corotating and counter-rotating orbits exhibit very satisfactory agreement with the exact Kerr relation and up to $a \to M$ and $r \approx 4M$ the third $u_{\phi(3)}$ root is too large in magnitude to be of any physical influence.

For $a = M$ there is a minimal magnitude of the third root $u_{\phi(3)} \approx -13M$ at $r \approx 4.3M$ but for smaller a and larger r the value of $u_{\phi(3)}$ rapidly grows in magnitude; for $a = M, r = 5M$ it is around $-45M$ and for $a = 0.8M, r = 4.3M$ it is $\approx -25M$. It should be again stressed that the physical significance of the root is negligible due to the fact that the respective circular orbit is unstable and counter-rotating with respect to the centre.

Nevertheless, figure 3.4 do not show that the behaviour of *unstable* circular orbits (i.e. the sector on the left from the local minimum of the angular momentum distribution) is not very satisfactory. For all values of $a/M \in (0, 1)$ the corotating unstable circular orbits extend all the way to the horizon and take a finite value of $u_{\phi(\mathrm{C})}$ there (this horizon-value diverges as $a \to 0^+$).

Furthermore, the horizon is pathological also because a radially in-falling particle gets frozen there, very much like in the case of the Tejeda-Rosswog potential (Tejeda and Rosswog, 2013) and the exact-relativistic infall as observed from infinity. Hence, the dynamics should be cut off somewhere between the marginally stable orbit and the horizon $\Delta = 0$.

The angular frequency of the orbits is given by $\Omega = \dot{\phi} = \partial H_{\mathrm{PNK}}/\partial u_\phi$ for the pseudo-Kerr case, and for the exact Kerr the angular frequency of corotating circular orbits is given as

$$\Omega = \frac{1}{a + r^{3/2}M^{-1/2}}, \tag{3.41}$$

where only values above the photon circular orbit $r_{\mathrm{ph}} = 2M(1+\cos[2\arccos(-a/M)/3])$ are physical. We only plot a comparison of the corotating case in fig. 3.5 and note that the tendencies of the counter-rotating case are quite similar.

The specific energy of circular orbits in the Kerr space-time reads

$$\mathcal{E}_{(\mathrm{K})} = \frac{r^2 - 2Mr + a\sqrt{Mr}}{r\sqrt{r^2 - 3Mr + 2a\sqrt{Mr}}}. \tag{3.42}$$

The energy of the pseudo-Kerr circular orbits is given simply by substituting $u_{\phi(\mathrm{C})}$ into H_{PNK}. The relations for the corotating case are compared in Figure 3.5. It should be stressed that the plot ranges do not show the growing energies of unstable circular orbits extending to the horizon.

3.6.3 Small perturbations of circular orbits

Let $\delta r, \delta u_r, \delta\theta, \delta u_\theta$ be small deviations from the stable circular orbits. At the point of reflectional symmety $\theta = \pi/2$ all the first $\partial/\partial\theta$ derivatives of the Hamiltonian vanish and for $u_\theta = 0$ first $\partial/\partial u_\theta$ derivatives are also zero. Hence, the linearised equations decouple into two sectors corresponding

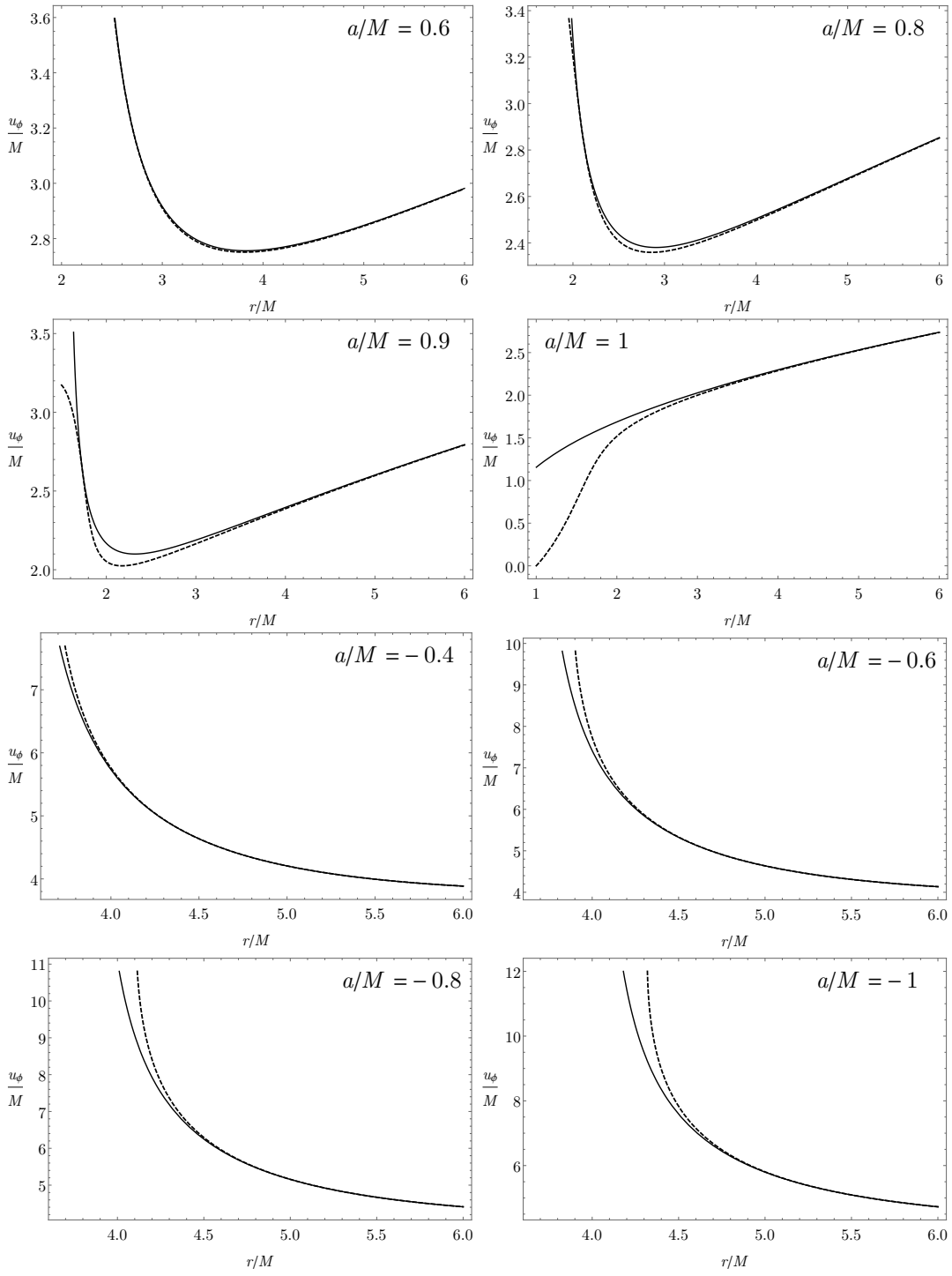

Figure 3.4: Angular momenta u_ϕ of corotating (top) and counter-rotating (bottom) circular orbits of radius r in the Kerr space-time (solid line) compared with the distribution as given by the pseudo-Kerr Hamiltonian (dashed). For $r > 6M$ or $a < 0.6M$ the differences are virtually zero. The ranges for the corotating case are chosen to clearly document the vicinity of the marginally stable orbit.

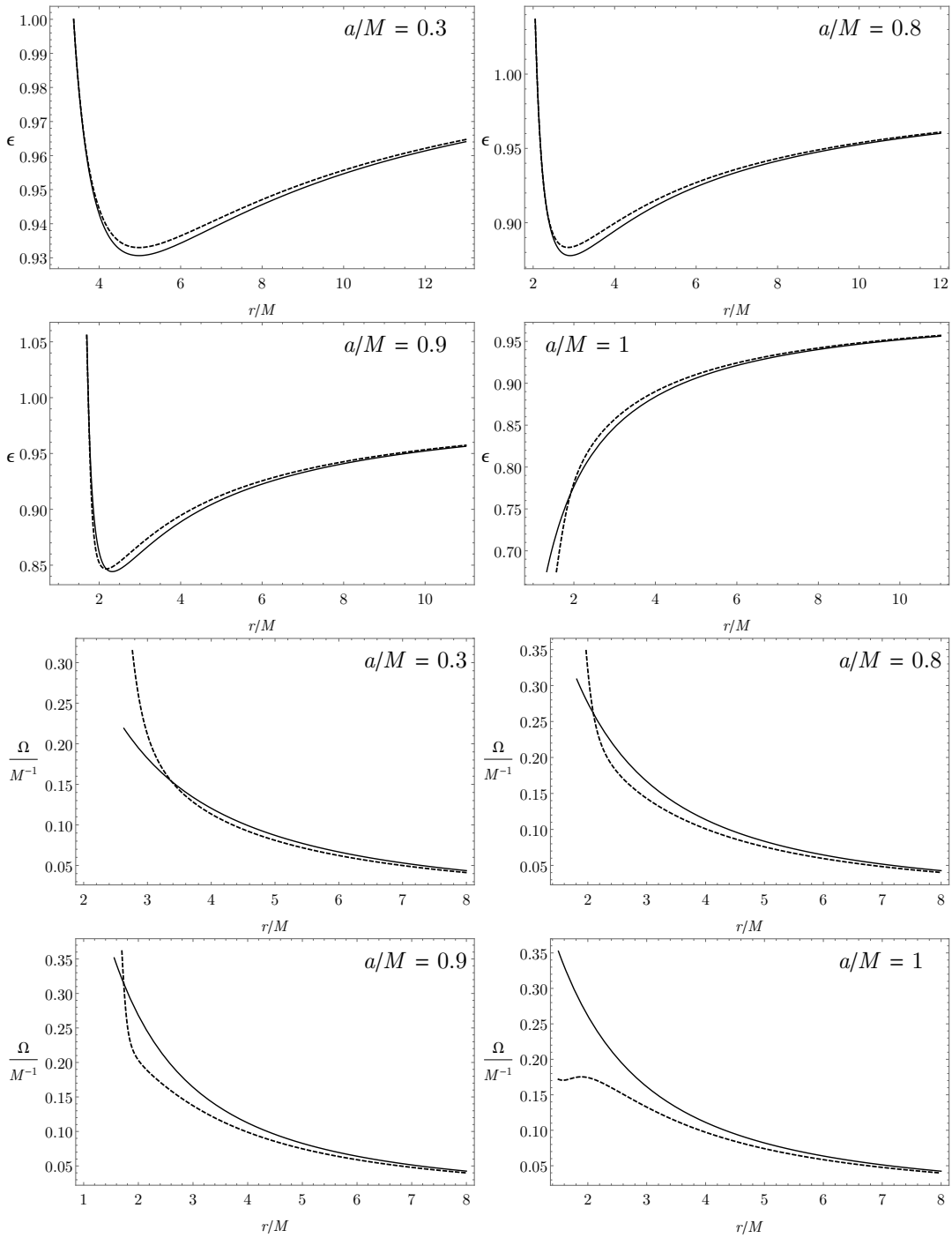

Figure 3.5: Specific energy (top) and angular frequency (bottom) of corotating circular orbits of radius r in the Kerr space-time (full line) compared with the distribution as given by the pseudo-Kerr Hamiltonian (dashed). The plots of the angular frequencies always show the endpoint of the exact-Kerr relation whereas the pseudo-Kerr relations continue to grow up to the horizon. In the specific energy case, the exact-Kerr relation diverges at the endpoint for $a < M$ and thus cannot be depicted.

to the purely radial (epicyclic) and purely vertical oscillations. The equations for the purely radial oscillations read

$$\begin{pmatrix} 0 & -\frac{\partial^2 H}{\partial^2 r} \\ \frac{\partial^2 H}{\partial^2 u_r} & 0 \end{pmatrix} \begin{pmatrix} \delta u_r \\ \delta r \end{pmatrix} = \begin{pmatrix} \delta \dot{u}_r \\ \delta \dot{r} \end{pmatrix}. \tag{3.43}$$

Because we are considering $u_r = 0$, the diagonal terms corresponding to first $\partial/\partial u_r$ derivatives of the Hamiltonian are also zero. Assuming $\sim e^{i\kappa t}$ oscillating solutions we obtain the epicyclic frequency

$$\kappa = \left(\frac{\partial^2 H}{\partial^2 u_r} \frac{\partial^2 H}{\partial^2 r} \right)^{1/2}, \tag{3.44}$$

where the expression is evaluated at $\theta = \pi/2$, $u_r = u_\theta = 0$, $u_\phi = u_{\phi(C)}$. Similarly for the purely vertical oscillations

$$\Omega_{\rm v} = \left(\frac{\partial^2 H}{\partial^2 u_\theta} \frac{\partial^2 H}{\partial^2 \theta} \right)^{1/2}. \tag{3.45}$$

Expressions (3.44) and (3.45) along with the substitution of the appropriate $u_{\phi(\rm C)}$ give the oscillation frequencies analytically. However, the explicit form is rather involved and can be easily obtained via symbolic software so we only compare their values with the oscillation frequencies for the stable corotating circular orbits in the Kerr space-time in fig. 3.6.

The conclusion drawn from the analysis of figures 3.4-3.6 is clear: The correspondence for stable circular orbits is excellent for $a/M \in (0, 0.8)$ and borderline-satisfactory for $a/M \in (0.8, 0.9)$. Furthermore, in the approximate region $a/M \in (0.9, 1)$ both in the exact Kerr space-time and in the pseudo-Kerr dynamics a qualitative transition is taking place. In this region, the precise rate of the transition and the various critical points such as vanishing and appearance of extrema of the various distributions are not faithfully reproduced in the pseudo-Kerr dynamics. On the other hand, even though the quantitative differences are large for $a = M$, the qualitative correspondence is recovered for the extremal case.

3.6.4 Special radii

As already noted, the main issue of the presented pseudo-Kerr Hamiltonian is the non-existence of a photon circular orbit ($u_{\phi(\rm C)} \to \infty$ singularity) above the horizon. However, all the other features such as the marginally stable and the marginally bound orbit are recovered. The marginally stable orbit is given by the zero of the epicyclic frequency $\kappa = 0$ and the marginally bound orbit is given by the specific energy equal to one $H = E_{\rm tot} = 1$. But since the marginally stable orbit has $\delta = 0$ or $\mathcal{E} = 1$, the discussion in Section 3.2 precludes that the marginally bound orbits will be reproduced exactly in the pseudo-Kerr dynamics. Indeed, we have verified by numerical root-finding that the marginally bound is exactly equal to the Kerr value (Abramowicz and Fragile, 2013)

$$r_{\rm mb} = 2M - a + 2\sqrt{M^2 - a^2}. \tag{3.46}$$

The marginally stable orbit vanishes "too soon" in the pseudo-Kerr dynamics, at $a \approx 0.934M$ which can be understood as the ultimate limit of applicability of the presented Hamiltonian. The exact-Kerr marginally stable orbit reads

$$\begin{aligned} r_{\rm ms(K)} &= 3M + Z_2 - \sqrt{(3M - Z_1)(3M + Z_1 + 2Z_2)}, \\ Z_1 &= M + (M^2 - a^2)^{1/3} \left[(M + a)^{1/3} + (M - a)^{1/3} \right], \\ Z_2 &= \sqrt{3a^2 + Z_1^2}. \end{aligned} \tag{3.47}$$

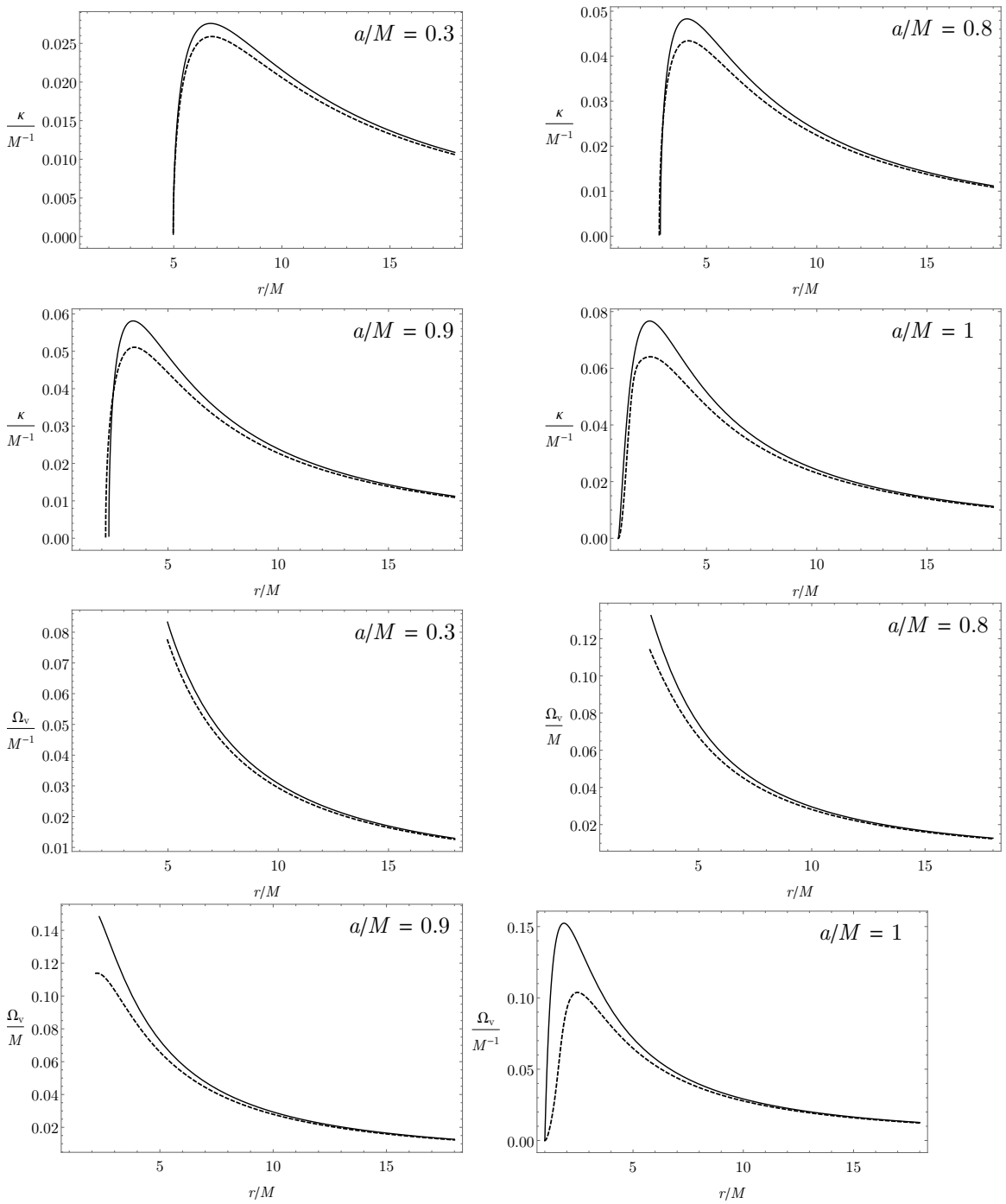

Figure 3.6: Epicyclic (top) and vertical (bottom) oscillation frequency of stable corotating circular orbits of radius r in the Kerr space-time (solid line) compared with the distribution as given by the pseudo-Kerr Hamiltonian (dashed). Even though the relative error is larger than in the case of angular momentum u_ϕ, the qualitative correspondence is satisfied for every value of $a \lesssim 0.8M$. Around $a/M \in (0.9, 1)$ a qualitative transition starts taking place during which the correspondence is broken to be recovered for $a = M$.

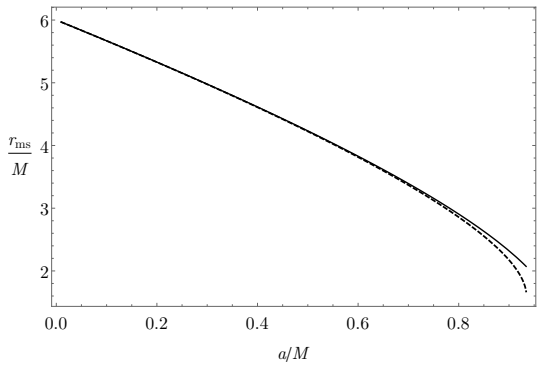

Figure 3.7: Positions of marginally stable orbits $r_{\rm ms}$ in the Kerr space-time (full line) compared with the positions of marginally stable orbits as given by the pseudo-Kerr Hamiltonian (dashed). The exact-Kerr relation continues up to $a = M$ whereas the pseudo-Kerr one ends at $a \approx 0.934$.

The value of $r_{\rm ms}$ for $a/M \in (0, 0.934)$ as obtained by numerical root finding in the pseudo-Kerr dynamics is compared with the exact-Kerr values in Fig. 3.7. Once again we see that the correspondence is very strong for $a \lesssim 0.8$ and reasonable up to $a \approx 0.9M$.

3.6.5 Note on practical simulations

Effective as the Hamiltonian (3.35) might seem, it is also rather complicated and might not be worth the extra computational cost for a large range of situations. Nonetheless, since the presented Lagrangians and Hamiltonians have a seamless Newtonian limit, it is possible to naturally "switch off" parts of the dynamics for different regions of space-time and do not spend computational time on them.

The deviation of the pseudo-Kerr Hamiltonian (3.35) from the Hamiltonian of a test particle in the field of a Newtonian monopole are of two kinds, the static field corrections $\sim M/r$ and $\sim a^2/r^2$, and the dragging term $\sim Mau_\phi/r^3$ (all to leading order in $1/r$). To obtain an estimate independent of u_ϕ and a, we use the leading-order value for a circular orbit $u_\phi \approx \sqrt{Mr}$ and the maximum spin $a = M$ to get $Mau_\phi/r^3 \sim M^{5/2}/r^{5/2}$ and $a^2/r^2 \sim M^2/r^2$. Since we are only interested in $r > M$, we can conclude that the dragging term will always be less significant than the spin-static term $\sim M^2/r^2$.

For the sake of computation-time saving it is then convenient to choose a small dimensionless inaccuracy tolerance ε and switch between the near-blackhole dynamics in the following way[9]. If $M/r < \varepsilon$ use purely Newtonian dynamics; if $\varepsilon < M/r < \sqrt{\varepsilon}$, use the Tejeda-Rosswog dynamics; if $M/r > \sqrt{\varepsilon}$, use the pseudo-Kerr Hamiltonian (3.35).

Since the intrinsic error of the Tejeda-Rosswog and the presented pseudo-Kerr dynamics is at least in orders of units of percent, a reasonable tolerance is $\varepsilon = 0.01$ because then the switch introduces about the same error as the approximate dynamics themselves. Hence, the pseudo-Kerr Hamiltonian should only be used from the near-horizon cut-off up to $r \approx 10M$ and the Tejeda-Rosswog Hamiltonian from $r \approx 10M$ up to $r \approx 100M$. Beyond $r \approx 100M$ it is pointless to use other than Newtonian

[9]Note that in SI units $M \to GM/c^2$ in the following discussion.

dynamics, unless, of course, describing extremely fast objects for which none of the mentioned approximations are suited.

3.6.6 Remarks on the Ghosh-Sarkar-Bhadra Lagrangian

The dynamics presented by Ghosh et al. (2014) are concordant with the presented approach in the idea of a low-δ limit, not, however, in the idea of phase-space reparametrization. Instead of covariant velocity components u_i, the dynamics are constructed by a series of ansatzes using the contravariant (canonically non-conjugate) components u^i. As a consequence, it seems that there is no simple characterization of the Ghosh-Sarkar-Bhadra Lagrangian in terms of geodesic reparametrization.

Nonetheless, the latter approach seems to be plagued by analogous problems as the currently presented one. Namely, the Ghosh-Sarkar-Bhadra Lagrangian

$$L_{\mathrm{GSB}} = \frac{1}{2(r-2M)^2(1+\gamma\dot{\phi})}\left(\frac{r^3(r-2M)}{\Delta}\dot{r}^2 + \Delta r^2\dot{\phi}^2\right) + \frac{M}{r}(1-\gamma\dot{\phi}), \tag{3.48}$$

where $\gamma = 2Ma/(r-2M)$, has a Hamiltonian form complicated beyond usefulness. For the angular momenta of circular orbits $\lambda_{\mathrm{GSB(C)}}$ it holds that

$$\begin{aligned} \lambda_{\mathrm{GSB(C)}} &= \frac{-Q \pm \sqrt{Q^2-4R}}{2}, \\ Q &= \frac{4a^3rM - 6Mar(r^2+a^2)}{a^2r(r-2M) - r(r-3M)(r^2+a^2)}, \\ R &= \frac{M(r^2+a^2)[r(r^3+3a^2) - 2a^2r]}{a^2r(r-2M) - r(r-3M)(r^2+a^2)}. \end{aligned} \tag{3.49}$$

What was not clearly stated or shown in the original paper is the fact that this angular momentum distribution has a singularity at

$$a^2(r_{\mathrm{s}}-2M) - (r_{\mathrm{s}}-3M)(r_{\mathrm{s}}^2+a^2) = 0, \tag{3.50}$$

for which the solution varies quite uniformly from $r_{\mathrm{s}} = 3M$ for $a = 0$ to $r_{\mathrm{s}} \approx 3.1M$ for $a = M$.

Even though the authors state that the marginally bound circular orbit exists up to $a \approx 0.7M$ and that the potential is thus useful up to such values, the angular momentum distribution (3.49) crosses the singularity (3.50) before reaching the marginally bound orbit as early as for $a \approx 0.45M$. Amongst other things, this means that the Keplerian circular orbits have a "singular pause" before reaching the marginally bound orbit and the matter density of a stationary accretion disc would necessarily vanish at the singular $r = r_{\mathrm{s}}$.

Hence, the Ghosh-Sarkar-Bhadra Lagrangian should be considered as useful only for $r \gtrsim 3.1M$, and if the marginally bound orbit is important in the given model, only $a \lesssim 0.45M$ should be considered. The point where even the marginally stable orbit collides with this singularity is $a \approx 0.7M$ (which is probably also the reason why the authors were not able to find the marginally stable orbit beyond that spin) which means that for $a \approx 0.7M$ the dynamics are necessarily cut off strictly behind the marginally stable orbit.

3.7 Conclusion

We have shown that it is possible to formulate a general pseudo-Newtonian limit for general space-times. An obvious benefit of the present approach is a unified framework for the estimate and understanding of errors in the approach of Tejeda and Rosswog (2013, 2014). Even though the original ambition was to extend the results of Tejeda and Rosswog (2013, 2014) to Kerr space-times, the effectivity of the presented limit seems to be, in fact, in the extension to light geodesics; the "time non-diagonal" space-times such as Kerr yield only a marginally satisfactory pseudo-Newtonian limit.

4 Weyl space-times

In this chapter, Weyl space-times are introduced along with disc/ring metric functions relevant for the study in Chapter 6. Additionally, a new gravitational potential for a thick (non-singular) toroid is proposed and the usefulness of the potential function as one of the metric functions in the Weyl metric is discussed.

The core of the study of exact solutions of Einstein equations is the investigation of vacuum and electro-vacuum space-times. In that case, one usually assumes that the sources such as charges, currents and masses are confined to a singular area of the space-time thus providing a mere boundary condition of the otherwise source-less equations.

Consequently, the equations governing the evolution of sources can be easily analysed and are often fulfilled automatically due to the nature of the surrounding (electro)-vacuum solution itself. The last but very non-trivial step is then to interpret the physical nature of the result, the perhaps most common interpretation being the more or less proven assumption that a region around the singularly compressed sources can be cut out and replaced by a non-vacuum solution of a non-singular distribution of sources.

A canonical example of this procedure is the Schwarzschild space-time where glueing a spherically symmetric interior solution to the Schwarzschild vacuum is *imperative* by virtue of the Birkhoff theorem. However, a part which is often overlooked is whether the sources in the interior solution can at least in principle fulfil equations of motion and thus represent a physical situation. As will be shown in this chapter, breaking one rotational symmetry with respect to the static and spherically symmetric Schwarzschild space-time already poses problems in this respect.

4.1 Weyl space-times and their sources

4.1.1 Preliminaries

Weyl space-times (Weyl and Bach, 1922), already briefly introduced in Chapter 3, are described by the Weyl metric ($(-+++)$ signature, $G = c = 1$ units)

$$\mathrm{d}s^2 = -e^{2\nu}\mathrm{d}t^2 + e^{2\lambda-2\nu}(\mathrm{d}\rho^2 + \mathrm{d}z^2) + e^{-2\nu}\rho^2\mathrm{d}\phi^2\,. \tag{4.1}$$

In vacuum, the metric function $\nu(\rho, z)$ satisfies the formal Laplace equation $\Delta\nu = 0$ in cylindrical coordinates

$$\frac{1}{\rho}\nu_{,\rho} + \nu_{,\rho\rho} + \nu_{,zz} = 0\,, \tag{4.2}$$

and $\lambda(\rho, z)$ is obtainable by quadrature from

$$\mathrm{d}\lambda = \rho((\nu_{,\rho})^2 - (\nu_{,z})^2)\mathrm{d}\rho + 2\rho\nu_{,\rho}\nu_{,z}\mathrm{d}z\,. \tag{4.3}$$

The Schwarzschild metric (of mass M) is given in Weyl coordinates as

$$\nu_{\rm schw} = \frac{1}{2}\ln\frac{d_1+d_2-2M}{d_1+d_2+2M} = \frac{1}{2}\ln\left(1-\frac{2M}{r}\right), \tag{4.4}$$

$$\lambda_{\rm schw} = \frac{1}{2}\ln\frac{(d_1+d_2)^2-4M^2}{4\Sigma} = \frac{1}{2}\ln\frac{r(r-2M)}{\Sigma}, \tag{4.5}$$

where

$$\begin{aligned} d_{1,2} &\equiv \sqrt{\rho^2+(z\mp M)^2} = r - M \mp M\cos\theta\,, \\ \Sigma \equiv d_1 d_2 &= \sqrt{(\rho^2+z^2+M^2)^2-4z^2M^2} \\ &= (r-M)^2 - M^2\cos^2\theta\,. \end{aligned}$$

The second versions of the expressions are simply the same as the first, albeit in Schwarzschild coordinates (r,θ) which are related to the Weyl coordinates by

$$\rho = \sqrt{r(r-2M)}\,\sin\theta\,, \quad z = (r-M)\,\cos\theta\,;$$
$$r - M = \frac{1}{2}(d_2+d_1), \quad M\cos\theta = \frac{1}{2}(d_2-d_1).$$

The Schwarzschild-type coordinates (or other spheroidal coordinates such as isotropic coordinates) are more natural for space-times containing a black hole, because the black-hole horizon is represented as a sphere ($r=2M$) in them, whereas in the Weyl coordinates it is a bar on the symmetry axis ($\rho=0$, $|z|\le M$).

Outside of a thin source superposed with the black hole, the complete metric transformed into Schwarzschild coordinates then reads

$$\begin{aligned} {\rm d}s^2 = &-\left(1-\frac{2M}{r}\right)e^{2\hat{\nu}}{\rm d}t^2 + \frac{e^{2\hat{\lambda}-2\hat{\nu}}}{1-\frac{2M}{r}}\,{\rm d}r^2 \\ &+ r^2e^{-2\hat{\nu}}(e^{2\hat{\lambda}}{\rm d}\theta^2 + \sin^2\theta\,{\rm d}\phi^2), \end{aligned} \tag{4.6}$$

where $\hat{\nu}(r,\theta)$ is the potential of the external source and $\hat{\lambda}(r,\theta) \equiv \lambda - \lambda_{\rm Schw}$ with $\lambda_{\rm Schw}$ given by (4.5). In Chapter 6 we will refer to the relativistic superposition of Semerák and Suková (2010, 2012); Suková and Semerák (2013) which was done exactly in these deformed Schwarzschild coordinates r,θ,ϕ

4.1.2 First inverted Morgan-Morgan disc

One of the "external" sources used in this thesis is the so-called Bach-Weyl (BW) ring already introduced in Chapter 3. Another of the used sources is the first of the family of the inverted Morgan-Morgan discs (iMM1) (Morgan and Morgan, 1969; Lemos and Letelier, 1994) with the potential functions

$$\nu_{\rm iMM1} = -\frac{M}{\pi(\rho^2+z^2)^{3/2}}\left(P_1\,{\rm arccot}\,S - P_2 S\right), \tag{4.7}$$

where

$$P_1 \equiv 2\rho^2 + 2z^2 - b^2\,\frac{\rho^2 - 2z^2}{\rho^2 + z^2}\,, \tag{4.8}$$

$$P_2 \equiv \frac{1}{2}\left(3\Sigma - 3b^2 + \rho^2 + z^2\right)\,, \tag{4.9}$$

$$S \equiv \sqrt{\frac{\Sigma - \rho^2 + b^2 - z^2}{2\,(\rho^2 + z^2)}}\,, \tag{4.10}$$

$\mathcal{M}$ and b being mass and Weyl inner radius of the disc, and in this case $\Sigma \equiv \sqrt{(\rho^2 - b^2 + z^2)^2 + 4b^2z^2}$ (λ is not known explicitly).

4.1.3 Einstein equations

We will now investigate the properties of *non-vacuum* Einstein equations of the form

$$R_{\mu\nu} = 4\pi\tilde{T}_{\mu\nu},\ \tilde{T}_{\mu\nu} \equiv 2T_{\mu\nu} - Tg_{\mu\nu}\,, \tag{4.11}$$

where $R_{\mu\nu}$ is the Ricci tensor, $T_{\mu\nu}$ the stress energy tensor and $T \equiv T^{\mu}{}_{\mu}$. In components with respect to the Weyl coordinates t, ρ, z, ϕ the Ricci tensor is similarly to the metric diagonal and the stress-energy tensor must then also be diagonal, which gives us

$$T_{\mu\nu} = T_{(\mu)}g_{\mu\nu}\,, \tag{4.12}$$

where $T_{(\mu)}, \mu = t, \rho, z, \phi$ represent a distribution of the properties of the gravitating sources. For instance, for a perfect fluid in rest with respect to the coordinate time t we have $T_{(t)} = -w, T_{(i)} = P, i = \rho, z, \phi$, where w is the matter density and P the isotropic pressure of the fluid. We will consider a more general case, an *anisotropic* fluid where $T_{(i)}$ are generally not equal. The formal anisotropic fluid can be constructed by superposing equal counter-streaming dust clouds $[s]$ which gives us

$$T_{(\mu)} = \sum_{[\mathrm{s}]} w_{[\mathrm{s}]}(u^{\mu}_{[\mathrm{s}]})^2\,, \tag{4.13}$$

where $u^{\mu}_{[\mathrm{s}]}$ are the four-velocity components of the streams and $w_{[\mathrm{s}]}$ it's matter densities.

4.1.4 Conditions on gravitating dust

The four diagonal Einstein equations (4.11) can be rearranged into the form

$$\begin{aligned} \frac{1}{\rho}\nu_{,\rho} + \nu_{,\rho\rho} + \nu_{,zz} &= 4\pi e^{2\lambda - 2\nu}(T_{(t)} + T_{(\phi)})\,, \\ T_{(\rho)} + T_{(z)} &= 0\,, \\ \mathrm{d}\lambda &= \rho((\nu_{,\rho})^2 - (\nu_{,z})^2)\mathrm{d}\rho + 2\rho\nu_{,\rho}\nu_{,z}\mathrm{d}z\,. \end{aligned} \tag{4.14}$$

This means that the Weyl space-time *cannot* be filled with a perfect fluid (only the $P = 0$ dust possibility is admissible) and that the counter-streaming dust can only stream in the ϕ direction, i.e. *the dust particles move on strictly circular orbits or are static*.

Obviously, one can take $T_{(\rho)} = -T_{(z)}$ non-zero while still fulfilling any of the usual energy conditions but such a possibility would correspond to a very special microscopical composition of the material in strict discord with any realistic situation. Hence, the only viable sources of gravitation in Weyl space-time are azimuthally counter-streaming clouds of particles on circular geodesics. The condition for a circular geodesic $\mathrm{d}^2\rho/\mathrm{d}\tau^2 = 0$ yields up to the case of $\lambda \to \infty$

$$\left(\frac{\mathrm{d}\phi}{\mathrm{d}\tau}\right)^2 = \frac{\nu_{,\rho}\, e^{2\nu}}{\rho(1 - 2\rho\,\nu_{,\rho})}\,, \tag{4.15}$$

However, the condition $\mathrm{d}^2 z/\mathrm{d}\tau^2 = 0$ up to $\nu \to -\infty$, $\lambda \to \infty$ cases yields $\nu_{,z} = 0$. For ν, λ nonsingular we can thus say that a circular orbit is possible if and only if $\nu_{,\rho} \in (0, 1/(2\rho))$ and $\nu_{,z} = 0$. A space-time with a region where both $\Delta\nu \neq 0$ and $\nu_{,\rho}$, $\nu_{,z}$ violate one of these conditions is then necessarily unrealistic as there are no dust particles which could generate the given metric functions.

4.1.5 A note on the linearity of superposition

For the rest of this chapter we will adopt the convention $w(\rho, z) = 4\pi e^{2\lambda-2\nu}(T_{(t)} + T_{(\phi)})$ where we assume that the final solutions ν, λ are such that $e^{2\lambda-2\nu} \in (0, \infty)$ so that the actual distribution of $T_{(t)} + T_{(\phi)}$ is recoverable.

At this point, we would also like to draw attention to a slightly inaccurate assertion circulating throughout literature: It is often stated that sources superpose linearly in the function ν but this is true only for the formal distributions $w(\rho, z)$. By superposing two sources with potentials ν_1, ν_2 we actually obtain a space-time with a non-linearly rescaled mass-energy distribution $T_{(t)}+T_{(\phi)}$ with non-trivial superposition phenomena in source overlaps. For instance, the linear-density ring of Bach & Weyl exhibits directional singularities in both ν, λ in the vicinity of the ring (Semerák et al., 1999b). If one were to superpose this ring into a volume-density $w(\rho, z)$, the actual matter distribution $T_{(t)}+T_{(\phi)}$ in the vicinity of the ring would wildly differ from the values before superposition.

However, there is a certain sense in which the formal distribution $w(\rho, z)$ linearly superposes. The "active gravitational mass" $\mathcal{M}$ as given by the leading term of the asymptotic expansion of an asymptotically flat metric is given by

$$\mathcal{M} = \frac{1}{4\pi}\int_0^\infty \int_{-\infty}^\infty w(\rho, z) 2\pi\rho\,\mathrm{d}\rho\,\mathrm{d}z\,, \tag{4.16}$$

which does linearly superpose for different $w(\rho, z)$. On the other hand, the integration is *not* done over the proper volume of the hypersurface and cannot be given any elegant geometrical interpretation. Similarly, $T_{(t)} + T_{(\phi)}$ cannot be related to the active gravitational mass via a straight-forward proper-volume integral.

4.1.6 Equatorial-plane sources

A useful approximation to numerous astrophysical situations is to consider only matter placed in the equatorial plane $z = 0$ as a surface density[1] $w(\rho, z) = \Sigma(\rho)\delta(z)$ (such as in the case of the iMM1 disc in Subsection 4.1.2). The solution can be then understood as a vacuum solution with the boundary condition

$$\nu_{,z}(\rho, z \to 0^-) - \nu_{,z}(\rho, z \to 0^+) = \Sigma(\rho)\,, \tag{4.17}$$

[1] Here $\Sigma(\rho)$ is a the surface density rather than a metric function!

or in the case of $z \to -z$-symmetric boundary conditions at infinity

$$\nu_{,z}(\rho, z \to 0^{\pm}) = \mp\frac{1}{2}\Sigma(\rho)\,. \tag{4.18}$$

For example, for the iMM1 disc the formal matter density reads

$$\Sigma(\rho) = \frac{2\mathcal{M}b}{\pi^2\rho^3}\left(1 - \frac{b^2}{\rho^2}\right)^{1/2}\,. \tag{4.19}$$

To check whether a distribution of matter is at least loosely physical in the sense of existence of circular orbits, it is sufficient to know the potential $\nu(\rho, 0)$ in the equatorial plane which is given by the quadrature

$$\nu(\rho, 0) = -\int_0^{\infty} \Sigma(\rho)\frac{K[4\rho\rho'/(\rho+\rho')^2]}{\pi(1+\rho/\rho')}\mathrm{d}\rho'\,, \tag{4.20}$$

where $K(m)$ is the complete elliptic integral of the first kind

$$K(m) \equiv \int_0^{\pi} \frac{\mathrm{d}\phi}{\sqrt{1 - m\sin^2\phi}}\,. \tag{4.21}$$

Unfortunately the general properties of $\nu(\rho, 0)$ such as the sign of $\nu_{,\rho}$ are not easily deductible from the properties of Σ so a simple analytical check of the physicality of the surface distribution seems not to be possible. It can only be loosely anticipated that matter at $\rho < \rho_{\mathrm{m}}$ where $\Sigma(\rho_{\mathrm{m}})$ is a maximum of Σ is at peril of being non-physical.

4.2 An ansatz regularization of the Bach-Weyl ring

The Poisson equation (4.14) for the potential ν can be easily solved via usual methods of potential theory as was demonstrated e.g. in Šácha and Semerák (2005). However, for a generic "nice" distribution $w(\rho, z)$ the solution is given as an infinite series of special functions with non-trivial coefficients. In the following section, the converse is being done; a very simple regularization of a vacuum solution is proposed as an ansatz to yield a formally (but not geometrically) complicated distribution $w(\rho, z)$.

Let us recall (Chap. 3) that the potential ν of the infinitely thin BW ring reads

$$\nu_{\mathrm{BW}} = \frac{-2\mathcal{M}K(m)}{\pi\sqrt{(\rho+b)^2+z^2}},\; m \equiv \frac{4b\rho}{(\rho+b)^2+z^2}\,, \tag{4.22}$$

where $\mathcal{M}$ is the ring mass and b it's coordinate radius. It can be easily derived that $m \in [0, 1]$ and that surfaces of constant $m = m_0$ are axially and reflectionally symmetric tori[2] with a centre ρ_{c} and radius R given by

$$R = 2b\sqrt{\frac{1}{m_0}\left(\frac{1}{m_0} - 1\right)},\; \rho_{\mathrm{c}} = b\left(\frac{2}{m_0} - 1\right)\,. \tag{4.23}$$

These tori converge to a ring at $\rho = b$ for $m = 1$ and grow into infinity while asymptotically converging to the axis of symmetry for $m \to 0$.

[2] These can be connected to a surface of a constant toroidal coordinate.

The singularity of the potential (4.22) is caused by the singularity of $K(m)$ at $m = 1$. Hence, we propose a regularization of the form $m \to f(m)$ where $f(m) = m$ below a certain $m_0 > 0$ and at the same time $f(1) < 1$. This means that the exterior of a torus given by (4.23) will be the original vacuum solution while the interior will be modified and the potential non-singular. To avoid source singularities, we further require $f(m)$ to be at least twice differentiable. Generally, if $f(m)$ is k times continuously differentiable, then $w(\rho, z)$ is $k - 2$ times continuously differentiable.

Another heuristic criterion in searching for the "correct" regularization is to impose monotonicity on the function $f(m)$. The elliptic integral K is monotonous in the given ranges so if $f(m)$ is monotonous, then the whole potential will be monotonously decreasing up to the position of the ring which is a behaviour to be expected from a gravitational potential of a natural toroidal cloud of matter. Taking all these criteria into account, we propose a family of regularized toroids parametrized by three additional parameters $m_0 \in (0, 1)$, $\Delta \in (0, 1)$ and $n \in \mathbb{N}_0$ with the potential

$$\begin{aligned} v_{m_0,n,\Delta} &= \frac{-2\mathcal{M}K(\tilde{m})}{\pi\sqrt{(\rho+b)^2+z^2}}, \\ \tilde{m} &= m - \Delta\frac{1-m_0}{n+2}\Theta(m-m_0)\left(\frac{m-m_0}{1-m_0}\right)^{n+2}, \end{aligned} \tag{4.24}$$

where Θ is the Heaviside step function and n is the number of continuous derivatives of the resulting distribution $w(\rho, z)$. The parameter Δ is a deviation parameter of $\tilde{m}$ from m constructed so that when $\Delta < 1$, $\tilde{m}$ is monotonous in m.

Obviously, the distributions $w_{m_0,n,\Delta}$ obtained by applying the Laplace operator to the potentials $v_{m_0,n,\Delta}$ can be far from physical for some parameter ranges. However, we have checked that for the whole set of the given ranges $\Delta \in (0, 1)$, $m_0 \in (0, 1)$ and n at least up to 50, the formal matter distributions $w_{m_0,n,\Delta}$ are everywhere positive.

On the other hand, as we increase the deviation Δ from the Bach-Weyl ring, for a certain $\Delta_{\mathrm{m}} < 1$ a minimum of $w_{m_0,n,\Delta}$ develops at $\rho = b$, $z = 0$ (i.e. the toroid gets hollowed out), and $w_{m_0,n,\Delta}$ touches 0 at a certain $\Delta_{\mathrm{c}} > 1$ beyond which a *negative* matter density appears around $\rho = b$. This was to be expected, since beyond $\Delta = 1$ the potential has a local *maximum* at $\rho = b$ which is a special feature indeed.

The regularization would, however, be associated with either $T_{(\rho)}$ or $T_{(z)}$ negative which is far from plausible. Thus, the only reasonable application of the regularized potential is in Newtonian gravitational theory.

5 Numerical simulation of chaos

The purpose of this chapter is to describe some of the advanced programming techniques and algorithms used in the code employed for the simulations in Chapter 6 (henceforth referred to as "the code" or "the program"). Although this description is far from a full documentation, it may prove to be a useful reference for future users of the code or as an inspiration for a construction of a similar one.

5.1 Geometrical integration

The term geometrical integration (see Hairer et al. (2006)) refers to integrators which conserve a geometrical structure or symmetry of the time-flow[1] Φ_τ of the system with a higher degree of accuracy than a general numerical integrator. In the case of Hamiltonian systems, the geometrical symmetries of the flow include time-reversal symmetry

$$\Phi_{-\tau} = \Phi_\tau^{-1}, \tag{5.1}$$

symplecticity in the sense of push-forwarding the symplectic form

$$\Phi_\tau^* \boldsymbol{\omega} = \boldsymbol{\omega}, \tag{5.2}$$

and in our case also reversibility. Let ζ be a momentum-reversal operator, i.e. $\zeta(p,q) = \zeta(-p,q)$ ($\zeta^2 = \mathrm{Id}$). Then reversibility is expressed as

$$\Phi_\tau \circ \zeta = \zeta \circ \Phi_{-\tau}. \tag{5.3}$$

The conservation of any of the mentioned geometrical properties of the flow by the approximate numerical time-translation $\Psi_\tau \approx \Phi_\tau$ is associated with long-term conservation of integrals and geometrical structures in the phase space (see Hairer and Lubich (2000) for a short review). The basic ideas of proofs of such statements is to show that the flow Ψ_τ is in fact an *exact* flow of a close dynamical system with the given symmetry.

For instance, in the case of symplectic integrators the flow Ψ_τ can be shown to be equivalent to the exact flow of a modified Hamiltonian (Benettin and Giorgilli, 1994)

$$H' = H + \mathcal{O}(h^{r+1}) + \mathcal{O}(nh\mathrm{e}^{-\kappa/h}), \tag{5.4}$$

where h is the integration step, r is the integration order (i.e. $\Psi_h = \Phi_h + \mathcal{O}(h^{r+1})$), n is the number of steps executed, and $\kappa > 0$ is a constant specific to the dynamical system and the integration method. Hence, for h very small the error in energy and generally in all integrals of motion will merely oscillate on an $\mathcal{O}(h^{r+1})$ scale. There are two caveats. First, for chaotic trajectories the integrals may

[1] The time-flow function Φ_τ takes a phase-space point and maps it to the phase-space point into which it evolves in time τ.

be conserved but the difference between the numerical and exact trajectory may blow up nonetheless. Second, the constant κ may become very small for very "wild" parts of phase space such as the vicinity of singularities and the error in energy and integrals may grow considerably.

Similar conservation properties are also true for integrators which aren't symplectic but are reversible with the caveat that such integral conservation *is true only for regular trajectories* (see chapter XI of Hairer et al. (2006)). Once applying a reversible non-symplectic integrator to a non-integrable trajectory, the integrals experience a linear error growth (a "drift"). Nonetheless, for both the reversible and symmetric integrators such drifts seem to be always smaller than for non-geometrical integrators.

In conclusion, the more geometric and symmetry-preserving the integrator, the better the long-term properties. On the other hand, for the accuracy of short-term trajectories, other integration methods such as general Runge-Kutta schemes yield better results.

5.1.1 Explicit symplectic integrators and partitioned methods

Consider a separable Hamiltonian

$$H(p, q) = T(p) + V(q)\,. \tag{5.5}$$

For such a Hamiltonian there exist explicit symplectic methods, i.e. such that can be given as a sequence of explicit arithmetic operations rather than implicit expressions needing to be solved by a method such as fixed-point iteration. The simplest explicit integration method, the so-called symplectic Euler or leap-frog method is of second order and reads

$$q_{n+1/2} = q_n + \frac{h}{2}T'\,, \tag{5.6}$$

$$p_{n+1} = p_n - hV'\,, \tag{5.7}$$

$$q_{n+1} = q_{n+1/2} + \frac{h}{2}T'\,. \tag{5.8}$$

A more familiar "leap-frog" form is obtained by solving for $q_{n+3/2}$ in terms of $q_{n+1/2}$ and eliminating the need to compute q_n, q_{n+1}. Furthermore, because of the possibility of "sewing" over the border q_n, q_{n+1}, it is very useful to compose multiple symplectic-Euler steps with different h. The merit of composing several steps is that in certain cases composing steps with step sizes $h_1, ..., h_n$ can yield an integrator of higher order than the original integrator. The drawback is the fact that some of the steps h_i are often negative and the composition methods are thus more prone to rounding error.

In a preliminary version of the code used for the simulations in this thesis we employed the composition coefficients of Blanes and Moan (2002) with satisfactory results. However, the Blanes-Moan coefficients are given by numerical optimalization and only to 15 digits. As the code was later modified to allow for an arbitrary number of digits, the coefficients A from Yoshida (1990), given to arbitrary precision in terms of polynomial roots, were employed.

This explicit symplectic method of Yoshida was used for the integration of trajectories in the models of black holes with the superposed Bach-Weyl ring $h = (2 \div 5) \cdot 10^{-2} M$ depending on the strength of the ring. However, for the integration through the disc, another method with a variable time step had to be used. It should be noted that the actual integration is actually carried out in cylindrical (not Weyl!) coordinates.

5.1.2 Variable time-stepping

Even though symplectic integration methods with variable time steps exist, they are generally very unpractical and often must be tailored specifically for the problem. On the other hand, the relaxed condition of reversibility yields a flexible and accessible framework for variable time-stepping while preserving the good long-term behaviour of the integrators (Hairer and Söderlind, 2005; Stoffer, 1995).

Inspired mainly by the IGEM integrator of Seyrich and Lukes-Gerakopoulos (2012), the algorithm at the core of the variable-step method of the code is the Gauss collocation method which can be understood as a Runge-Kutta method with the Butcher tableau (see e.g. Iserles (2009)):

$1/2 - \sqrt{15}/10$	$5/36$	$2/9 - \sqrt{15}/15$	$5/36 - \sqrt{15}/30$
$1/2$	$5/36 + \sqrt{15}/24$	$5/36 - \sqrt{15}/24$	
$1/2 + \sqrt{15}/10$	$5/36 + \sqrt{15}/30$	$2/9 + \sqrt{15}/15$	$5/36$
	$5/18$	$4/9$	$5/18$

The Gauss method is a three-step method of sixth order albeit at the cost of being implicit. Nevertheless, the implicitness of the method would be introduced in the time-step control. In our case, the step is decided based on the integrated vector field f rather than it's Jacobian Df as is done in the case of IGEM. The basic step is

$$h = \frac{\epsilon}{||f_1 + f_3||}\,, \tag{5.9}$$

where $f_{1,3}$ is the vector field in the first and third step of the collocation respectively, ϵ is some small constant and[2] $||f|| = \sum |f^i|$.

5.1.3 Disc transition

In the case of the particle flying through the singular potential of the disc an additional "slow down" is added to properly control the integration so that the particle flies in a controlled manner as close to the disc as possible and then can be reflected to the other side. The conditions on the step control to be reversible are relatively flexible, it suffices if the step-controller is a function of the collocation points affine with respect to momentum signs and when it is symmetric with respect to the reversal of order of the collocation points $1, 2, 3 \to 3, 2, 1$. We thus use a step

$$h = \frac{\epsilon}{n(\bar{z})||f_1 + f_3||}\,,\ \bar{z} = \frac{1}{3}\sum_{i=1}^{3} z_i\,, \tag{5.10}$$

where z_i are the cylindrical-z distances from the equatorial plane in collocation points i and

$$n(x) = 1 + \frac{\delta_1}{\delta_2 + x^2} \tag{5.11}$$

is some "slow-down" function, where δ_1, δ_2 are some constants tuned by hand. This modified step is identical to the usual step-control from equation (5.9) for $\bar{z}^2 \gg \delta_1$, while for $\delta_2 + \bar{z}^2 < \delta_1$ the step is contracted; the maximal factor by which the step is contracted with respect to the usual step-control is δ_2/δ_1.

[2] Any norm works in place of $||\cdot||$, the one employed is computationally most light.

This special step-control is designed to let the numerical trajectory approach the singular disc as close as possible without crossing it. When the vertical distance z of the trajectory from the disc falls below some chosen $z_{\min}$, the program estimates whether the particle will cross the equatorial plane in the next κ steps via the vector field $f(x)$ at the current phase-space point x

$$z' = z + \kappa f^z(x) \frac{\epsilon}{||2f(x)||}, \tag{5.12}$$

thus basically using the explicit Euler method with a step of roughly $\kappa\epsilon/||2f||$. Then, if the sign of z' is different than z, instead of evolving the particle by the usual algorithm, the original position is reflected as $z \to -z$. The advantage of this approach is that the particle encounters a "stepping wall" near $z = 0$, the iterative Gaussian collocation does not suffer from the nearby discontinuity and the $z \to -z$ reflection exactly conserves energy. The only point violating the integrator's symmetry is the step estimate of the crossing, but any symmetric reversible stepping would be implicit and difficult to iterate over the discontinuity, with only small benefit to accuracy.

We checked that when the parameters are tuned properly, the error typically oscillates without any drift, as typical for symplectic/reversible-symmetric integrators. In some cases the adjusted step could not compensate for the singularities and a slow linear growth in relative energy error was observed (usually for particles falling into the black hole), but this error only rarely exceeded 10^{-11}. By numerical experiments, we have found the following parameter ranges to be optimal:

$$\begin{aligned} z_{\min} &= (1 \div 5) \cdot 10^{-4} M, \\ \delta_1 &= (10^{-5} \div 10^{-3})\, M^2, \\ \delta_2 &= (10^{-8} \div 10^{-5})\, M^2, \\ \epsilon &= (5 \div 8) \cdot 10^{-2} M, \\ \kappa &= 1 \div 3\,. \end{aligned}$$

Let us add that the Gaussian collocation was found by fixed-point iteration and convergence was confirmed by checking the difference between the current set of collocation points x_i and the previous one $x_{i(\mathrm{p})}$, as given by

$$\Delta = \sum_{i=1}^{s} \sum_{j=1}^{2N} \left| x_i^j - x_{i(\mathrm{p})}^j \right|, \tag{5.13}$$

where $N = 2$ is the number of degrees of freedom. The iteration was stopped whenever $\Delta < 10^{-13}$. Such a tolerance corresponds to an average error of the order of 10^{-14} per collocation component, which is about what can practically be achieved, because spatial position (configuration part of $x \sim r, \theta$) was often larger than 10 (the program operated in units of M), the "distance" Δ includes subtraction of close numbers and we used double precision which stores about 15 digits; $\Delta \sim 10^{-14}$ is then on the level of round-off noise.

5.2 Number representation and templates

One of the main obstacles when constructing the code was the bad numerical behaviour of some of the potentials near their singularities. Rather long and strenuous analyses of Taylor expansions and possibly better formal expressions of the potentials and their derivatives yielded no satisfactory

result. Hence, the newest version of the code was constructed with the possibility of *higher float representations* allowing virtually for an infinite number of digits. For that, the BOOST libraries (Dawes et al., 2014) were used, specifically the `gmp_float` from the *Multiprecision* library.

To be able to switch between different float representations, the code relies on the template feature of the C++ language that allows both classes and functions to operate with generic types. Throughout the whole code, the functions were always defined to operate with a generic number template which would then be chosen during initialization. Thus, the functions and classes are of the generic form:

```
template <typename number>
number Function(number a){
    number b = number(0);
    number c = a+b;
    ...
}
```

Analogously for classes with the difference that the number type such as `double` or `mpf_float` has to be declared during instantiation:

```
template <typename number>
class SomeClass{
    ...
};
...
int main(){
SomeClass<double> DoubleInstantiation;
SomeClass<mpf_float> MpfInstantiation;
...
}
```

After some experimentation, the `double` number type proved to work best for the numerical integration, and higher float representations (30 digits) was used only for internal calculations of some of the potential (and derivatives) functions.

5.3 Objects in program

5.3.1 Abstract classes

To obtain flexible and modular code, another feature of C++ called *abstract classes* or *interfaces* was used. An abstract class is a way to describe the properties of a class such as `Integrator` without being forced to employ a particular implementation of such a class. As a result, one could construct other functions or classes expecting an instance of `Integrator` with the core functions expected from a numerical integration algorithm, but the actually implemented algorithm may be any of the integration methods mentioned in the previous section.

As an example consider the abstract class `Dynamika`[3] (the `number*` indicate pointers to dynamically allocated arrays usually representing state vectors):

[3] Czech for "Dynamics".

```
template <typename number>
class Dynamika{
protected:
    int DIM; // Dimension of the dynamical system
public:
    virtual number hamilton(number* state)=0; // Hamiltonian of state
    virtual number* d_dt(number* state)=0; // time derivatives field
    virtual bool check(number* state)=0;  // checks for singularities
    int giveDIM(){return DIM;}
};
```

An actual implementation of `Dynamika` looks like this:

```
template <typename number>
class HarmonicOscillator : public Dynamika<number>{
... // Definition of hamilton, d_dt, check etc.
}
```

However, one can then define a function to take a pointer at a `Dynamika` instantiation and it will (if properly constructed) work as well with `HarmonicOscillator` as with any other `Dynamika`-implemented dynamical system.

An early version of the code even relied on an implementation of `Dynamika` called `Superpozice` which would superpose a given set of `Dynamika` instants very much in the spirit of Newtonian superposition of gravitating sources or even components of the kinetic energy. However, this solution proved to be computationally inefficient and, in the end, every of the superpositions from Chap. 6 was hardcoded as a separate `Dynamika` implementation.

5.3.2 Sketch of object structure

The main abstract classes in the employed code are

- `Dynamika` representing a dynamical system with it's dimension, Hamiltonian, equations of motion and singularities,
- `Integrator` representing an integration algorithm with all it's parameters including a step constant and an evolution operator. `Integrator` takes an instantiation of `Dynamika` as an argument upon creation which then serves as the system whose dynamical equations are integrated.
- `SectionInstruction` represents the instructions how the data from a single trajectory are to be noted down, what coordinates to write down at which instants, and when to stop the integration. `SectionInstruction` needs an `Integrator` upon construction.
- `Sampling` determines which trajectories are picked for a section or some other investigation. Namely, it has to find out allowed areas of initial conditions, pick from them, compute the rest of coordinates from constraints, determine whether and how to retry a failed integration. `Sampling` takes a `Dynamika` as an argument upon construction mainly to have access to the Hamiltonian.

- `PoincareSections` is basically a coordinating shell taking an instant of `Sampling` and `SectionsInstruction` upon construction using the two to produce a final plot.

Perhaps a slight construction weakness of this hierarchy is the fact that `SectionInstruction` and `Sampling` can, in principle, be constructed with respect to different dynamical systems without any obvious conflict. It is then the responsibility of the user of this hierarchy not to mix objects with different dynamical systems at their cores.

As a result of this object structure it is possible to choose different modules such as "periodic snapshots" for orbit tracks after time-steps $\Delta\tau$, or a $\theta = \pi/2$ surface of section noting down either r, v^r, or r, v^z), and switch between integrators by altering single lines of code.

5.4 Surfaces of section

The two core classes used for the creation of Poincaré surfaces of section in Chapter 6 were `KlasikZSampling`, an implementation of `Sampling`, and `SimpleZSection`, an implementation of `SectionInstruction`, the two joint in the shell `Narezani`, an implementation of `PoincareSections`.

The `KlasikZSampling` sets up the allowed r-area of initial conditions in the section upon creation via an internal function `SetupZOblast` which essentially goes step by step through the $r\,, v^r = 0$, $v^\theta = 0$ initial conditions from some $r_{\min}$ to some $r_{\max}$ and checks whether the energy of such initial conditions (also at some given ℓ) is lower than the $\mathcal{E}_s$ of the surface of section to be constructed. If the energy of the initial condition is higher than $\mathcal{E}_s$, the program assumes that for $v^r \neq 0$, $v^z \neq 0$ the energy can be only higher (i.e. energy is positive-definite and quadratic in velocities) and the respective r is not part of the allowed area. There is an additional loop which identifies the case of disconnected allowed areas.

Once the allowed area is identified, the program has an internal initial condition indicating where it is in the surface of section and gradually returns initial conditions at appropriate $\ell, \mathcal{E}$ quasi-randomly covering the whole surface of section. In the simulations in Chapter 6, `KlasikZSampling` was set to gather around 130 trajectories per section.

The `SimpleZSection` created a single Poincaré surface of section given an initial condition from equatorial intersections in both directions. Since the steps h were sufficiently small, the point recorded in the section was taken simply from the average of the state of the trajectory one step before crossing and of the state immediately after crossing the equatorial plane. The maximal number of points recorded from a single trajectory was generally set to 3600.

Whenever the singularities of the central potential or the ring were closely approached, the integration was stopped and restarted again with a nearby initial condition (given by `KlasikZSampling`) until a sufficient number of points was collected (the singularity-encountering points in the section kept). However, the whole set of intersections generated by a given trajectory was discarded if a relative error in energy turned out to be too large (namely $\gtrsim 10^{-9}$).

6 Pseudo-Newtonian model of a black hole with disc or ring

In this chapter, the chaotization and resonance of orbits in the fields of some classical (velocity-independent) pseudo-Newtonian potentials (Section 6.1) superposed with gravitating discs or rings (Section 6.2) is studied and compared with an analogous relativistic system previously investigated by Semerák and Suková (2010, 2012); Suková and Semerák (2013). The main method of study are Poincaré surfaces of section (see Sections 2.3 and 6.3) even though a case study involving the trajectory time-series is also presented (Section 6.4).

In the following text, the papers Semerák and Suková (2010, 2012); Suková and Semerák (2013); Witzany et al. (2015) of the "Free motion around black holes with discs or rings" series will be denoted as Paper I-IV respectively. The contents of this chapter are vastly similar to those of Paper IV and can be understood as a continuation and expansion of the investigation commenced in the bachelor thesis Witzany (2013).

The whole contents of the stated Paper IV are a result of collective effort of all the authors, but for some parts I should give exclusive credit to the co-authors. Unless stated otherwise, every figure in this chapter was taken from Paper IV as graphically prepared mainly by Oldřich Semerák. Additionally, credit must also be given to Petra Suková who was the one to mainly execute the time-series analysis presented in Subsections 6.4.2 and 6.4.3.

For the convenience of the reader and due to the large number of figures in this chapter, all figures first referred to in a section are included strictly before the beginning of another section.

6.1 Pseudo-Newtonian potentials and their properties

6.1.1 Potentials for static black holes

Pseudo-Newtonian potentials were already briefly mentioned in Chapter 3 in the context of the presented "pseudo-Newtonian limit". Here, we will quickly review some of the "classical" pseudo-Newtonian potentials, i.e. such that reproduce the features of the Schwarzschild space-time and are velocity-independent; these potentials were also a basis of the studied model. In the following, we tested the three potentials

$$V_{\mathrm{PW}} = -\frac{M}{r-2M}\,, \tag{6.1}$$

$$V_{\mathrm{NW}} = -\frac{M}{r}\left(1-\frac{3M}{r}+\frac{12M^2}{r^2}\right), \tag{6.2}$$

$$V_{\mathrm{ln}} = \frac{1}{3}\ln\left(1-\frac{3M}{r}\right). \tag{6.3}$$

The first of these potentials (PW) was introduced by Paczyński and Wiita (1980), the second (NW) by Nowak and Wagoner (1991) and the third (ln) is a potential newly proposed in Paper IV. The

latter logarithmic potential was derived by fine-tuning an ansatz family of logarithmic potentials of the form

$$V_\alpha = \frac{1}{\alpha}\ln\left(1-\frac{\alpha M}{r}\right), \tag{6.4}$$

where the family is constructed so that it always has correct $\sim -M/r$ asymptotics as $r\to\infty$. Trying to find an α best reproducing the properties of circular orbits one finds that

$$\ell_{\rm c}^2 = \frac{M}{r_{\rm c}-\alpha M}, \tag{6.5}$$

where $r_{\rm c}, \ell_{\rm c}$ are the angular momentum and radius of a circular orbit. By chance, this relation is *identical* to the relation between angular momentum and Schwarzschild radius of a circular orbit in the Schwarzschild space-time when $\alpha = 3$. This means, in particular, that a Keplerian disc in the vicinity of the $\alpha = 3$ ln potential will formally have an identical angular-momentum distribution as in the Schwarzschild field.

The Paczyński-Wiita (PW) potential is the "original" pseudo-Newtonian potential and in both it's simplicity and effectivity it serves as a certain benchmark potential. The Nowak-Wagoner (NW) potential is also one of the oldest potentials and was chosen more or less arbitrarily to show what different effects are brought with a significantly different potential.

Other major pseudo-Newtonian substitutes for the black hole include the potentials of Artemova et al. (1996) and the potentials designed for scattering and near-parabolic orbits by Wegg (2012) (the previously mentioned potentials are fine-tuned mainly on circular orbits). The Artemova potentials for non-spinning black holes are (numbered according to the original paper)

$$V_{\rm ABN3} = -1+\sqrt{1-\frac{2M}{r}}, \tag{6.6}$$

$$V_{\rm ABN4} = \frac{1}{2}\ln\left(1-\frac{2M}{r}\right). \tag{6.7}$$

A comparison of the PW, NW and Artemova potentials was performed by Crispino et al. (2011) on the case of scalar radiation emitted from an orbiting source.

The Wegg potentials read (original A,B,C marking again kept)

$$V_{\rm WA} = -\frac{M}{r}\left(1+\frac{3M}{r}\right), \tag{6.8}$$

$$V_{\rm WB} = -\frac{M}{r}\left(\frac{3r}{3r-5M}+\frac{4M}{3r}\right), \tag{6.9}$$

$$V_{\rm WC} = -\frac{M}{r}\,\frac{1+\frac{4M}{r}(3-\sqrt{6})+\frac{20M^2}{r^2}(5-2\sqrt{6})}{1-\frac{M}{r}(4\sqrt{6}-9)}. \tag{6.10}$$

As the potentials were designed to reproduce apsidal precession of near-parabolic orbits, it is no wonder that they may not work so well for the study of bound particles. In early considerations for this study we have studied the Wegg A potential as another simple possibility for simulations. However, the potential has no bound orbits for $\ell < \sqrt{3}M$ and offers simply ℓ-shifted Newtonian dynamics for $\ell > \sqrt{3}M$. The picture of dynamics would thus be very different from the other potentials generating an unstable orbit and a fragile interplay between the centrifugal barrier repelling the particles and the central source devouring them. On the other hand, this potential turns out to perform surprisingly well as e.g. an effective potential for photon scattering (Semerák, 2015).

Even though only the PW, NW and ln potentials were used in the actual simulations, all the other potentials are included in figure 6.3, perhaps the key figure for the current study.

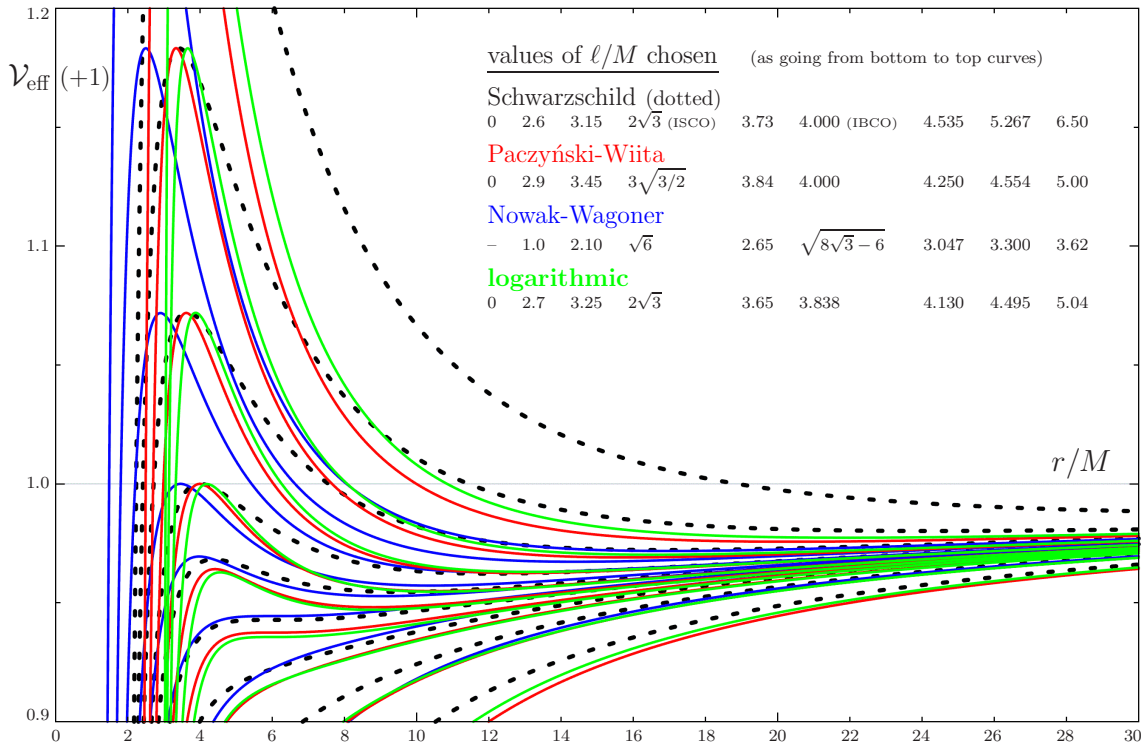

Figure 6.1: Comparison of the three pseudo-Newtonian effective potentials created from the potentials (6.1), (6.2), (6.3) (shifted by one to fit the relativistic case) with the exact Schwarzschild effective potential $\sqrt{(1-2M/r)(1+\ell^2/r^2)}$. The values of ℓ are adjusted so that the curves for different potentials are similar; particularly the fourth curve from top shows the position of the innermost bound circular orbit (IBCO) and the sixth from top the innermost (marginally) stable circular orbit (ISCO). All the three potentials have quite similar shapes with differences in ℓ required to reach certain maxima and shifts in the precise radial positions of the maxima.

6.1.2 Properties important for simulation

Since ℓ is fixed throughout every surface of section, the unperturbed dynamics are best understood through the effective potential

$$\mathcal{V}_{\rm eff} = V(r) + \frac{\ell^2}{2r^2\sin^2\theta}\,. \tag{6.11}$$

Even though we could include the $p_\theta/(2r^2)$ centrifugal term, we anticipate that the θ-symmetry will be broken by the perturbation and p_θ no longer an integral of motion. The boundary of the allowed area on the r, p_r Poincaré surface of section for specific energy $\mathcal{E}$ can then be given as

$$p_r = \sqrt{2(E-\mathcal{V}_{\rm eff})}\,, \tag{6.12}$$

where $\mathcal{V}_{\rm eff}$ is evaluated at $\theta = \pi/2$. This relation will be also true after perturbation with the only exception that $\nu_{\rm E}$ evaluated at $\theta = \pi/2$ will be added to the effective potential. Shapes of effec-

tive potentials in the $\theta = \pi/2$ equatorial plane for various choices of the central pseudo-Newtonian potentials are compared with the exact Schwarzschild case in fig. 6.1.

To observe the difference between the various potentials and their ability to mimic the Schwarzschild space-time, it is also convenient to compare their shapes in the full r, θ plane which is done in figure 6.2.

The feature of the pseudo-Newtonian potentials most important for our study is the exact location of the unstable circular and consequently the homoclinic orbit in the $\mathcal{E}, \ell$ parameter space. The importance of these relations, plotted in fig. 6.3, is twofold.

First, the exact values of $\ell, \mathcal{E}$ for which the surface of section includes the unstable circular orbit is critical in the sense that for larger $\mathcal{E}$ or smaller ℓ the allowed area will be open towards the center and some of the trajectories in the respective surfaces of section will be "sucked" into the black hole. On the other hand, if ℓ is much higher and/or $\mathcal{E}$ much lower than the critical values, then one can be actually surprised not to find any bound trajectories in the respective section because $\mathcal{E}$ is below the minimum of the respective effective potential.

Second, as discussed in Chapter 1, the homoclinic orbit is the point where chaos usually appears first in the phase space under perturbation. In consequence, the proximity of the section parameters to the critical $\ell, \mathcal{E}$ is a good indicator of the degree of chaoticity to be expected in the layer close to the homoclinic orbit.

As a rule of thumb, the PW and ln potentials best reproduce the investigated Schwarzschild features, and all of the other potentials fail in some aspects. Namely, the NW potential is "too weak" with respect to the centrifugal barrier, with the closing-off curve (fig. 6.3) in $\ell, \mathcal{E}$ way below the Schwarzschild case. Moreover, the ln and PW potentials are very similar to each other in the studied respects, which will also be observed in the Poincaré surfaces of section.

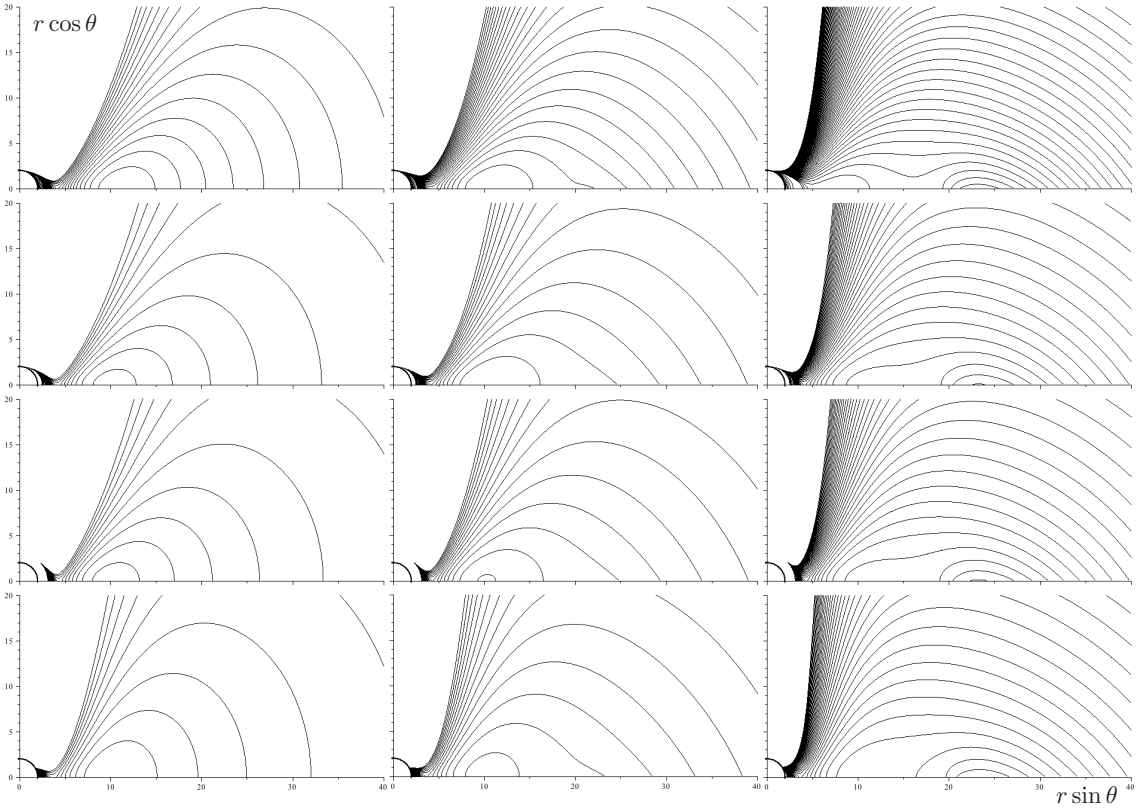

Figure 6.2: Meridional (ϕ = const) plots of the effective potentials (6.11) for various models of a black hole surrounded by the first circumnuclear disc from the inverted Morgan-Morgan family. The exact relativistic superposition, the Paczyński-Wiita, logarithmic and Nowak-Wagoner linear superposition are shown in the first to fourth row one in each row respectively. The values of ℓ are set so that all the potentials have a maximum (the unstable circular orbit) at $\mathcal{E}(+1) = 0.987746$ at $\mathcal{M} = 0$, which means $\ell = 3.9M$ for Schwarzschild, $\ell = 3.9494M$ for Paczyński-Wiita, $\ell = 2.7475$ for Nowak-Wagoner, and $\ell = 3.7805M$ for the logarithmic potential. In each row, the disc mass is varied from left to right as $\mathcal{M}/M = 0, 1, 5$. In all the plots the contours shown are $\mathcal{V}_{\rm eff} = 0, 0.1, 0.2, ..., 0.700, 0.705, 0.710, ..., 1.000$. (In the Newtonian case the effective potential is again shifted to $\mathcal{V}_{\rm eff} + 1$ to match the relativistic case.)

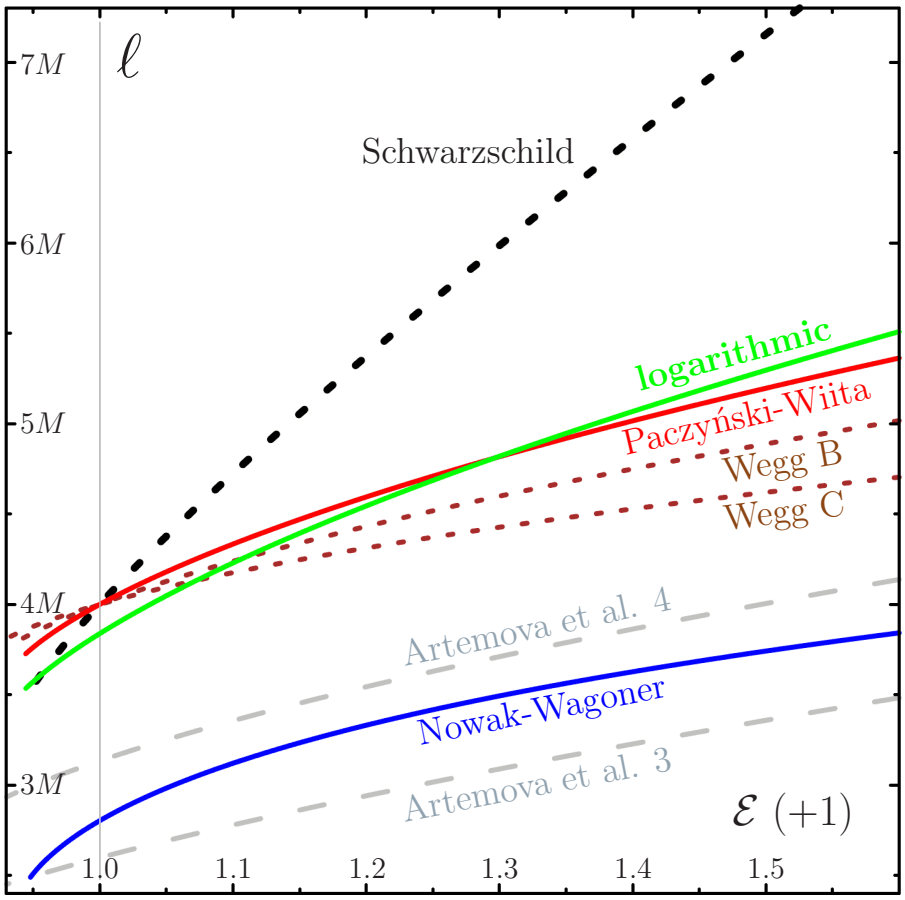

Figure 6.3: The values of angular momentum ℓ needed to raise the centrifugal barrier (and thus the unstable circular orbit) to a given specific-energy level $\mathcal{E}$ plotted for the pseudo-Newtonian effective potentials along with the exact Schwarzschild case (Newtonian energy is shifted as $\mathcal{E}+1$ to fit the relativistic case). The logarithmic and Paczyńsky-Wiita potentials perform the best in this comparison whereas the Nowak-Wagoner potential the worst along with the Artemova ABN3 potential (6.6). The Wegg A potential (6.8) is not included because it does not possess any local maximum of the centrifugal barrier (i.e. it has no unstable circular orbit).

6.2 Superposition with discs and rings

The Weyl metric described briefly in Chapters 3 and 4 possesses a natural analogue of a Newtonian potential, the metric functions ν which satisfy the Laplace equation when interpreting the Weyl coordinates ρ, z, ϕ as usual cylindrical coordinates. However, the transformation between the Schwarzschild r, θ, ϕ and Weyl ρ, z, ϕ does *not* correspond to the transformation between the Euclidean spherical and cylindrical coordinates

$$\rho = \sqrt{r(r-2M)}\sin\theta\,,\ z = (r-M)\cos\theta\,,\ \phi = \phi\,. \tag{6.13}$$

For instance, the $r = 2M$ horizon of the central black hole becomes a bar $\rho = 0$, $z \in (-M, M)$ in Weyl coordinates. Hence, we start with the requirement that the dominant central black hole is spherical in the Newtonian model for which spherical coordinates are the most convenient starting point.

The other important feature observed in papers I-III was that the position of the edge of the disc or the ring was very much important for the dynamics. We thus put another requirement on the Newtonized superposition which is that the Schwarzschild radius of the edge of the disc or the position of the ring should be identical as in the relativistic model. This leaves us with two possible ways of superposing the external sources $\nu_{\rm E}(\rho, z)$ with the pseudo-potentials $V_{\rm PN}$. First, the "Newtonized" superposition

$$H_{\rm N} = T + V_{\rm PN}(r) + \nu_{\rm E}(r\sin\theta, r\cos\theta)\,, \tag{6.14}$$

where T is the usual Newtonian kinetic energy per unit mass in spherical coordinates, the source-radius parameter is set to $b = r_{\rm ring,edge}$ from the relativistic model. The second superposition is the "Weylized" superposition

$$H_{\rm N} = T + V_{\rm PN}(r) + \nu_{\rm E}(\sqrt{r(r-2M)}\sin\theta, (r-M)\cos\theta)\,, \tag{6.15}$$

where the source-radius parameter is set to $b = \sqrt{r_{\rm ring,edge}(r_{\rm ring,edge} - 2M)}$.

The Newtonized superposition is the most straightforward superposition, understandable as a fully Newtonian model with the only substitution of $V_{\rm PN}(r)$ instead of the $-M/r$ Newtonian potential. The Newtonized superposition was utilized in the preliminary studies in the bachelor thesis Witzany (2013). The Weylized superposition, on the other hand, goes a step further in trying to mimic the relativistic situation even though the potential $\nu_{\rm E}(\sqrt{r(r-2M)}\sin\theta, (r-M)\cos\theta)$ certainly does not satisfy the Laplace equation in spherical coordinates.

In the final simulations, we have decided to use the "Weylized" version of the superposition as a more faithful counterpart to the relativistic dynamics. Nonetheless, numerical experiments showed that the difference between these superpositions is virtually non-existent, at least for the sources relatively far away from the central black hole ($r_{\rm ring,edge} \gg 2M$).

The sources superposed with the pseudo-Newtonian potentials are the first of the inverted Morgan-Morgan discs (iMM1) introduced in Chapter 4 ($\nu_{\rm iMM1}$ in equation (4.7)), and the Bach-Weyl ring introduced in Chapter 3 ($\nu_{\rm BW}$ is in equation (3.32))

6.3 Comparing the relativistic and pseudo-Newtonian sections

First, it must be stressed that any kind of quantitative comparison of the relativistic and pseudo-Newtonian dynamics is necessarily only formal since the basic dynamical variables have a completely

different meaning. For instance, the relativistic $\mathcal{E}$ and ℓ are in fact the covariant components of four-velocity $-u_t$, u_ϕ and the equivalence with the Newtonian $\mathcal{E}, \ell$ are drawn only from the Newtonian limit, conditions of which are, however, *not* fulfilled for most of the studied orbits.

For that reason, it is better to observe qualitative rather than quantitative features of the motion, and to take a slightly more reserved viewpoint on the precise pace of evolution of surfaces of section with the parameters $\ell, \mathcal{E}, \mathcal{M}, b$. Furthermore, one is only guaranteed a $C^{1/2}$-type dependence of the structures (recall the discussion of $\mathcal{O}(\sqrt{\epsilon})$ effects in Chapter 1) for regions without singularities and no nice behaviour for invariant structures passing through singularities. Hence, "interpolative" arguments about the observed relations should be done only very cautiously.

The admissible ranges for the parameters are $\mathcal{E} \in (0, \mathcal{E}_{\mathrm{min}}(\ell))$, where $\mathcal{E}_{\mathrm{min}}(\ell, b, \mathcal{M})$ usually around -0.1 is the minimum of the effective potential with the given parameters; $\ell \in (0, \infty)$; $\mathcal{M} \in (0, \infty)$; $r_{\mathrm{disc/edge}} \in (6M, \infty)$, where $r = 6M$ is the position of the innermost stable circular orbit. Even though the full extent of the presented ranges is surely not physical, it is obvious that a complete documentation of even strictly physical parameters is not possible. Instead, the comparison is admissible only on a few slices through the parameter space. Without adhering to any rule, the parameters of surfaces of section were set to formally copy the parameter sets for the energetic and momentum series of Paper I. This means that ℓ was always set to $3.75M$ and r_{edge} or r_{ring} to $20M$ with the other two parameters variable.

In the following, we will concentrate on the Paczyński-Wiita and logarithmic potentials because these two potentials reproduce well the relativistic features for the given parameters. The case of the Nowak-Wagoner potential is then briefly discussed in a special subsection.

6.3.1 Disc-mass influence

Figures 6.4 and 6.5 show the Poincaré diagrams for equatorial orbit transitions in dependence on the iMM1 disc mass $\mathcal{M}$ with the black hole imitated by the Paczyński-Wiita and the logarithmic potential respectively. For convenience of the reader, the respective diagrams for the relativistic model from Paper I are included in figure 6.6. The figures are plotted for the value of specific energy $\mathcal{E} = 0.955 - 1 = -0.045$ and the disc mass $\mathcal{M}/M$ is varied from 0.1 to 1.7.

The most notable difference between the sections is in the qualitative shape of the accessible region; the allowed area for the PW potential is generally "more open" towards the centre whereas the ln potential is "more closed". For the given parameters, the Schwarzschild allowed area is initially closed towards the centre and opens only for $\mathcal{M} \gtrsim 0.5M$. On the other hand, the PW allowed region is open already for zero external perturbation and the ln region opens up towards the centre only for $\mathcal{M} \gtrsim M$. Even so, this does not seem to have such an influence on the invariant structures in phase space, only "sucking out" the chaotic trajectories not held by some invariant barrier[1]. (The diagrams are then asymmetric with respect to $v^r = 0$ because for every "in-falling" trajectory we do not have another "out-flying" trajectory.)

The three systems are strikingly similar, namely, the succession of resonances seems to be identical up to very strong perturbations. For both pseudo-Newtonian potentials, however, the resonances appear slightly earlier in perturbation strengths. In the PW case, the phase-space features show about $0.1M$ to $0.2M$ "earlier" (for accordingly smaller values of $\mathcal{M}$), and in the ln case the structures show up even approximately $0.15M$ to $0.3M$ "early".

[1] Strictly speaking, the trajectories "sucked out" by the centre should not be called "chaotic" but perhaps "chaotically scattered" because they are not bound in the sense of eternally orbiting in a finite portion of phase space.

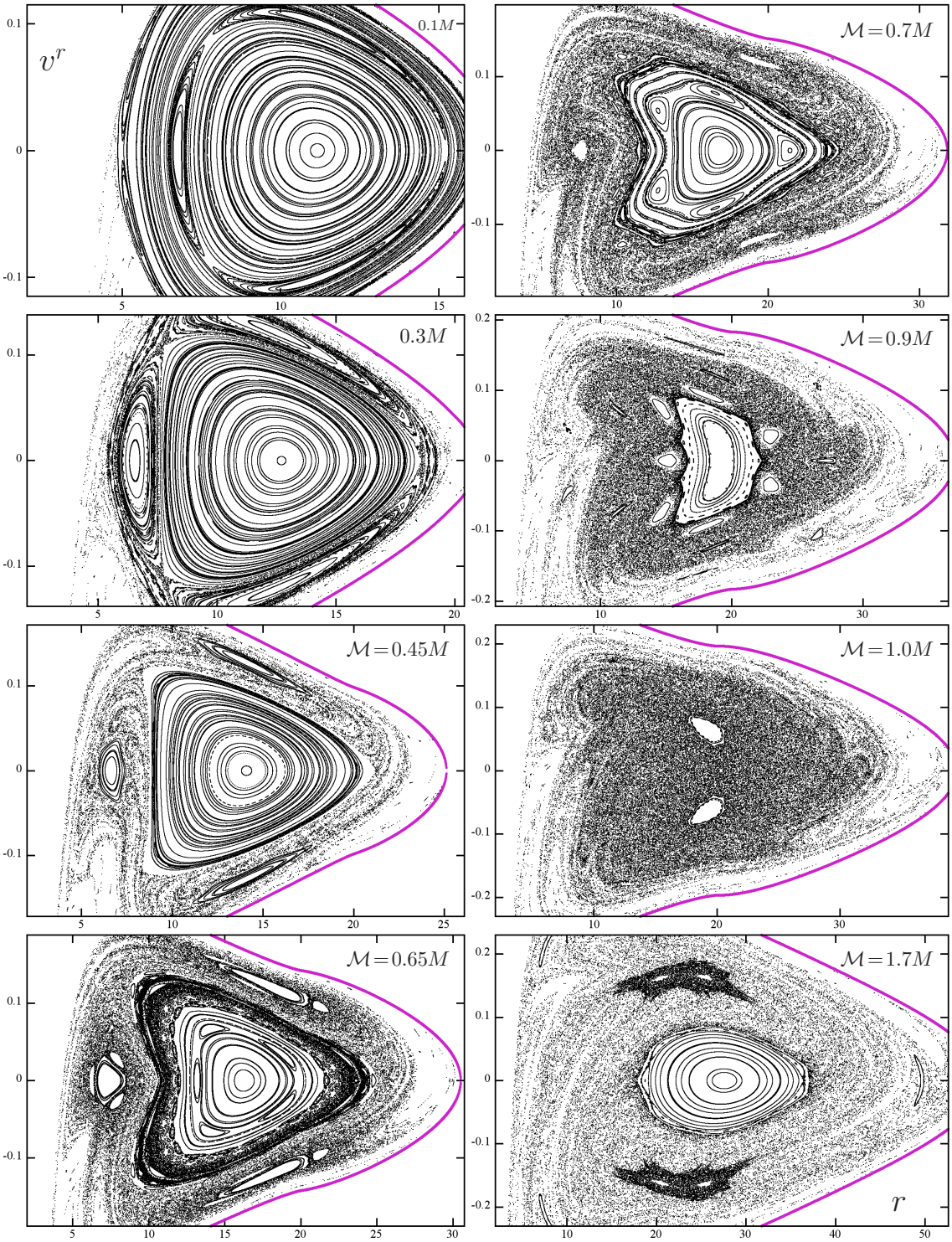

Figure 6.4: Poincaré surfaces of section in the r, v^r variables showing intersections of orbits with conserved specific energy $\mathcal{E}+1=0.955$ and angular momentum $\ell=3.75M$ through the equatorial plane of a centre described by the Paczyńsky-Wiita potential (with mass M) and surrounded by an iMM1 circumnuclear disc with an inner radius $r_{\rm edge}=20M$. Varying disc mass $\mathcal{M}$ is indicated throughout the plots; allowed area is delimited in purple and r axis is in units of M.

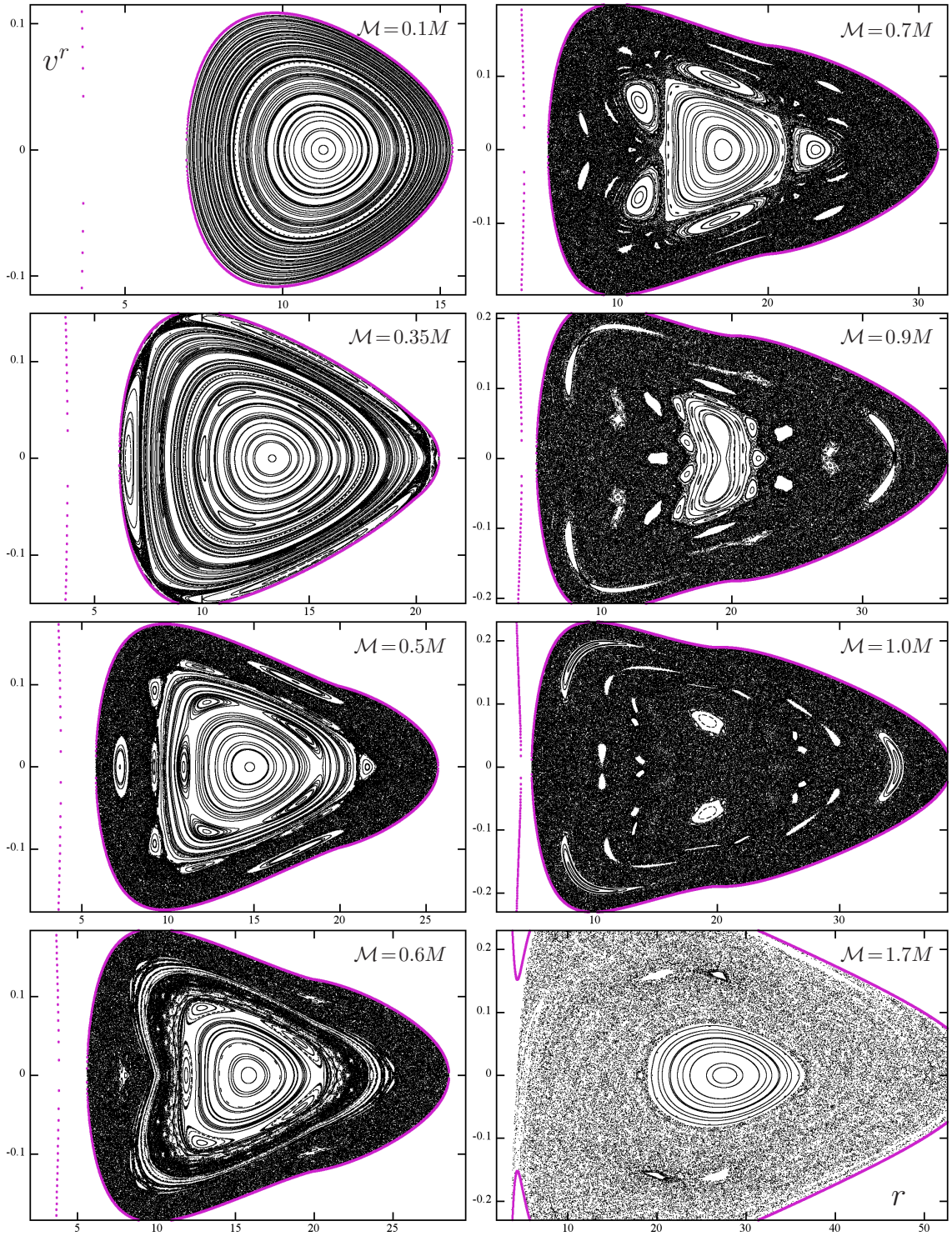

Figure 6.5: The identical series of plots as in figure 6.4 only with the centre simulated by the logarithmic potential (6.3). As discussed more in the text, comparison with figure 6.6 suggests that the evolution of phase space is similar in all three models with various differences in the behaviour of the accessible region and in the evolution of invariant structures.

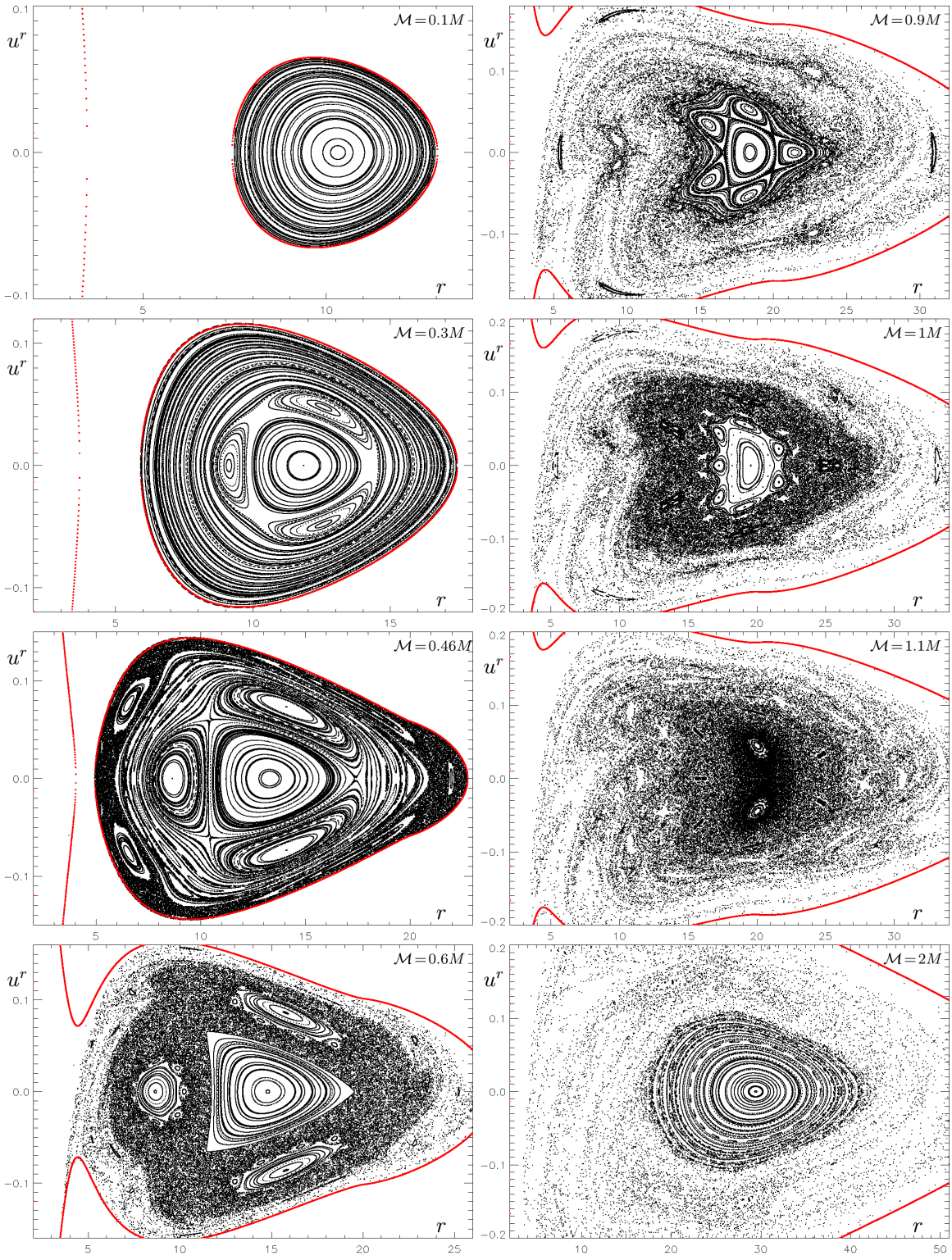

Figure 6.6: The identical series of plots as in figure 6.4 and 6.5 albeit in the exact relativistic framework with non-shifted specific energy $\mathcal{E} = 0.955$. (Taken from Paper I.)

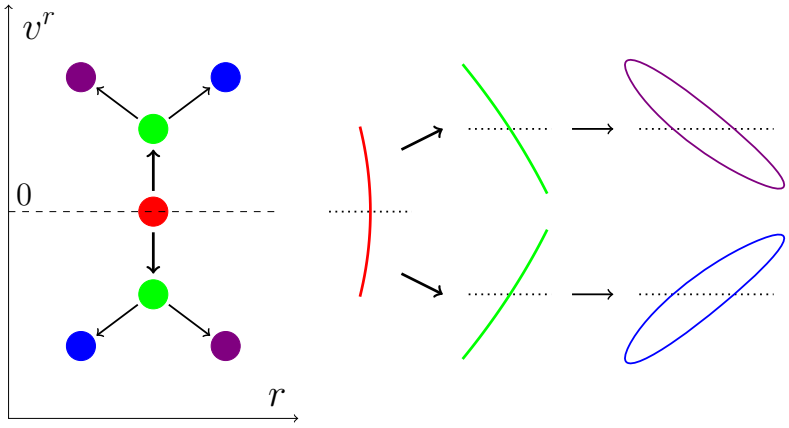

Figure 6.7: A schematic representation of the central-island (1:1 resonance) bifurcation observed in figures 6.4, 6.5, 6.6, i.e. for the both the relativistic and pseudo-Newtonian disc-hole systems. The left part indicated the records left by the "core" trajectories of the islands on the Poincaré surface of section whether the right part is a sketch of the trajectory shapes in the $r\sin\theta, r\cos\theta$ meridional plane in respective colours with the dotted line always representing the equatorial plane $\theta = \pi/2$. Note that the sections of the blue and purple curve would actually depend on the sign of velocity on the loop. The original 1:1 central island (red) first breaks up "vertically" into two islands (green) which afterwards break up into two additional ones (blue and purple). The first break up at $\mathcal{M} \approx M$ in all three models is associated with the central island colliding with the singular disc edge.

Let us now describe the succession of major structures appearing in the surfaces of section, which have been verified by checking the orbit shapes to correspond to identical resonances in all the three dynamics. First, a 3-fold island corresponding to a 2:3 resonance appears; then temporarily a 4-fold resonance corresponding to a set of two 1:2 resonances[2] appears on the periphery of the accessible region (in the PW case the 4-fold island appears and disappears much earlier, and in the ln case the 4-fold structure does not appear at all).

Later, the central regular region successively gives birth to 5-fold, 7-fold, 9-fold, and even a very small 11-fold resonant island corresponding to a 4:5, 6:7, 8:9, and 10:11 resonance respectively (the m from an m:k resonance has to be read off from the trajectory shape in the r, θ plane as is demonstrated in Section 6.4 and figure 2.1 in Chapter 2).

Finally, as the $\mathcal{M}$-parameter flow brings the central island towards the disc edge at about $\mathcal{M} = M$ in all of the three models, the central structure breaks up into two v^r-symmetric islands which later again bifurcate into a set of four islands, all corresponding to a 1:1 resonance. Such a central-island bifurcation is of key importance because the "ground state" taken as a basis for many accretion models is unstable and the hypothesized system would have to undergo a "spontaneous symmetry breaking", i.e. fall towards a solution which does not obey the full symmetry of the Hamiltonian. For even larger $\mathcal{M}$, the central orbit regains stability and the central island exists along with it's 4

[2]Normally, an m:k resonance corresponds to a k-fold island in the surface of section. In this case it is not clear whether a simple 2-fold island appeared for very short $\mathcal{M}$-range to produce the observed structure by a pitchfork bifurcation, or whether the 4-fold island appeared "out of the blue" as a tangent bifurcation.

bifurcated branches.

More specifically, (see fig. 6.7) when one takes any point $r, \dot{r}, \theta, \dot{\theta}$ on the original central orbit (red) and applies reflection $\theta \to \pi - \theta$ and/or velocity reversal $\dot{r} \to -\dot{r}$, $\dot{\theta} \to -\dot{\theta}$, the same central orbit will be obtained albeit at a different phase. Hence, the original central orbit is up to phase symmetric with respect to the discrete symmetries of the Hamiltonian, reflection and reversibility. However, these symmetries are respected only by the phase-space structure as a whole and individual islands may not be symmetric.

Both the bifurcations of the islands then represent a case of the mentioned spontaneous symmetry breaking, because the islands group around the stable equilibria which on their own violate the symmetries of the Hamiltonian. The first bifurcation (green) violates the reflection-symmetry of the Hamiltonian; the 1:1 orbit performs a "skew oscillation" around the equatorial plane, each of the islands corresponding to an orbit with a different skew. The second bifurcations then violates the reversibility of the trajectory, each of the four islands in fact correspond to a tilted "non-collapsed" oscillation with respect to the equatorial plane along with a given orientation on the whole loop. (It should be noted that as always with the surfaces of section in this study, an unambiguous identification of an island with a trajectory is only possible when fixing the sign of $\dot{\theta}$ in the section.)

A final remark is that in the ln-potential system a strong 4:5 resonance (a five-fold island) appears inside the central regular region existing from approximately $\mathcal{M} = 0.33M$ to $\mathcal{M} = 0.62M$ which does not appear in the exact system. In the PW-potential system the same resonance is weaker and appears only for $\mathcal{M} = 0.54M$ to $\mathcal{M} = 0.67M$. For perturbation masses larger than the stated intervals the five-fold chains of resonant islands undergo a sudden interchange between stable and unstable orbits; in this form, however, the resonant chain *is* present in the exact relativistic system.

6.3.2 Energy influence with disc

As will be described in the next Subsection 6.3.3, there is a subtle connection between the energy and perturbing-mass series which means that one also has study the energy series to be able to discern the true influence of the external perturbing source. Figures 6.8 and 6.9 show the energy series at a moderate perturbing mass $\mathcal{M} = 0.5M$, $\ell = 3.75M$, $r_{\text{edge}} = 20M$, and the energy in the interval $\mathcal{E} + 1 \in (0.950, 0.980)$; the analogous series for the relativistic system from paper I is reprinted in fig. 6.10. It should be stressed that even though we use the same symbol for the specific energy in the Newtonian and relativistic case, the relativistic energy of a particle at rest at infinity includes the rest energy and is thus equal to 1, whereas the Newtonian $\mathcal{E}$ of a particle at rest at infinity is 0.

Once again, observing the "major" structures emerging from the central region one sees the sequence of resonances 2:3, 4:5, 6:7, 8:9, and even 10:11 corresponding to 3-, 5-, 7-, 9-, and 11-fold islands respectively, which is *completely analogous* to the perturbing-mass series of sections.

There is even an analogy in the opening of the allowed area towards the centre. The PW potential is always open in the given range, whereas the ln potential is closed up to $\mathcal{E} + 1 \approx 0.971$. On the other hand, the relativistic system opens about halfway through the range at $\mathcal{E} \approx 0.956$.

6.3.3 Connection between energy and disc-mass series

The Newtonian nature of the dynamics allows for a straightforward and quantitative explanation of the correspondence between the changes in sections caused by disc-mass variation and those caused by energy variation. As we fix the total energy with respect to infinity and increase the mass of the disc, we deepen the potential well below the particle, thus necessarily endowing it with more *kinetic*

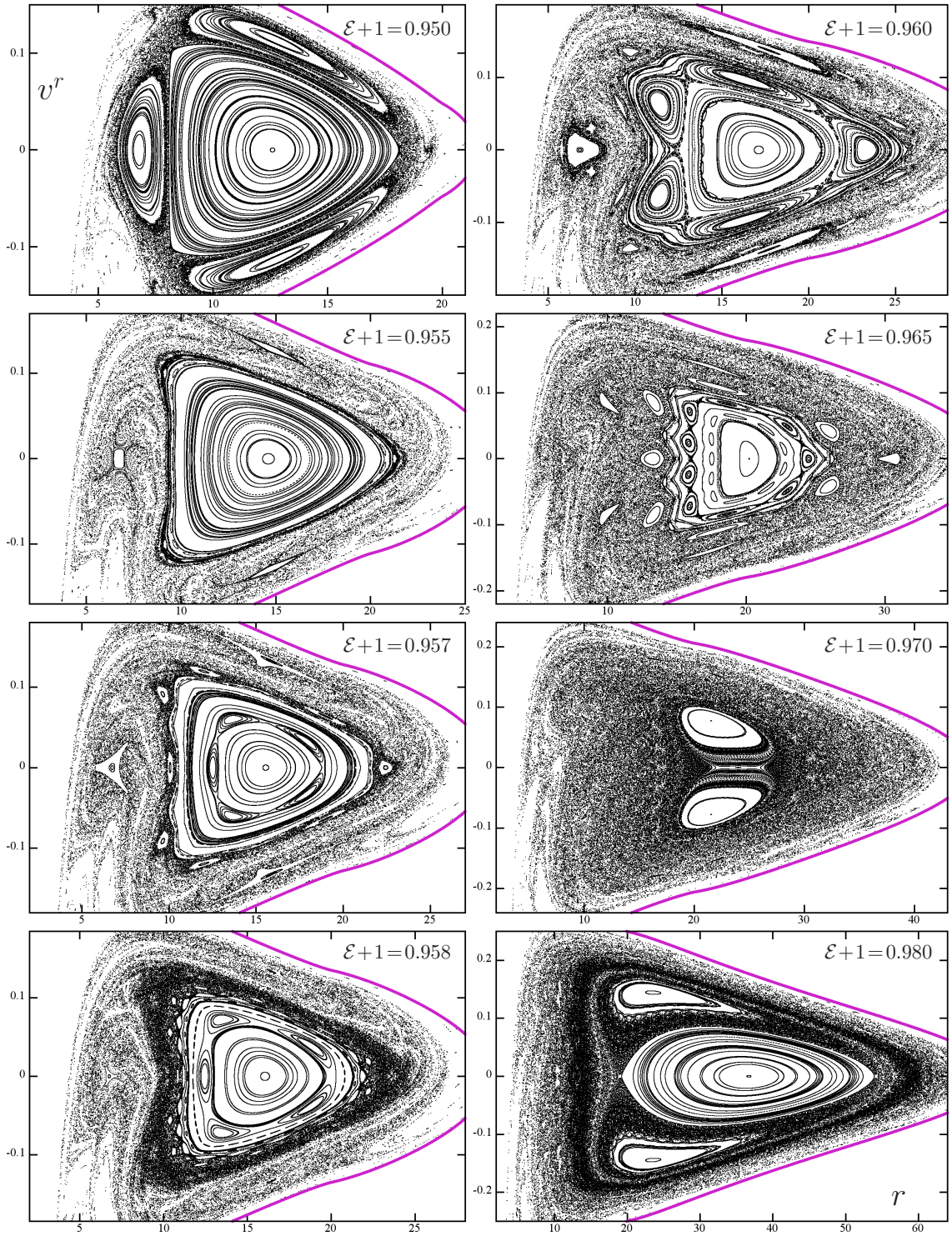

Figure 6.8: Poincaré surfaces of section in the r, v^r variables showing intersections of orbits with angular momentum $\ell = 3.75M$ through the equatorial plane of a centre described by the Paczyńsky-Wiita potential (with mass M) and surrounded by an iMM1 circumnuclear disc with an inner radius $r_{\rm edge} = 20M$ and mass $\mathcal{M} = 0.5M$. Varying specific energy of the orbits in the sections is indicated throughout the plots; allowed area is delimited in purple and r axis is in units of M.

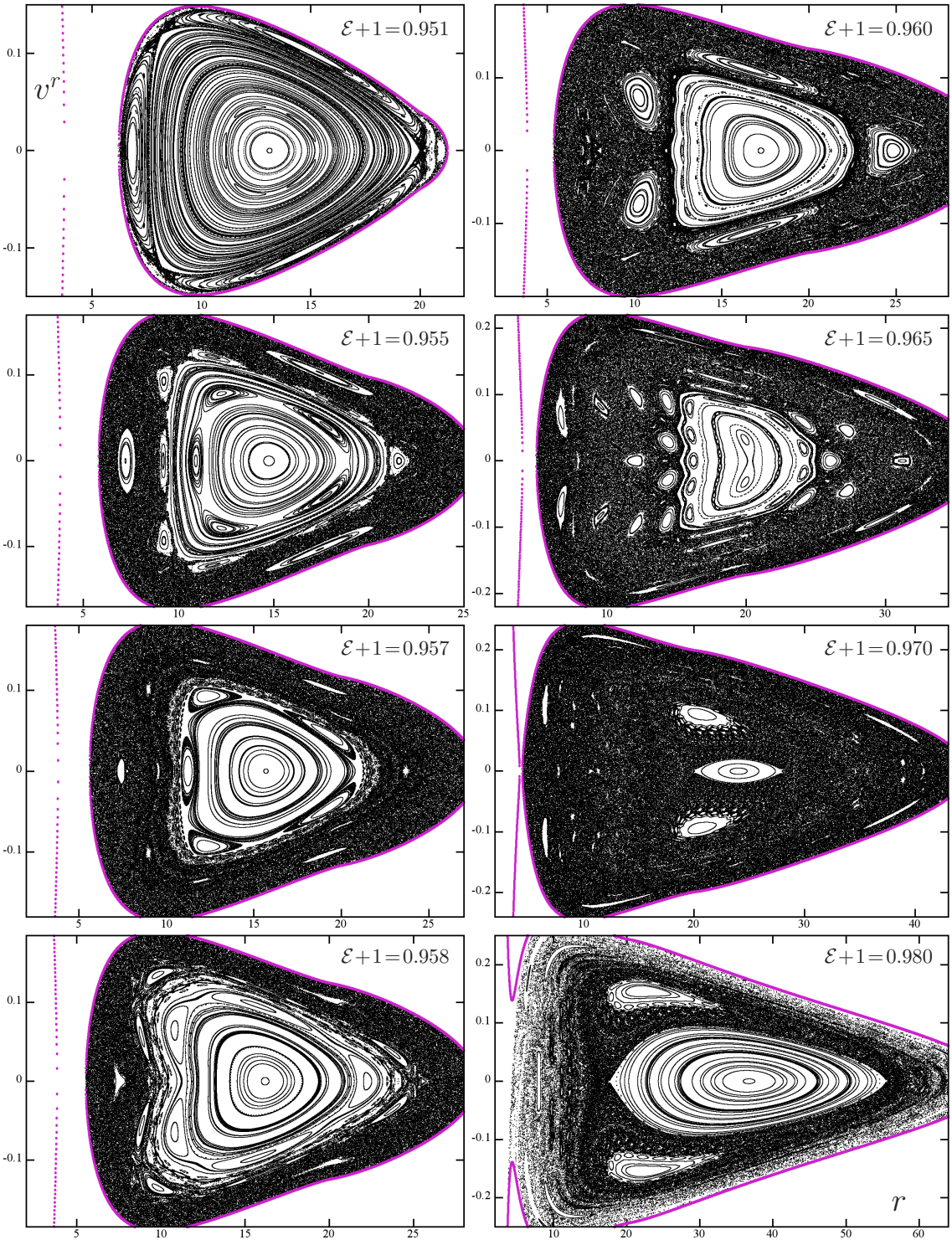

Figure 6.9: The identical series of plots as in figure 6.8 only with the centre simulated by the logarithmic potential (6.3).

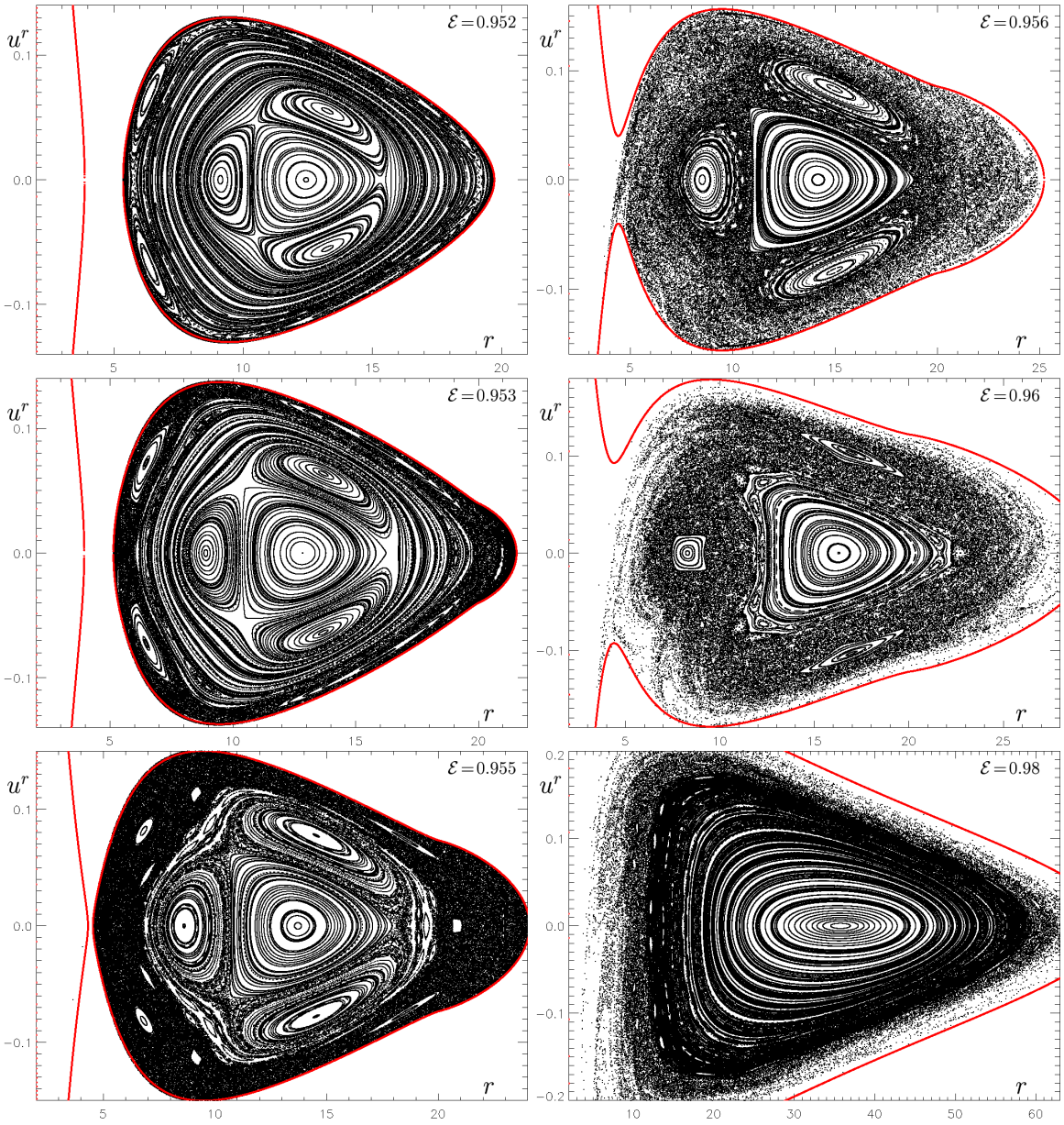

Figure 6.10: The identical series of plots as in figure 6.8 and 6.9 albeit in the exact relativistic framework with non-shifted specific energy $\mathcal{E} = 0.955$. Comparing the three "energetic" series in each of the models again shows that the pseudo-Newtonian potentials well approximate the relativistic situation again with a notable difference in openness/closedness of the accessible region towards the centre and with some minor differences in the phase space structure. (Taken from Paper I.)

energy. Even though a first naive look at the parameters of the perturbing-mass series in figs 6.4 and 6.5 might compel us to think that we study identical ensembles of trajectories with stronger and

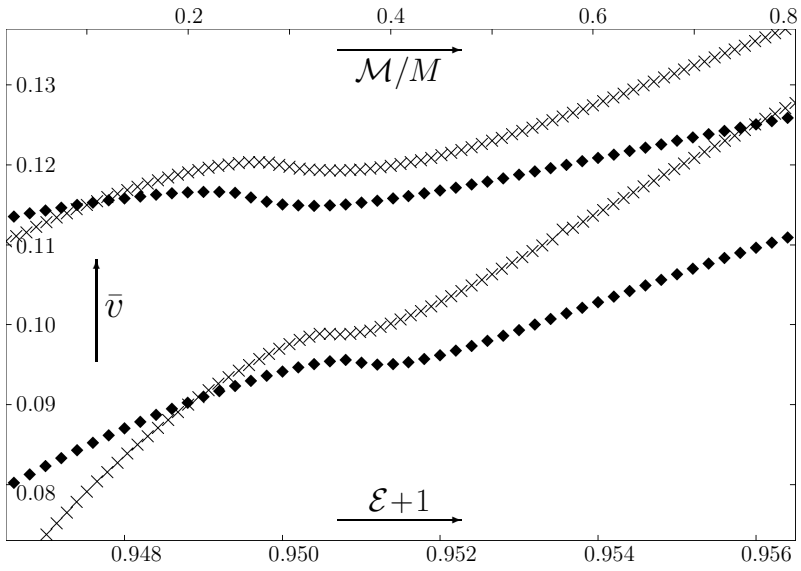

Figure 6.11: Average velocity $\bar{v}$ from eq. (6.16) with which orbits with angular momentum $\ell = 3.75M$ intersect the equatorial plane of the system of a black hole surrounded by a circumnuclear iMM1 disc with inner radius $r_{\rm edge} = 20M$. The dependence of $\bar{v}$ on $\mathcal{M}$ for $\mathcal{E}+1 = 0.955$ is plotted in $\times$ crosses and indicated by the top axis; the dependence of $\bar{v}$ on $\mathcal{E}+1$ for $\mathcal{M} = 0.5$ is plotted in ♦ diamonds and indicated by the bottom axis. The top couple of relations was obtained for the Paczyński-Wiita potential while the two bottom curves were obtained for the logarithmic potential. In both cases the growth is almost monotonous and the $\mathcal{E}$ and $\mathcal{M}$ dependence well correlated; the single "dip" in the relations is always associated with the disc-edge entering the allowed area.

stronger dynamical perturbation, it is not so.

To illustrate this fact we compute the average velocity[3] $\bar{v}(\mathcal{E}, \mathcal{M}, \ell, r_{\rm disc})$ over the equatorial plane for the section parameters of the Newtonian series both in specific energy and perturbing mass. I.e., we take

$$\bar{v}(\mathcal{E}, \mathcal{M}, \ell, r_{\rm disc}) = \frac{\int_{\rm allowed} \sqrt{2(\mathcal{E} - \mathcal{V}_{\rm eff}|_{\theta=\pi/2})} 2\pi r \mathrm{d}r}{\int_{\rm allowed} 2\pi r \mathrm{d}r}, \tag{6.16}$$

and plot the dependence of the result on $\mathcal{M}$ and specific energy $\mathcal{E}$ for the PW and ln potential in figure 6.11. In some cases the allowed region was not closed in the direction towards the black hole in which case we have taken the lowest allowed r to be $5M$. The plots show that for both of the central potentials at the given fixed parameters, $-0.055 \lessapprox \mathcal{E} \lessapprox -0.035$ and $0 \lessapprox \mathcal{M} \lessapprox 0.8M$, the growth of average velocity with either $\mathcal{E}, \mathcal{M}$ is almost identical both in a quantitative and qualitative sense.

Thus, comparing perturbing-mass and energy series in figures 6.4-6.9 suggests an interesting conclusion: The structure of the phase space stays roughly the same for a moderate range of the strength of the disc perturbations and the growing disc mass mostly causes a shift of the considered section

[3] It should be stressed that it is difficult to construct a well-motivated velocity average so we chose one which seemed most natural and simple.

ensemble to higher kinetic energies. This influence on the ensemble is also surely present in the relativistic case studied by Papers I-III but would require a slightly more nuanced argument.

6.3.4 Ring perturbation

The singular ring perturbation cannot be understood as "weak" at any point. As anticipated in Chapter 1, the steep slope of the perturbing potential around the singularity creates a plethora of resonances of various order even at very low ring-mass, and at higher mass the phase space structures are completely defined rather than perturbed by the presence of the ring.

A second concern about the singular nature of the ring is about the Newtonian-relativistic correspondence. The ring in the relativistic case is an ultra-relativistic naked singularity with effects which surely cannot be translated by a naive Newtonian analogy. For instance, the directional singularity of the relativistic Bach-Weyl ring as purported by the metric function λ is not represented anyhow in the Newtonian systems. This means that the quasi-linearity of the superposition is broken even for very small ring masses and that from the very beginning one cannot expect any kind of analogy in the structures in the vicinity of the ring.

The ring-mass series for $\ell = 3.75$, $\mathcal{E} + 1 = 0.977$, $r_{\rm ring} = 20M$ and $\mathcal{M}/M \in (0, 1.1)$ is given for the PW and ln potential respectively in figs 6.12 and 6.13; the respective relativistic series is in figure 6.14 (the beginning of the relativistic mass series is meaningless to compare in detail with the Newtonian picture). As already stated in the disc case, the PW potential is always open towards the centre and the ln potential, on the other hand, opens towards the centre only later than the relativistic case. Also similar to the disc case is the fact that the Newtonian systems exhibit the discussed structures "earlier" in ring-mass than the relativistic system, with the ln-potential system even a little bit earlier than in the PW case.

The beginning of the mass series is marked by a richness of tiny resonances which cannot be compared in detail amongst the system apart from the fact that the overall picture seems to be qualitatively equivalent in all the three studied systems. At $\mathcal{M} \approx 0.03M$, however, in all the systems a structure of a regular central island along with it's 1:1 pitchfork bifurcation starts to grow to at least $\mathcal{M} \approx 0.7M$. The central island then corresponds to a θ oscillation "above" the ring ($r > r_{\rm ring}$), whereas the two-fold island corresponds to a simple "loop" oscillation around the ring. The Newtonian ring-hole models then undergo a short window of another bifurcation of the central island for $\mathcal{M}$ approximately between $0.7M$ and $1.1M$ which then switches back to the normal central island and stays that way for $\mathcal{M}$ at least up to $2M$. From Paper I or the Master thesis Suková (2009) it is not clear whether this "window of central-island bifurcation" happens also in the relativistic system but it is certainly not shown in any of the sections.

The specific-energy series in the ring-perturbed system is then given for $\ell = 3.75$, $\mathcal{M} = 0.5M$, $r_{\rm ring} = 20M$ and $\mathcal{E} + 1 \in (0.915, 0.985)$ is given for the PW and ln potentials respectively in the more compact figures 6.15 and 6.16; the analogous relativistic series is shown in figures 6.17 and 6.18. As a rule of thumb, if a structure interacts closely with the ring, it will not be reproduced across the systems (not even in-between the Newtonian ones!), and if it does not interact closely with the ring, it sometimes will be present across the different ring-hole models.

We will only discuss the overall picture and the fate of the central island. For low energy, the "original" region with the central orbit is disconnected from the ring's potential well or it doesn't exist whatsoever (ln potential, relativistic case). As higher energy levels are browsed, the ring well and the original central well connect; the connection, however, is associated with an unstable orbit between the ring and the central black hole. (It should be stressed that this "new" unstable orbit is

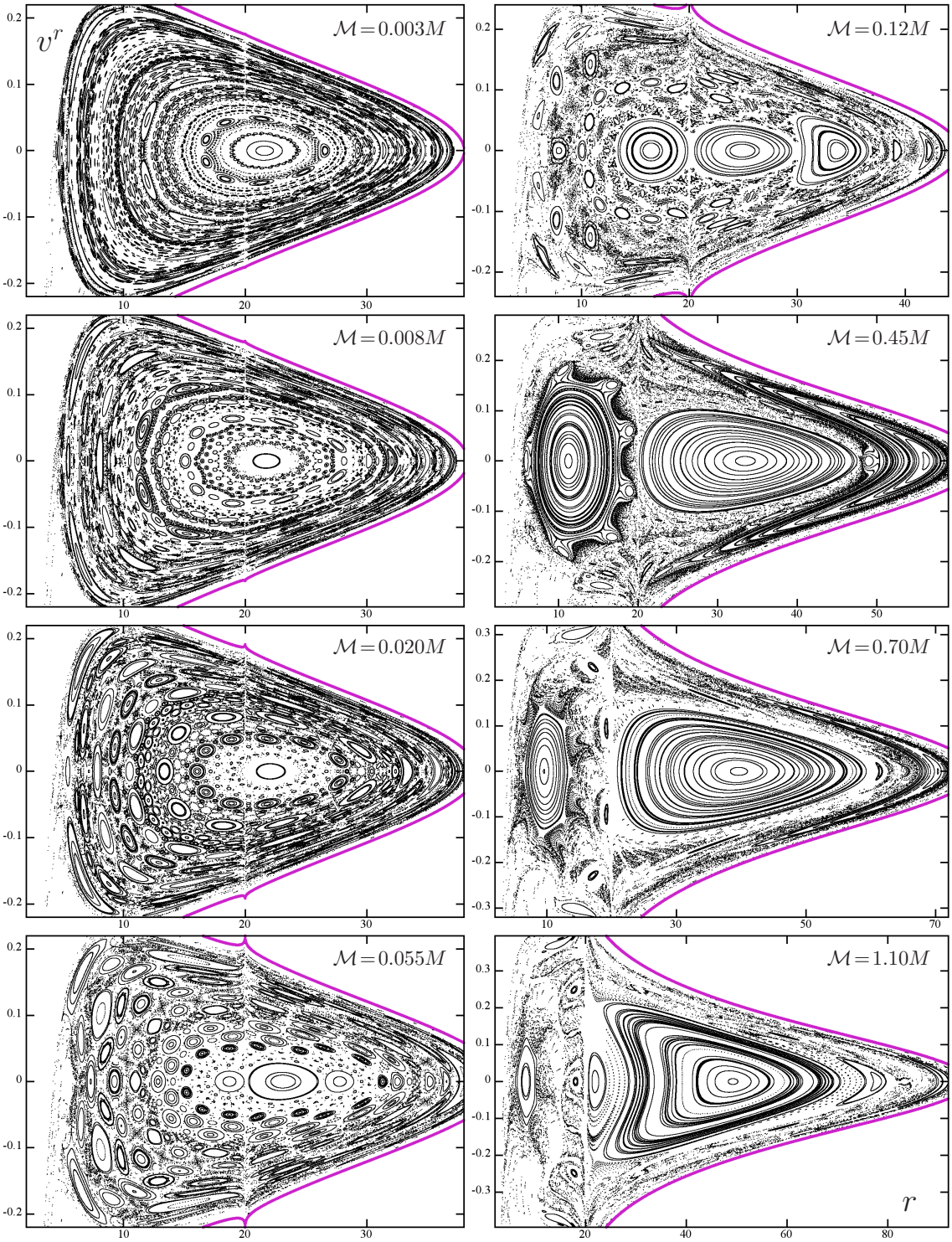

Figure 6.12: Poincaré surfaces of section in the r, v^r variables showing intersections of orbits with conserved specific energy $\mathcal{E}+1=0.977$ and angular momentum $\ell=3.75M$ through the equatorial plane of a centre described by the Paczyński-Wiita potential (with mass M) and surrounded by a BW circumnuclear ring of radius $r_{\rm ring}=20M$. Varying ring mass $\mathcal{M}$ is indicated throughout the plots; allowed area is delimited in purple and r axis is in units of M.

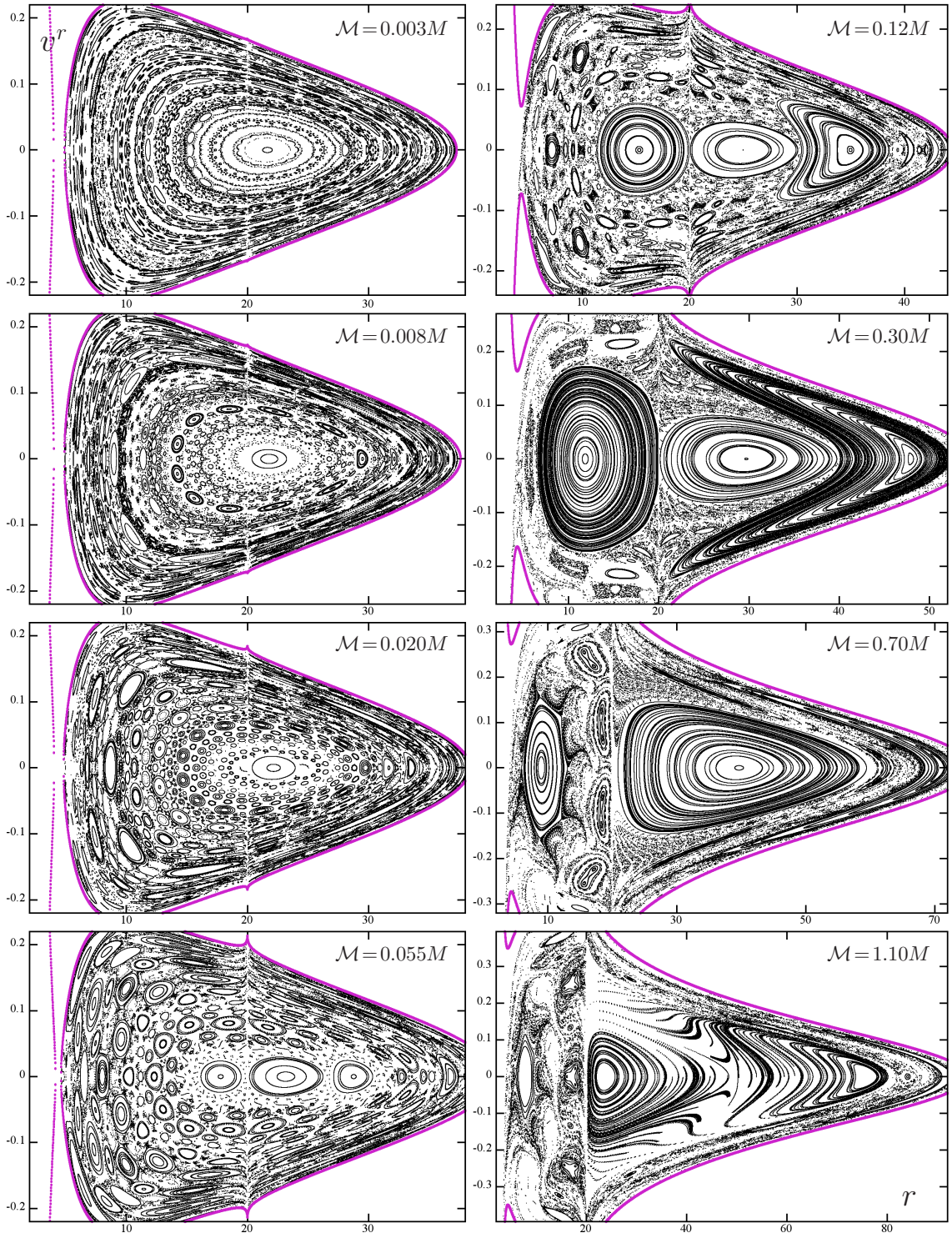

Figure 6.13: The identical series of plots as in figure 6.12 only with the centre simulated by the logarithmic potential (6.3).

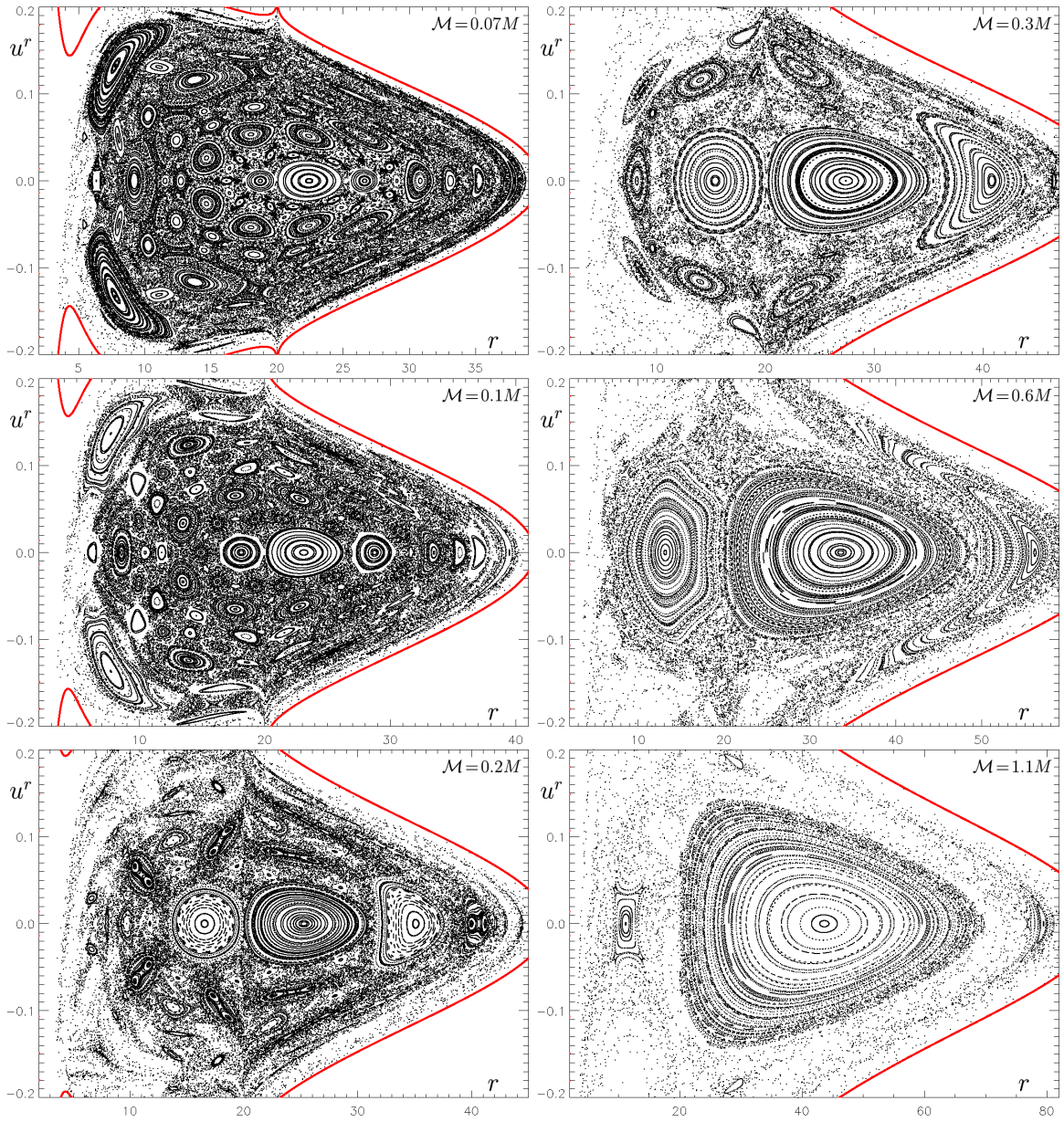

Figure 6.14: The identical series of plots as in figure 6.12 and 6.13 albeit in the exact relativistic framework with non-shifted specific energy $\mathcal{E} = 0.977$ and only for larger ring masses. The three systems vary in a number of quantitative details with some common dominant structures discussed in the text. (Taken from Paper I.)

a *different* unstable circular orbit than the "original" unstable circular orbit!) Hence, the energetic levels around the connection occurring at $\mathcal{E}(+1) \approx 0.925$ is associated with a homoclinic tangle and separatrix chaos.

For higher energies, the central island is forced to move to larger radii and collides with the ring

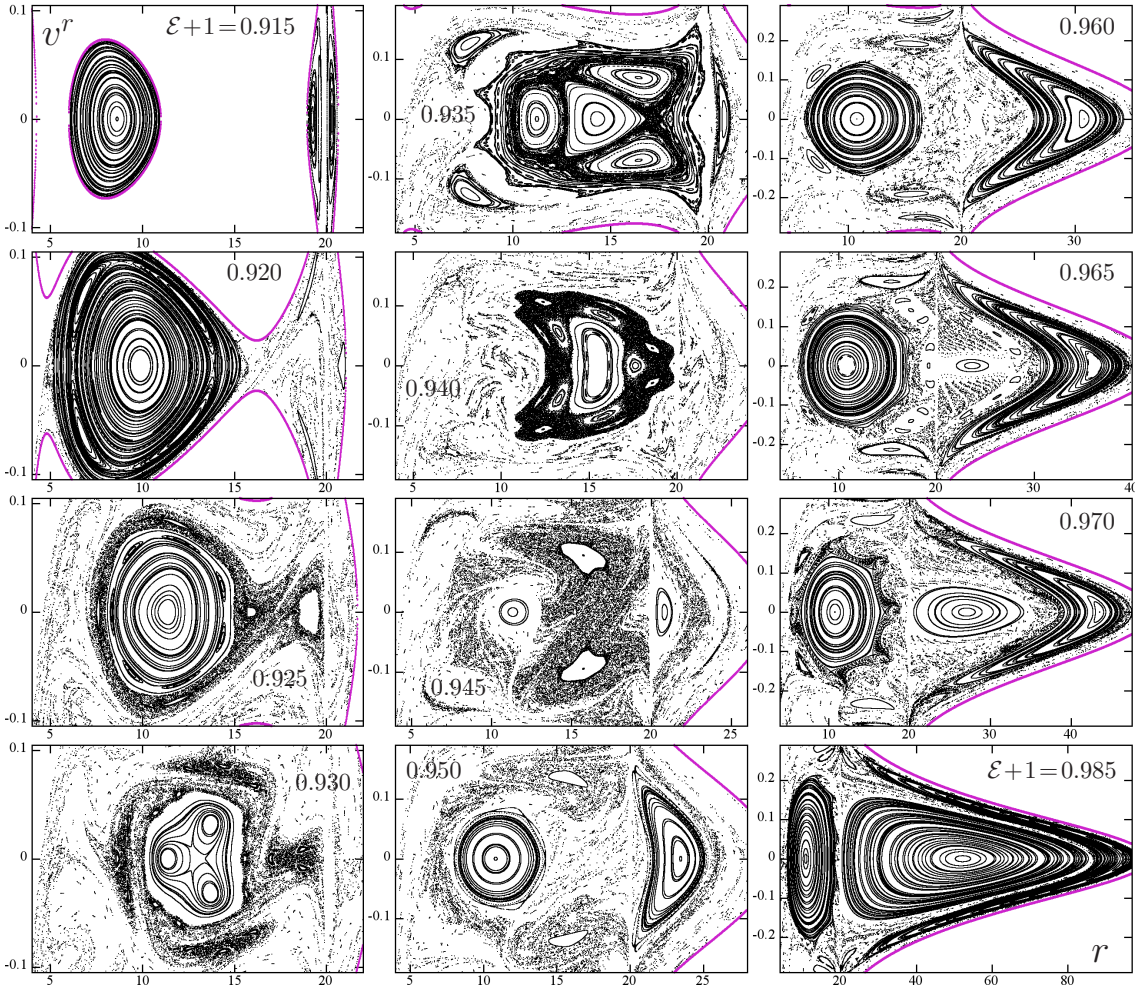

Figure 6.15: Poincaré surfaces of section in the r, v^r variables showing intersections of orbits with angular momentum $\ell = 3.75M$ through the equatorial plane of a centre described by the Paczyńsky-Wiita potential (with mass M) and surrounded by an BW circumnuclear ring with inner radius $r_{\rm ring} = 20M$ and mass $\mathcal{M} = 0.5M$. Varying specific energy of the orbits in the sections is indicated throughout the plots; allowed area is delimited in purple and r axis is in units of M. For some sections, there are two disconnected allowed regions.

"from below". This transitional region from $\mathcal{E}(+1) \approx 0.930$ to $\mathcal{E}(+1) \approx 0.950$ has a completely different scenario in every system because the dominant structures are closely interacting with the ring. For $\mathcal{E} + 1 \approx 0.945$ in the PW and ln system, and for $\mathcal{E} \approx 0.955$ in the relativistic system, a characteristic structure of a 2-fold island corresponding to a 1:2 resonance and a 2-fold island corresponding to a 1:1 bifurcated resonance (familiar with the one from the ring-mass series) forms. Additionally, for $\mathcal{E}(+1) \approx 0.965$ the central island re-emerges "above" the ring as familiar from the perturbing-mass series and this structure of the bifurcated 1:1 resonance along with the central island

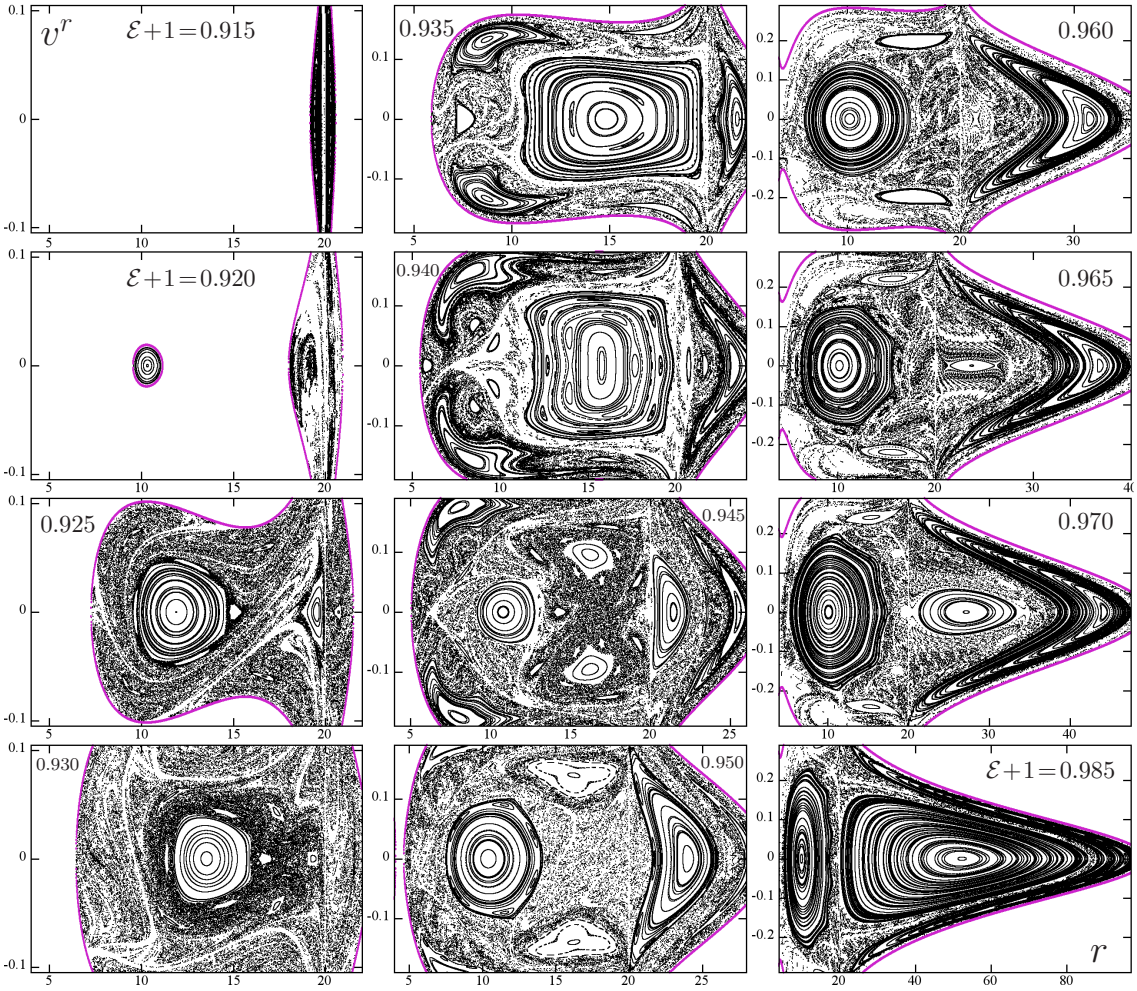

Figure 6.16: The identical series of plots as in figure 6.15 only with the centre simulated by the logarithmic potential (6.3).

get larger for higher energies and dominate the section at $\mathcal{E}(+1) = 0.985$ in all three systems.

6.3.5 Nowak-Wagoner potential

As already stated, the Nowak-Wagoner potential is "too weak" with respect to the centrifugal barrier. As a consequence, when taking the formal parameters of the sections from paper I, the superposition of the Nowak-Wagoner potential with the disc/ring doesn't even have any trajectories with the given parameters and the correspondence is completely broken. Of course, it would be possible to somehow rescale energy or angular momentum to account for this fact but such an approach is against the spirit of the required simplicity of the correspondence and the usual applications of pseudo-Newtonian potentials.

We thus show only a compact excerpt from the Nowak-Wagoner simulations in the form of figure 6.19 in which a part of the perturbing-mass and energy series with the perturbing disc is displayed.

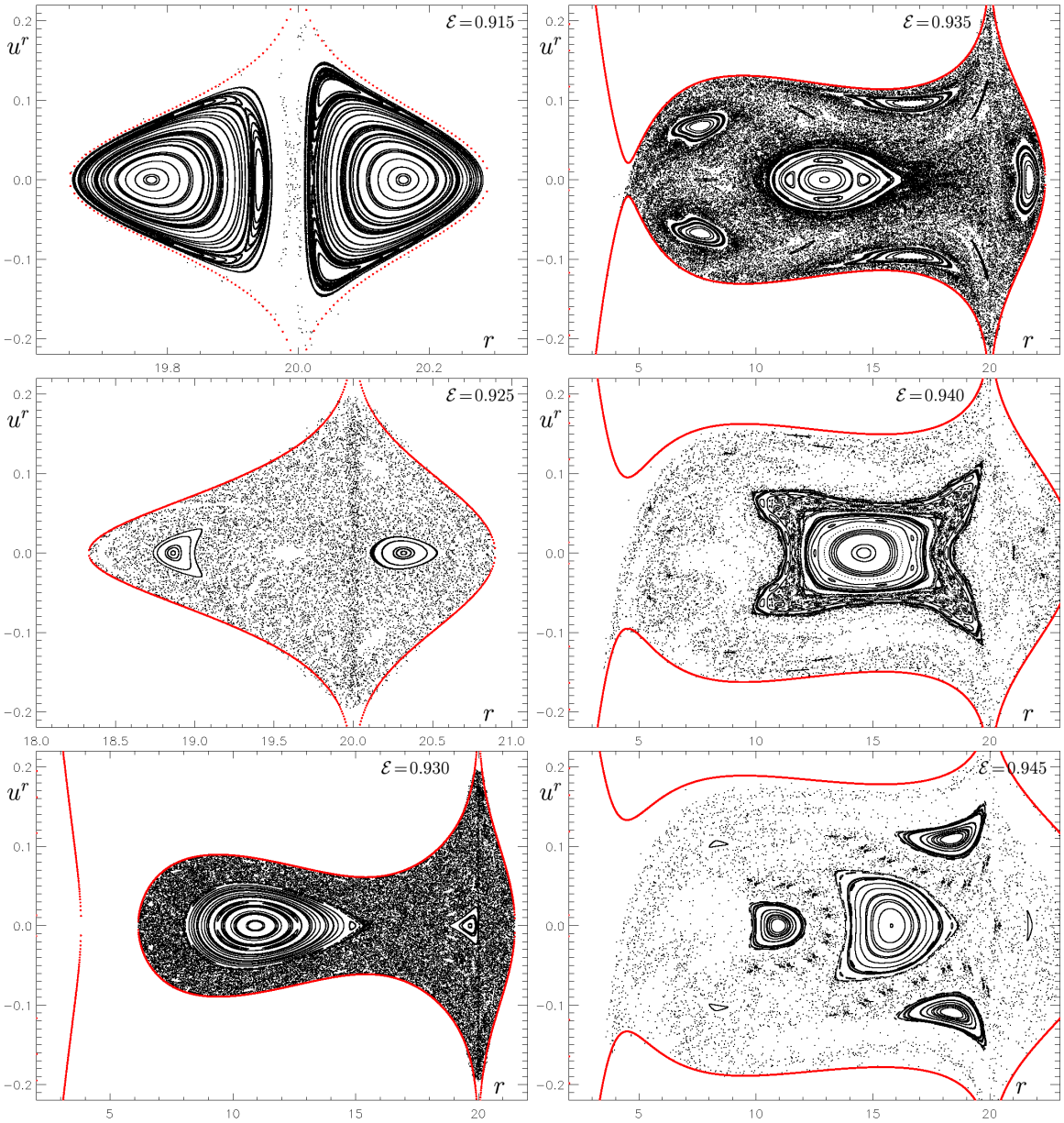

Figure 6.17: The identical series of plots as in figure 6.15 and 6.16 albeit in the exact relativistic framework, with the rest of the energies in figure 6.18. As discussed more extensively in the text, the three systems fall in discord during the transition of the central island over the ring but apart from that share a number of analogies. (Taken from Paper I.)

For the usual $\ell = 3.75M$, $r_{\rm edge} = 20M$, $\mathcal{E}+1 = 0.955$ perturbing mass series a small area of initial conditions appears only for the disc mass larger than $\mathcal{M} \approx 0.7M$. Nevertheless, this small allowed area is created exclusively by the potential well of the disc and the resonant structures or the sequence of bifurcations of the central island have no analogy in the other systems.

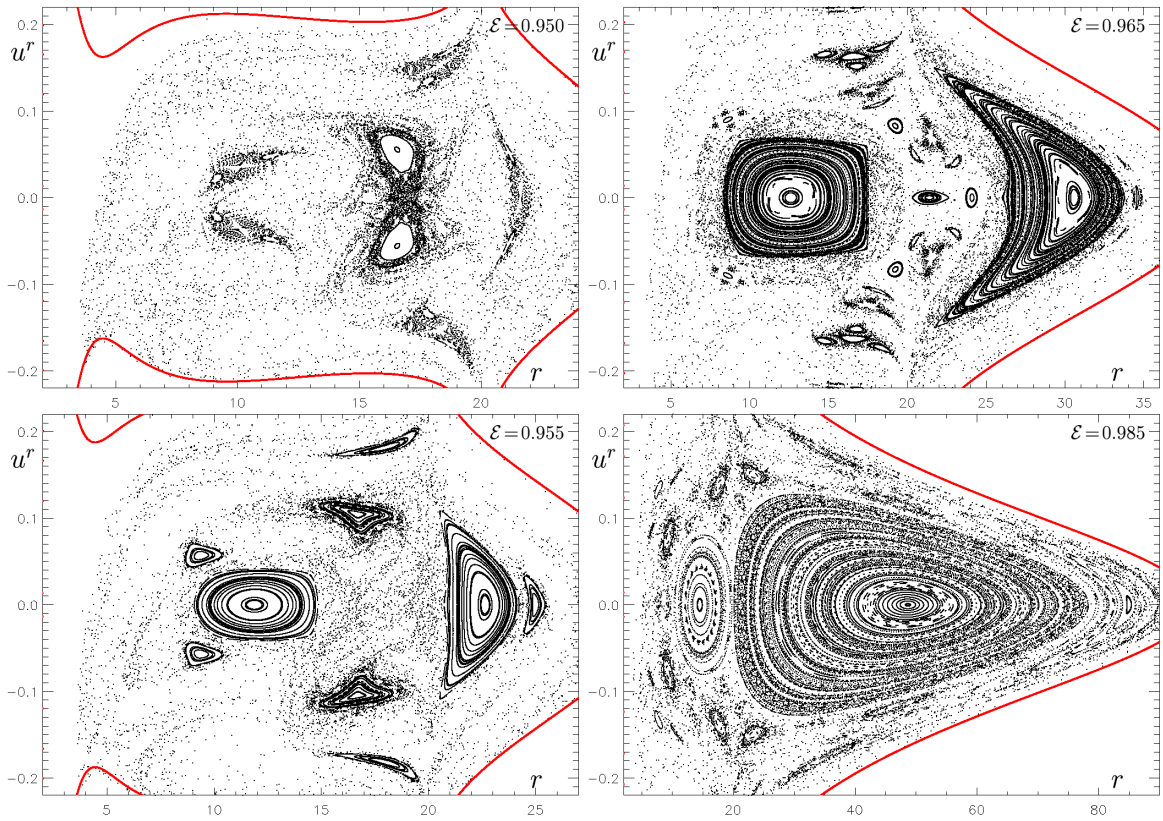

Figure 6.18: A continuation of the "energetic series" of sections from figure 6.17 for the relativistic superposition of a black hole with the BW ring.

For the energetic series under an $\mathcal{M} = 0.5M$ disc perturbation for $\ell = 3.75M$, $r_{\rm edge} = 20M$, the allowed area appears only at $\mathcal{E} + 1 \approx 0.965$ again mostly defined by the disc potential well. Once more, the structure of islands does not resemble the other systems apart from the general structure of a central island plus a chaotic layer with resonances on the periphery of the allowed area.

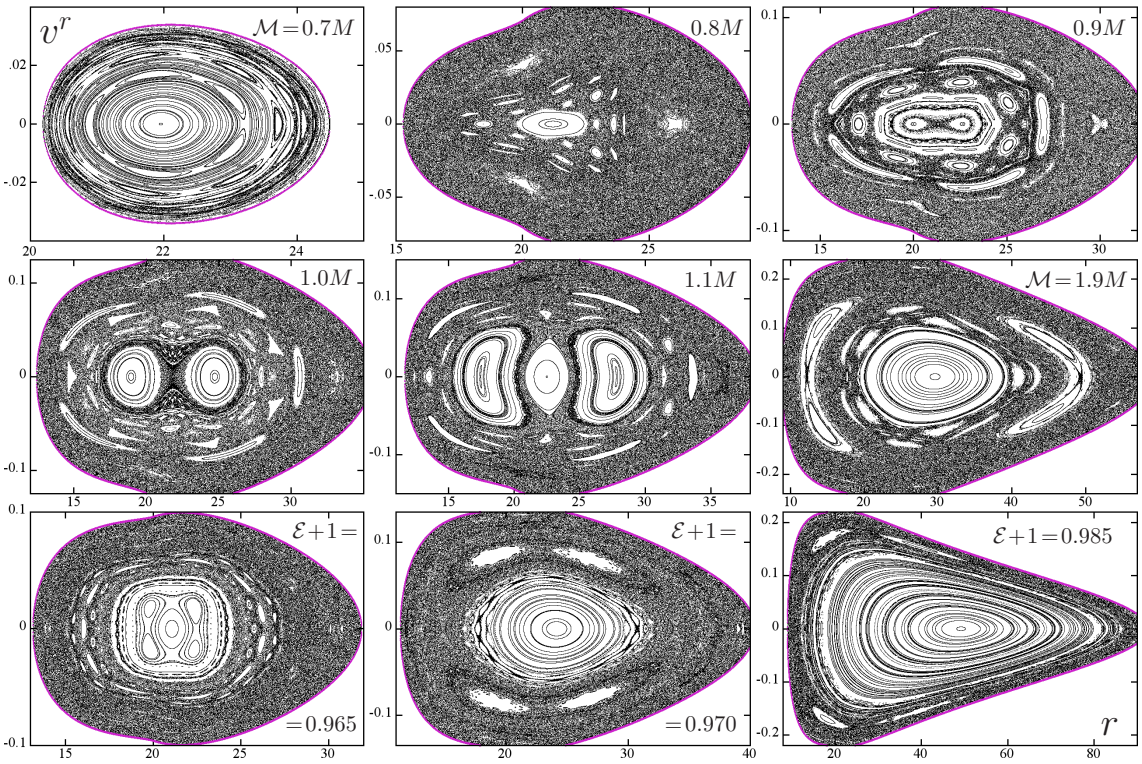

Figure 6.19: Poincaré surfaces of section in the r, v^r variables showing intersections of orbits with angular momentum $\ell = 3.75M$ through the equatorial plane of a centre described by the Nowak-Wagoner potential (with mass M) and surrounded by an iMM1 circumnuclear disc with an inner radius $r_{\rm edge} = 20M$; allowed area is delimited in purple and r axis is in units of M. The first two row show the dependence of the sections on disc-mass $\mathcal{M}$ for particles orbiting at specific energy $\mathcal{E} + 1 = 0.955$. The third row shows only three sections for the $\mathcal{E}$-dependence of the sections, while disc-mass $\mathcal{M}$ is set at $0.5M$. The surfaces of section are so different from the ones for the Paczyński-Wiita or logarithmic potential because the Nowak-Wagoner potential is so "weak" that the observed potential valley is sustained mainly by the superposed disc rather than the centre. This fact also makes the Nowak-Wagoner potential a useful demonstration of "what could go wrong" in a pseudo-Newtonian model.

6.4 Analysis of the orbits

6.4.1 Coordinate shapes

Poincaré surfaces of section are a useful tool in investigating the *overall* structure of the phase space but, in so doing, it necessarily flattens most of the information about individual trajectories. To be able to observe features hidden by the surfaces of section, it is instructive to survey the actual numerical orbits in detail at least in a single surface of section.

Namely, when comparing the surfaces of section of the relativistic vs. Newtonian systems, an

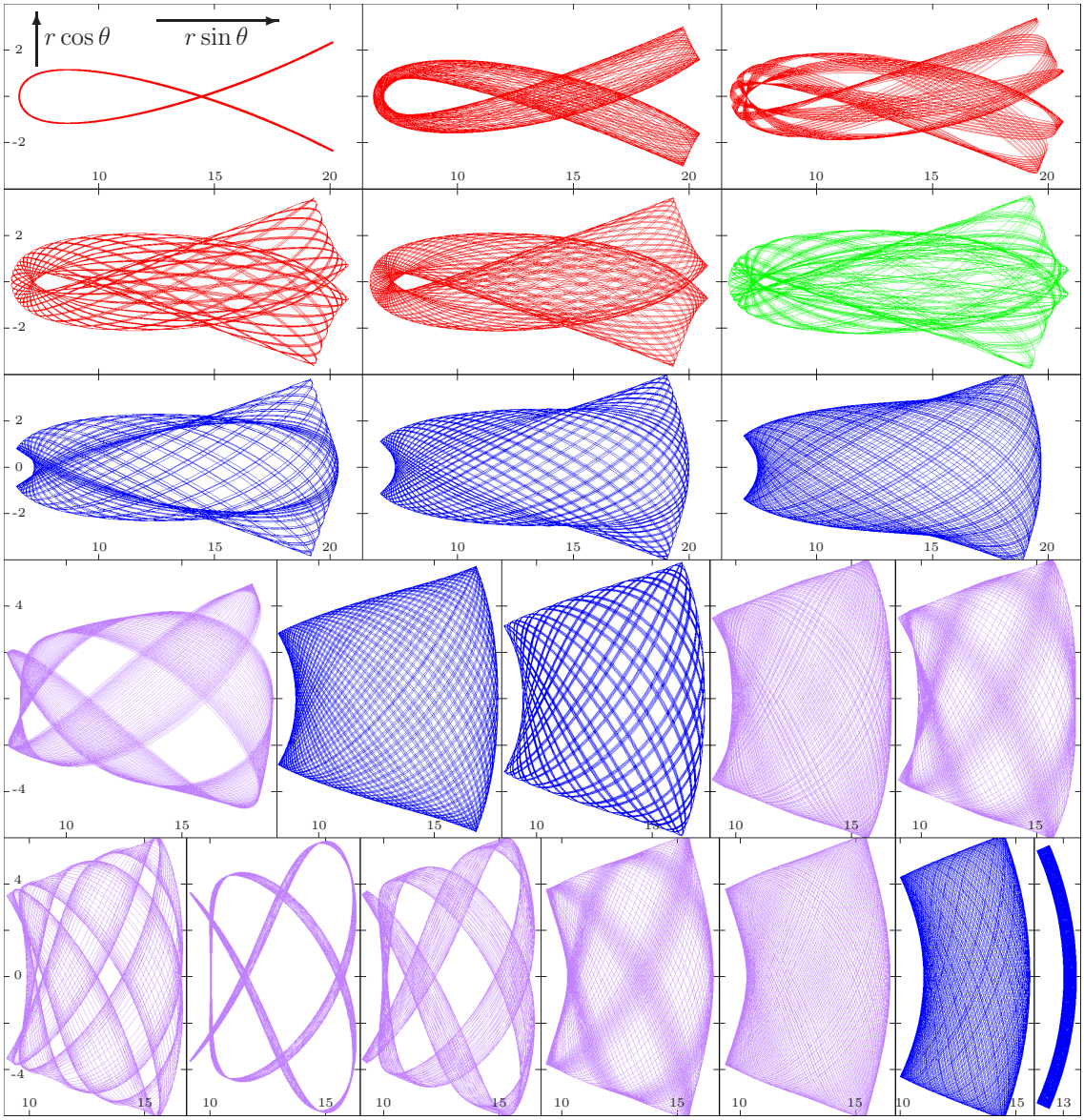

Figure 6.20: A counterpart of fig. 6.21, showing the shapes within the $r\sin\theta$, $r\cos\theta$ plane of the trajectories whose equatorial transitions have been recorded there (in the r, v^r axes). The orbits are plotted up to some 200 intersections with the equatorial plane and are coloured to be easily identifiable in fig. 6.21. From top left to right and bottom, the profile starts from the central orbit of the 3-fold island and proceeds toward the centre of the fig.-6.21 surface of section. All the plots have exactly the same scale, though the coordinate ranges (indicated along the axes in units of M) are adjusted to capture the orbits effectively. Orbits from "more interesting" regions in the central island (near-resonant and resonant) are purple, the single chaotic orbit is green.

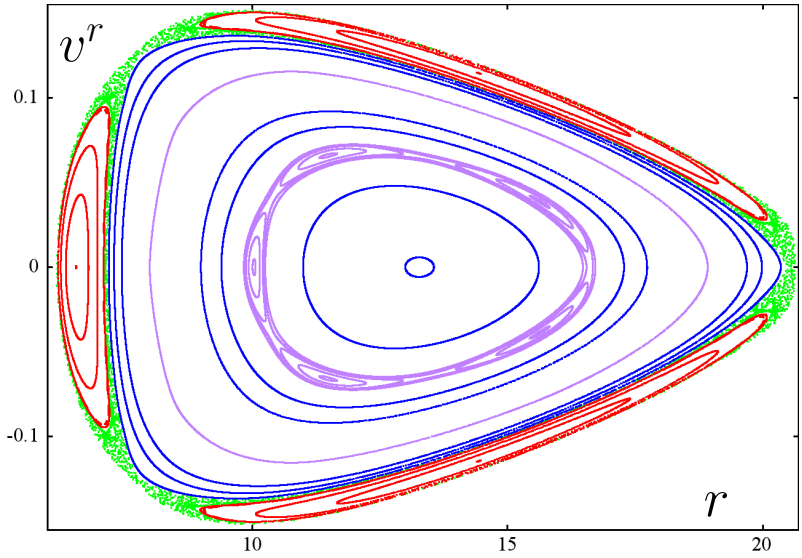

Figure 6.21: The Poincaré surface of section for disc-mass $\mathcal{M} = 0.35M$ from fig. 6.5 revisited with the aim to illustrate what kind of orbits its main structures represent. About 7400 transitions for each orbit was recorded. The orbits are shown in colour to ensure their easy identification against fig. 6.20 where the meridional-plane shapes of their 200 equatorial-intersections are plotted.

n-fold island in one system may correspond to a different resonance than in the other. It is then necessary to plot the orbits of a trajectory in the r, θ plane to be able to read off the ratio of the radial frequency Ω_r and the vertical frequency Ω_θ by comparing the resulting shapes with a set of Lissajous figures (such as in fig. 2.1).

Furthermore, plotting the r, θ coordinate shapes corresponds to a certain projection of physical tracks of an actual body in an idealized astrophysical observation. As a result, by surveying the coordinate tracks one is getting slightly closer to the observational questions of chaos.

Hence, we choose one of the surfaces of section from the disc-mass series of the logarithmic potential (fig. 6.5), specifically the $\mathcal{M} = 0.35M$ section, and present a qualitative catalogue of it's orbits in figure 6.20; the $\mathcal{M} = 0.35M$ case represents the weakest perturbation for which separatrix chaos appears around the chain of three resonant islands. Since only a limited number of orbit shapes is plotted in figure 6.20, the section is replotted in fig. 6.21 with the section-curves corresponding strictly to the orbits in 6.20 with the colours of the intersection-records chosen correspondingly.

There are two distinct resonances in the catalogue (aka fig. 6.20), the "fish-like" 2:3 resonance (red) separated from the central island by a thin separatrix-chaos layer (green), and the 4:5 resonance (purple) near the centre of the island. Additionally, a very thin 3:4 resonance resides halfway between the 2:3 and 4:5 resonance represented only by a single purple near-resonant trajectory, the leftmost one of the fourth row of the catalogue.

It is interesting to note that not only the trajectories in the resonant islands but also the orbits in the vicinity of the resonant islands are deformed into a periodic-like shape. For instance, in the third row of the catalogue we see three trajectories from the central island deformed into the fish-like shape of

the nearby 2:3 resonance.

Even though a deformation of the "envelope" of the orbit shape isn't visible for trajectories near the 4:5 resonance, we can see for the rightmost trajectory in the fourth row and the middle trajectory in the last row that the vicinity of the resonance is reflected in the density of the orbit passage. The mentioned dense spots in the orbit tracks correspond to the vicinity of the unstable periodic orbit, also known as the 5-periodic hyperbolic point in the resonant chain of islands in the Poincaré surface of section.

Drawing on the model resonance introduced in Chapter 1, the near-resonant purple orbits are then analogical to a rotation of a non-linear pendulum very close to a transition to libration. The dense spots correspond to the phase of the pendulum/rotator "on the top", slowing down at near-equilibrium. This analogy also holds against a check of the integration time; from the whole catalogue the near-resonant purple orbits took the longest time to finish 200 intersections of the equatorial plane, most probably because of these "slow-downs" near hyperbolic equilibria.

Let us now turn our attention to the green chaotic orbit. Although it is quite obvious that the orbit is chaotic from the 7200-intersection Poincaré diagram in figure 6.21, it is not all that obvious from the 200-intersection orbit track in the second row of the catalogue. From the short-term coordinate track, the weakly chaotic orbit is virtually indiscernible from the regular ones and even longer records would not provide a very rigorous distinction. One thus must utilize more sophisticated methods such as time-series analysis to discern chaos from order.

6.4.2 Detection of chaos

In this subsection we will only briefly recapitulate the time-series analysis as proposed by Kaplan and Glass (1992) and utilized in Paper IV. The method, originally proposed for deciding whether a time series is random or deterministic, is based on the observation that for an autonomous deterministic system the tangent to a phase-space trajectory is a function of the given point in phase-space (i.e. the tangent is the integrated vector field defining the dynamical system). Hence, tangents passing through an infinitesimal cell in phase space should all have the same tangent (up to infinitesimals).

The second trick used in the analysis is "embedding" a one-dimensional time-series $x(t)$ into a reconstructed phase space by plotting the trajectory alongside delayed coordinates $x(t)$, $x(t-\Delta\tau)$, $x(t-2\Delta\tau)$, ... When the number of dimensions of the reconstructed phase space is sufficient and when the delay $\Delta\tau$ does not hit any characteristic period of the system, the embedded trajectory is equivalent to the original trajectory up to a diffeomorphism (Takens, 1981).

Without further discussion, we state the minimal algorithm of finding a useful overall indicator $\bar{\Lambda}(\Delta\tau)$:

1. The dimension d of delay-embedding is chosen along with time delay $\Delta\tau$ and the size of the phase-space cells over which the average is taken; the cells are indexed by j.

2. Tangents of trajectories crossing the jth box are linearly averaged and the length of the result is found using a suitable norm; the result is denoted as $V_j(\Delta\tau)$

3. The jth box was crossed n_j times, so to obtain a meaningful overall indicator one must compute a particularly weighed average over all the occupied cells

$$\bar{\Lambda}(\Delta\tau) = \left\langle \frac{(V_j(\Delta\tau))^2 - \bar{R}^d_{n_j}}{1 - \bar{R}^d_{n_j}} \right\rangle_j , \tag{6.17}$$

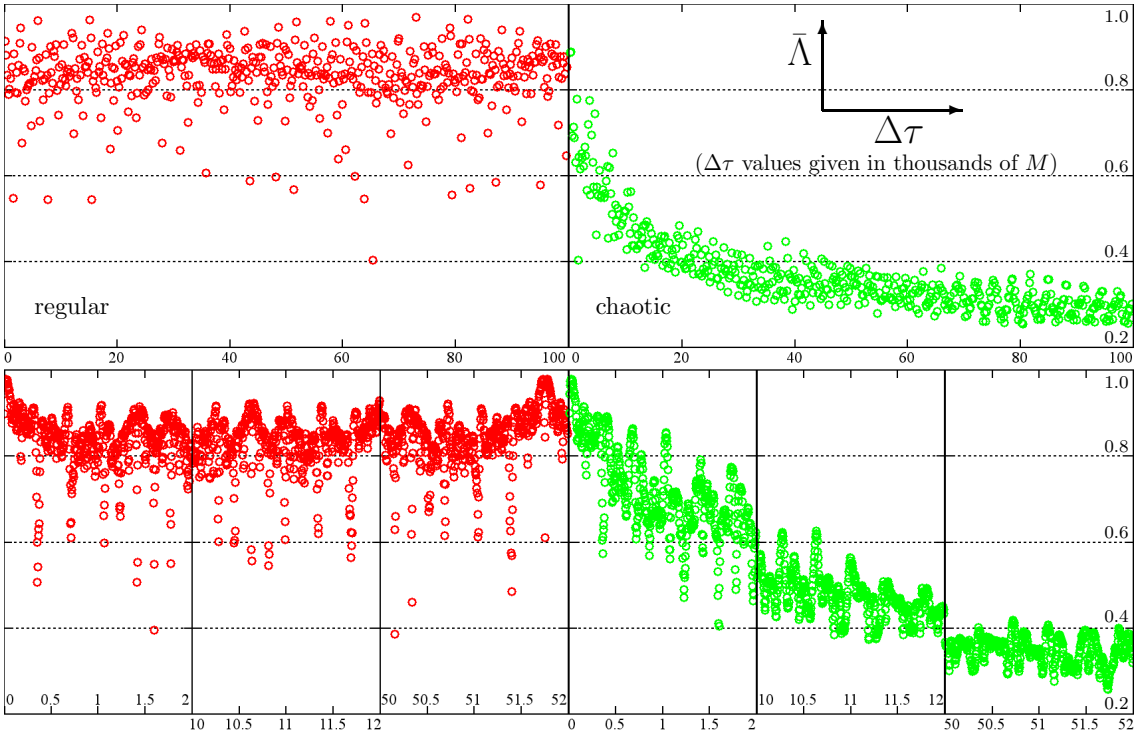

Figure 6.22: Two very close orbits from figure 6.20 (and 6.21), namely the outmost of the red-colour (3-fold) regular ones (left plot) and the green-colour chaotic one (right plot), are clearly distinguishable via the Kaplan-Glass "average directional vectors" recurrence method. The meaning of the $\bar{\Lambda}(\Delta\tau)$ dependence is explained in the main text. Both orbits represent motion of free particles with $E + 1 = 0.955$, $\ell = 3.75M$ in the field of a centre described by the logarithmic potential (mass M) and surrounded by the iMM1 disc with mass $\mathcal{M} = 0.35M$ and inner radius $r_{\rm disc} = 20M$. The orbits have been followed for about $500\,000M$ of proper time (some 5000 equatorial intersections); the top row shows the dependence $\bar{\Lambda}(\Delta\tau)$ from $\Delta\tau = 0$ up to $\Delta\tau = 100\,000M$, while three selected intervals of $\Delta\tau$ are added in more detail in the bottom row (the $\Delta\tau$-axis labels are in thousands of M everywhere).

where $\bar{R}^d_{n_j} \sim n_j^{-1/2}$ is the average displacement per step (for large n_j) for a random walk in d dimensions.

In a theoretical limit of an infinite amount of data and infinitely small cells, $\bar{\Lambda} = 1$ for a deterministic signal and $\bar{\Lambda} = 0$ for a random signal. Obviously, in the case of finite data and a finite grid of phase-space cells, the indicator may work quite differently; it is in fact connected to the autocorrelation function of the time-series with a finite tolerance. In turn, it was shown in Paper II that the dependence $\bar{\Lambda}(\Delta\tau)$ and it's fall-off reveals whether a trajectory is chaotic or regular.

In the currently studied Newtonian system we have computed $\bar{\Lambda}(\Delta\tau)$ for two orbits from figures 6.20 and 6.21; the 2:3 resonant orbit (red) most at the edge of the resonant island and the neighbouring separatrix-chaotic orbit (green). The phase space was reconstructed as three-dimensional (which is

the true dimension of phase space after integral-constraints are applied) from the time-record of the vertical distance from the equatorial plane $r(t)\sin\theta(t)$, and divided into $25^3 = 15625$ cells; the average number of transition through the boxes which were crossed at least once (the average is done only over such boxes) was about $n_j = 50$. The resulting function $\bar{\Lambda}(\Delta\tau)$ for the two chosen trajectories is in figure 6.22.

Depending on the degree of certainty to which the decision between chaotic/regular is needed, the larger the $\Delta\tau$ required. However, at least under the rather idealized assumptions of a system with a minimal degrees of freedom and noiseless data, the characteristic time of discerning chaoticity is certainly in orders of $10^4 M$. For instance, for the black hole at the centre of the Milky way M in terms of time is of orders of seconds. The object on the chaotic trajectory would then need to be monitored for hours, with samples taken every few seconds. Alternatively, of course, the sample could be less dense and the observation time longer. Either way the observation of a sufficient amount of data for the distinction between order and chaos is not unrealistic.

6.4.3 Recurrence analysis

The second method of analysing time-series relies on the analysis of recurrences of the series to a given neighbourhood of a phase-space cell (see Marwan et al. (2007) for an extensive review). In the context of chaos near black holes, the method was already applied in Paper II and in the relativistic context for the first time by Kopáček et al. (2010).

The elementary object of recurrence analysis obtained from a time-series of N points x_i is the $N \times N$ recurrence matrix[4] proposed by Eckmann et al. (1987)

$$R_{ij}(\epsilon) = \Theta(\epsilon - ||x_i - x_j||), \tag{6.18}$$

where $||\cdot||$ is some norm on the generally n-dimensional space of points x_i and $\Theta()$ is the Heaviside step function. From the patterns of diagonals of ones in the recurrence matrix it is possible to read off whether the given time-series is regular, chaotic or stochastic. For instance, a periodic or quasi-periodic time-series will have a large number of long diagonals, and a chaotic system an exotic bent structure of some diagonals, blocks and vertical lines. However, a more sophisticated distinction between order and chaos is obtained by indicators gained from the statistics over the whole recurrence matrix.

Here we only employed several overall indicators obtained from the overall recurrence matrix and used them to document the occurrence of chaoticity/regularity in a whole surface of section. The first employed indicator is "determinism"

$$DET = \frac{\sum_{l=l_{\min}}^{N} l P(l)}{\sum_{i,j}^{N} R_{ij}}, \tag{6.19}$$

where $P(l)$ is the number count of diagonal lines of length l and $l_{\min}$ is a threshold value to cut off a possible fat tail of diagonals in $P(l)$ as $l \to 0$. DET is thus the ratio of the mean diagonal value and the total number of ϵ-recurrences. The second employed indicator is "divergence"

$$DIV = \frac{1}{L_{\max}}, \tag{6.20}$$

[4] Sometimes dubbed the "recurrence plot" but we will not explicitly plot the matrix here.

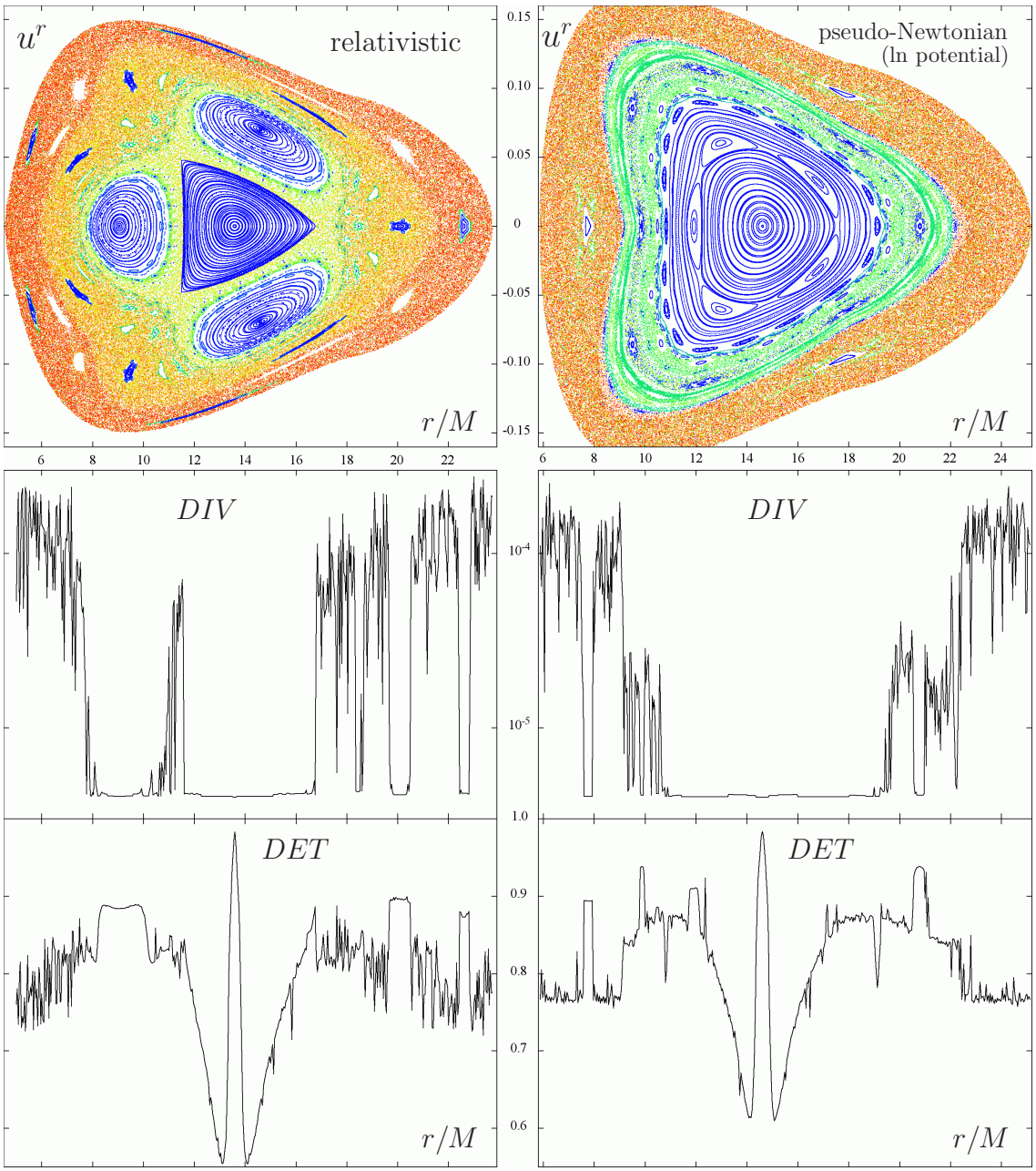

Figure 6.23: Recurrence plot results for a set of orbits with specific energy $\mathcal{E}(+1) = 0.9532$ and angular momentum $\ell = 3.75M$ in the disc-hole fields with the iMM1 disc of mass $\mathcal{M} = 0.5M$ and disc-edge radius $r_{\text{edge}} = 18M$. In the left column, the results for the relativistic superposition are presented, and on the right the results for the Newtonian superposition with the logarithmic potential. A set of orbits with initial $v^r = 0$ or $u^r = 0$ and all the allowed radii in the section was chosen and the indicators DIV and DET were computed to be plotted in dependence on the initial r/M in the second and third row. Additionally, a Poincaré surface of section was created from selected v^r, $u^r = 0$ orbits and the points in the section were coloured according to the DIV indicator (top row). The horizontal axes (r in units of M) are common for all rows and the vertical axes are common for both columns.

where $L_{\max}$ is the maximum length of a diagonal in the recurrence plot. The DIV indicator is related with the so-called Kolmogorov-Sinai entropy (Kolmogorov, 1958; Sinai, 1959) and consequently with the sum of positive Lyapunov exponents of the system.

For the relativistic–pseudo-Newtonian comparison using the recurrence-matrix analysis, we choose fig. 12 of paper II. There, several recurrence quantifiers were computed for 470 geodesics with specific energy $\mathcal{E} = 0.9532$ and specific angular momentum $\ell = 3.75M$, sent vertically from the equatorial plane (with $u^r = 0$) from radii between $r = 5M$ and $r = 24M$ (with step $0.04M$) in the superposition of a black hole (also mass M) and the iMM1 disc with $\mathcal{M} = 0.5M$ and $r_{\rm disc} = 18M$. The orbits were followed for approximately $250\,000M$ of proper time with a sampling period $\Delta\tau = 45M$, the minimal length of diagonal lines has been set at $l_{\min} = 2$ and the radius of the recurrence neighbourhood (the threshold) at $\epsilon = 1.25$. Two of the quantifiers – the most simple DIV and a slightly more sophisticated quantifier estimating the second order Rényi entropy of the system (providing an estimate of the sum of Lyapunov exponents from below) were illustrated by colouring the computed orbits according to their values in the Poincaré diagram. Two main observations were made: i) all the quantifiers proved sensitive to even miniscule phase-space features, and ii) the computationally (and in principle) trivial DIV quantifier proved equally efficient as the more sophisticated one.

The mentioned relativistic recurrence analysis was performed in a six-dimensional phase space (r, θ, ϕ and the respective velocities), while, for the present comparison, we have repeated the analysis for the same set of geodesics in the $(r\sin\theta, r\cos\theta)$ plane plus the respective velocity dimensions only. Even though ϕ cooresponds to an "inactive" (degenerate) degree of freedom, its elimination from the analysis has some interesting aspects.

For instance, note that in the full 3D configuration space there are virtually no true recurrences, since even the most regular central orbit is usually quasi-periodic in ϕ. Within the meridional plane, on the other hand, the core trajectories of resonances do produce true recurrences (see Subsection 6.4.1).

Let us add that the ϕ coordinate can be viewed as a kind of "dynamical memory", because

$$\Delta\phi = \int_{\Delta t} \frac{\ell \, \mathrm{d}t}{r^2 \sin^2\theta} \tag{6.21}$$

(the relativistic formula only contains proper time τ instead of t). Hence, the inclusion of ϕ actually adds non-trivial information, so the change resulting from its elimination might indicate the robustness of various recurrence indicators.

There are several parameters which have to be chosen for recurrence analysis, the already mentioned minimal diagonal was set to $l_{\min} = 3$ and the neighbourhood radius $\epsilon = 0.8$ (with an Euclidean metric used for the distance); the time step of recording the points was chosen as $\Delta\tau = 45M$ and the trajectories were recorded for a total time of about $250000M$ as in Paper II.

An additional parameter is the so-called Theiler window w which is used to eliminate false recurrences which occur simply as a consequence of the fact that x_i and say x_{i+1}, x_{i+2}, ... may be close only due to the slow evolution of the time-series. The Theiler window is then the maximal shift between neighbouring points of the series for which any recurrence is thrown away in the analysis; this parameter was set to $w = 3$.

By comparing fig. 6.23 with figure 12 of Paper II, one can infer that the DIV indicator is not changed by the 3D→2D projection at all, whereas the DET quantifier turned out to be less robust in this respect. Specifically, the DET quantifier seems to wrongly indicate that a large part of the central island is "less deterministic" than the surrounding chaos. To understand this point, it should be recalled that the DET indicator is defined as the ratio of the number of diagonal lines longer

than $l_{\min}$ to the number of all recurrence points. We checked that the orbits in the central island show a large number of recurrence points but, due to the robust quasi-periodicity of the respective trajectories, often not grouped into longer diagonal lines. Hence, the performed normalization with respect to the total number of recurrences turned out to have an undesirable effect of lowering DET for very regular trajectories.

Now to the comparison: we take an analogous pseudo-Newtonian situation, namely the gravitational system with the same formal parameters and with the central black hole simulated by the logarithmic potential. We do not employ the Paczyński–Wiita potential, because for the given parameters it has an accessible region open towards the centre and a long-term time-series analysis of the in-falling (short-lived) chaotic orbits is impossible. The orbits in the system were then subjected to the same recurrence-matrix analysis as performed in fig. 12 of Paper II; the results are given in fig. 6.23. In fig. 6.23, the left column is relativistic and the right column is pseudo-Newtonian (with the logarithmic potential), both plotted in the same scale. Both Poincaré sections are coloured by the inverse of the longest diagonal DIV, whose zero-velocity radial profile throughout the section is also plotted below, and the last row shows another simple quantifier DET, given by ratio of the points which form a diagonal line longer than a certain value within all the recurrence points.

The comparison from figure 6.23 clearly shows that the relativistic and pseudo-Newtonian sections differ in a number of phase-space structures including the degree of stickiness of regular islands, separation of chaotic layers, or multiplicity of resonances. In particular, the biggest difference observable mainly thanks to the colouring is that the relativistic section is stratified by a system of sticky layers (green to orange layers) whereas the Newtonian one has only a rigid invariant barrier ("green chaos" vs. "orange chaos") and no significant stickiness.

Nevertheless, we have already observed in the previous sections of this chapter that the appearance and evolution of various phase-space features can be somewhat shifted in the parameter space, so this difference does not come as a surprise and is not the main concern of the applied recurrence analysis. Rather, the primary motivation of this particular probe is to test whether the structures identified as "same" or "analogous" through Poincaré surfaces of section correspond to the same recurrence patterns. For instance, we are interested whether a relativistic-regular island does show the same characteristics as the Newtonian-regular island, and whether "strong chaos" in both models has approximately the same Lyapunov exponents (as estimated by the DIV indicator). In this respect, there seems to be no radical divergence between the pseudo-Newtonian and the relativistic model.

6.5 Conclusion

We have considered free test particle motion in the field of a black hole superposed with a thin gravitating disc or ring, with the centre simulated by pseudo-Newtonian potentials, and compared the features of families of respective orbits with those in an exact relativistic model. It is obvious that, at least some of the potentials (PW and ln) and at least in the given parameter ranges, the pseudo-Newtonian framework is able to reproduce the relativistic features on a very satisfactory level. However, different methods of analysis would be needed to assess a more "overall" quality of the correspondence.

On the other hand, spending too much time on the relativistic-Newtonian comparison may not be fruitful since the models are either way strongly idealised and no direct conclusions for astrophysics can be drawn from them, at least in their current form. A particular probe, as was given here and in Paper IV, perhaps exposes the problems and strengths of pseudo-Newtonian potentials from the

perspective of phase-space chaotization sufficiently.

The possible direction in which the models could be developed is to adapt them to more directly represent real situations in celestial mechanics. A simplest implementation of this program would be to add other gravitating components such as a jet or a halo of stars. Second, the gravitating sources would have to be extended to be 3D (non-singular) sources, unless they are considered only as effective "far-away" approximations and their singularities well avoided by the trajectories.

Once a sufficiently realistic description is obtained, one should start to look for consequences for observational phenomena. For example, the ensembles of trajectories in surfaces of section could be understood as *actual* collision-less ensembles orbiting the black hole. The large resonant structures could then have consequences for the typical oscillation spectra of such clouds or for the shape and long-term equilibria when an adiabatic evolution of the ensemble is introduced.

There are also technically very difficult aspects of the model such as the fact that for realistic astrophysical situations the black hole should be a spinning black hole described by a Kerr metric metric deformed by some external matter sources. Such realistic solutions are, however, unknown.

Concluding remarks

In light of the presented results and the review in Section 2.1, we see that the usefulness of Poincaré surface of section is limited. This historical method can satisfactorily document the perturbation of a dynamical system with one degree of freedom under time-dependent perturbation[5] (e.g. the kicked non-linear oscillators). In such a case, the system can be chosen to have a single parameter which defines a family of surfaces of sections from which clear and concise conclusions can be drawn. However, once a system with two non-degenerate degrees of freedom is perturbed, the Poincaré surfaces of section are necessarily parametrized by an additional energy parameter (conserved Hamiltonian).[6] Furthermore, if we are interested in a system which has merely "effectively" two degrees of freedom, while in fact three, then the Poincaré surfaces of section have *at least* three parameters, corresponding to energy, the integral of motion corresponding to the dynamically degenerate "third" degree of freedom, and the perturbation-strength parameter.

In our case the parameters were, in fact, four; the parameters due to extra degrees of freedom were $\mathcal{E}$, ℓ and the perturbation parameters $r_{\mathrm{ring,edge}}, \mathcal{M}$ ($\mathcal{M}$ being a natural "perturbation-strength" parameter and $r_{\mathrm{ring,edge}}$ an "internal" parameter of the observation). Observing a certain "slice" from the parameter space may then be interesting as a "first run-through" of the dynamics but not conclusive for the system as whole.

Additional problems plaguing the study of systems with more than one degree of freedom is that the perturbation parameters along with the fixing of integrals of motion $\mathcal{E}, \ell$ *deforms the set of initial conditions studied* (see Subsec. 6.3.3). In the Newtonian case the deformation could be approximately compensated by a shift in the specific energy $\mathcal{E}$ but in the relativistic case the perturbation also changes the connection between angular momentum $\ell = g_{\phi\phi}u^{\phi}$ and the physical proper velocity $u^{\phi} = \mathrm{d}\phi/\mathrm{d}\tau$.[7] As a result, the real influence of the perturbation on the ensemble of physical trajectories is probably impossible to clearly discern from the series of surfaces of section.

Obviously, for the papers published in the field some twenty years ago any other method than Poincaré surfaces of section would be computationally unfeasible. On the other hand, some of the rather ridiculous controversies as presented in Section 2.1 would be non-existent if more sophisticated "overall" methods had been available. The current computational possibilities have increased manifold and the numerical analysis of Hamiltonian chaos needs to reach a new stage: "Statistical" methods mapping the whole parameter space are needed. Also, the case for more sophisticated methods is strengthened by the fact that Poincaré surfaces of section are mostly useless for systems where chaos is happening in a dimension higher than 3, such as those with broken axial symmetry or for the motion of extended physical bodies with spin, and effectively quadrupolar or octupolar internal degrees of freedom. Without effective methods of analysis for such systems, studies of chaos in

[5] The fact is that it would suffice for it to be characterized by two canonically conjugate coordinates I, ϑ such that the unperturbed Hamiltonian is linear in I (which leads to $\dot{\vartheta} = \text{const.}$) and the perturbation is only dependent on ϑ. However, this case can always be turned into an I, ϑ-independent system perturbed by a time-dependent term.

[6] The trick in the case of the time-dependent perturbation is that, due to the particular degeneracy, the integral of motion $i = 1$ is the same for all trajectories.

[7] Alternatively, the change in ν changes the strength of the centrifugal barrier $\sim g^{\phi\phi}\ell^2/2$.

orbital dynamics cannot achieve physical significance.

Even so, such a discussion leads us inadvertently to the hard question of relativistic chaos: What are the properties we want to document about the studied dynamical system? What and why should we distill from the ensemble of possible orbits? Surely, the minimal goal is to show whether or not the studied evolution is fully integrable, but without additional physical motivation for a more detailed study this would be a trivial task.

There are a number of possible applications of orbital chaos in astronomy and astrophysics but apart from direct Solar-system observations none of these have been developed into a sharp prediction for astrophysical observations. Apostolatos et al. (2009) proposed that non-Kerr space-times could be detected by observing gravitational waves emitted by orbits passing through resonances in the phase-space, a point which was later elaborated upon by Flanagan and Hinderer (2012) and Brink et al. (2015b,a). However, there seems to be no agreement on what kind of physical effect (or a hierarchy of effects) should be responsible for the resonance, and thus no direct observational predictions were given to date. A related thread of research follows the proposal of Levin (2000) that chaos occurs in the case of an inspiral of compact binaries with spin (see also resurvey by Wu and Xie (2008)).

Resonances could also be linked to the observed quasi-periodic oscillations (QPOs) in the luminosity of various X-ray sources (see e.g. the review of Remillard and McClintock (2006)). This is because the power spectra of these oscillations exhibit peaks at integer-ratio frequencies very much similar to power spectra of resonant trajectories (see Paper II). It was first proposed by Kluźniak and Abramowicz (2001) that orbital resonance in an excitation of a near-Keplerian disc is responsible for the QPOs and since then various implementations were presented (Kluźniak and Abramowicz, 2001; Abramowicz et al., 2003; Schnittman and Bertschinger, 2004; Török et al., 2005). However, the accretion disc physics are very complicated and it is hard to draw hard conclusions from these models.

Alternatively, chaos could also be a reason of heightened accretion or rather black-hole infall rates (see the Newtonian disc-centre model of Vokrouhlický and Karas (1998)). Since the chain of resonances is also associated with a thin layer of chaos, a very particular observational signature of the chaos-induced in-falls would most probably be "resonant gaps" in orbiter population very much similar to the famous Kirkwood gaps in the distribution of main-belt asteroids caused by orbital resonance with Jupiter.

Nevertheless, all of these conjectured applications are beyond the scope of the current thesis. Even though this Master thesis set out to study chaos near black holes in general, its notable original scientific contribution lies in the testing and development of the pseudo-Newtonian framework. In particular, the study of the pseudo-Newtonian limit in Chapter 3 is not finished and could turn out a useful tool both for simulations near a spinning black hole and for null geodesics.

On the other hand, the "logarithmic" pseudo-Newtonian potential introduced in Chapter 6 is certainly comparable and in some aspects better than the "benchmark" Paczyński-Wiita potential, at least for bound motion. The only question is whether classical velocity-independent potentials for non-spinning black holes are still relevant for contemporary astrophysical simulations; the importance of the logarithmic potential would be higher some thirty years ago.

Bibliography

Abramowicz, M. A. and Fragile, P. C. (2013). Foundations of black hole accretion disk theory. *Living Rev. Relat.*, 16(1).

Abramowicz, M. A., Karas, V., Kluźniak, W., Lee, W. H., and Rebusco, P. (2003). Non-linear resonance in nearly geodesic motion in low-mass x-ray binaries. *PASJ*, 55(2):467–471.

Alligood, K., Sauer, T., and Yorke, J. (1997). *Chaos: An Introduction to Dynamical Systems*. Springer.

Apostolatos, T. A., Lukes-Gerakopoulos, G., and Contopoulos, G. (2009). How to observe a non-Kerr spacetime using gravitational waves. *Physical Rev. Lett.*, 103(11):111101.

Arnold, V. I. (1989). *Mathematical methods of classical mechanics*. Springer Science & Business Media.

Arnold, V. I., Kozlov, V. V., and Neishtadt, A. I. (2007). *Mathematical aspects of classical and celestial mechanics*. Springer Science & Business Media.

Artemova, I. V., Björnsson, G., and Novikov, I. D. (1996). Modified Newtonian potentials for the description of relativistic effects in accretion disks around black holes. *ApJ*, 461:565.

Bendixson, I. (1901). Sur les courbes définies par des équations différentielles. *Acta Math.*, 24(1):1–88.

Benettin, G. and Giorgilli, A. (1994). On the Hamiltonian interpolation of near-to-the identity symplectic mappings with application to symplectic integration algorithms. *J. Stat. Phys.*, 74(5-6):1117–1143.

Blanes, S. and Moan, P. (2002). Practical symplectic partitioned Runge–Kutta and Runge–Kutta–Nyström methods. *J. Comput. Appl. Math.*, 142(2):313–330.

Brink, J., Geyer, M., and Hinderer, T. (2015a). Astrophysics of resonant orbits in the Kerr metric. *Phys. Rev. D*, 91(8):083001.

Brink, J., Geyer, M., and Hinderer, T. (2015b). Orbital resonances around black holes. *Phys. Rev. Lett.*, 114(8):081102.

Chandrasekhar, S. (1998). *The mathematical theory of black holes*. Oxford University Press.

Chen, J. and Wang, Y. (2003). Chaotic dynamics of a test particle around a gravitational field with a dipole. *Class. Quantum Grav.*, 20(18):3897.

Contopoulos, G. (2002). *Order and chaos in dynamical astronomy*. Springer Science & Business Media.

Contopoulos, G., Lukes-Gerakopoulos, G., and Apostolatos, T. (2011). Orbits in a non-Kerr dynamical system. *IJBC*, 21(08):2261–2277.

Crispino, L. C., da Cruz Filho, J. L., and Letelier, P. S. (2011). Pseudo-Newtonian potentials and the radiation emitted by a source swirling around a stellar object. *Phys. Lett. B*, 697(5):506–511.

Dawes, B., Abrahams, D., and Rivera, R. (2014). BOOST libraries. `boost.org`. Version 1.57.0 (November 3rd, 2014).

de Moura, A. P. and Letelier, P. S. (2000). Chaos and fractals in geodesic motions around a nonrotating black hole with halos. *Phys. Rev. E*, 61(6):6506.

Dubeibe, F., Pachón, L. A., and Sanabria-Gómez, J. D. (2007). Chaotic dynamics around astrophysical objects with nonisotropic stresses. *Phys. Rev. D*, 75(2):023008.

Eckmann, J.-P., Kamphorst, S. O., and Ruelle, D. (1987). Recurrence plots of dynamical systems. *Europhys. Lett*, 4(9):973–977.

Flanagan, E. E. and Hinderer, T. (2012). Transient resonances in the inspirals of point particles into black holes. *Physical Rev. Lett.*, 109(7):071102.

Ghosh, S., Sarkar, T., and Bhadra, A. (2014). Newtonian analogue of corresponding space–time dynamics of rotating black holes: implications for black hole accretion. *Mon. Not. R. Astron. Soc.*, 445(4):4463–4479.

Guckenheimer, J. and Holmes, P. (1983). *Nonlinear oscillations, dynamical systems, and bifurcations of vector fields*. Springer Science & Business Media.

Guéron, E. and Letelier, P. (2001). Chaos in pseudo-Newtonian black holes with halos. *Astron. Astroph.*, 368(2):716–720.

Guéron, E. and Letelier, P. S. (2002). Geodesic chaos around quadrupolar deformed centers of attraction. *Phys. Rev. E*, 66(4):046611.

Hairer, E. and Lubich, C. (2000). Long-time energy conservation of numerical methods for oscillatory differential equations. *SIAM J. Numer. Anal.*, 38(2):414–441.

Hairer, E., Lubich, C., and Wanner, G. (2006). *Geometric Numerical Integration: Structure-Preserving Algorithms for Ordinary Differential Equations*. Springer Series in Computational Mathematics. Springer Berlin Heidelberg.

Hairer, E. and Söderlind, G. (2005). Explicit, time reversible, adaptive step size control. *SIAM J. Sci. Comput.*, 26(6):1838–1851.

Haller, G. (2012). *Chaos Near Resonance*. Applied Mathematical Sciences. Springer New York.

Han, W.-B. (2008). Revised research about chaotic dynamics in Manko et al. spacetime. *Phys. Rev. D*, 77(12):123007.

Hirsch, M., Smale, S., and Devaney, R. (2004). *Differential Equations, Dynamical Systems, and an Introduction to Chaos*. Academic Press.

Iserles, A. (2009). *A first course in the numerical analysis of differential equations*. Cambridge University Press.

Kaplan, D. T. and Glass, L. (1992). Direct test for determinism in a time series. *Phys. Rev. Lett.*, 68(4):427.

Karas, V. and Vokrouhlický, D. (1992). Chaotic motion of test particles in the Ernst space-time. *Gen. Relat. Grav.*, 24(7):729–743.

Kluźniak, W. and Abramowicz, M. A. (2001). The physics of kHz QPOs—strong gravity's coupled anharmonic oscillators. *arXiv preprint astro-ph/0105057*.

Kolmogorov, A. N. (1958). A new metric invariant of transient dynamical systems and automorphisms in Lebesgue spaces. volume 119 of *Dokl. Akad. Nauk SSSR*, pages 861–864.

Kopáček, O. and Karas, V. (2014). Inducing chaos by breaking axial symmetry in a black hole magnetosphere. *Astrophys. J.*, 787(2):117.

Kopáček, O., Karas, V., Kovář, J., and Stuchlík, Z. (2010). Transition from regular to chaotic circulation in magnetized coronae near compact objects. *Astrophys. J.*, 722(2):1240.

Kovář, J., Kopáček, O., Karas, V., and Kojima, Y. (2013). Regular and chaotic orbits near a massive magnetic dipole. *Class. Quantum Grav.*, 30(2):025010.

Lemos, J. P. and Letelier, P. S. (1994). Exact general relativistic thin disks around black holes. *Phys. Rev. D*, 49(10):5135.

Letelier, P. and Vieira, W. (1997). Chaos and rotating black holes with halos. *Phys. Rev. D*, 56(12):8095.

Letelier, P. and Vieira, W. (1998). Chaos and Taub-NUT related spacetimes. *Phys. Lett. A*, 244(5):324–328.

Levin, J. (2000). Gravity waves, chaos, and spinning compact binaries. *Phys. Rev. Lett.*, 84(16):3515.

Lowenstein, J. H. (2012). *Essentials of Hamiltonian Dynamics*. Cambridge University Press.

Lukes-Gerakopoulos, G. (2012). Nonintegrability of the Zipoy-Voorhees metric. *Phys. Rev. D*, 86(4):044013.

MacKay, R., Meiss, J., and Percival, I. (1984). Transport in Hamiltonian systems. *Physica D*, 13(1):55–81.

Marwan, N., Romano, M. C., Thiel, M., and Kurths, J. (2007). Recurrence plots for the analysis of complex systems. *Phys. Rep.*, 438(5):237–329.

Miller Jr, W., Post, S., and Winternitz, P. (2013). Classical and quantum superintegrability with applications. *J. Phys. A*, 46(42):423001.

Morgan, T. and Morgan, L. (1969). The gravitational field of a disk. *Phys. Rev.*, 183(5):1097.

Nakamura, Y. and Ishizuka, T. (1993). Motion of a charged particle around a black hole permeated by magnetic field and its chaotic characters. *Astrophys. Space Sci.*, 210(1):105–108.

Novikov, I. and Thorne, K. (1973). Astrophysics of black holes. In *Black Holes (Les Astres Occlus)*, volume 1, pages 343–450.

Nowak, M. A. and Wagoner, R. V. (1991). Diskoseismology: Probing accretion disks. I-trapped adiabatic oscillations. *ApJ*, 378:656–664.

Paczyński, B. and Wiita, P. J. (1980). Thick accretion disks and supercritical luminosities. *Astron. Astroph.*, 88:23–31.

Percival, I. C. (1980). Variational principles for invariant tori and cantori. volume 57 of *JPCS*, pages 302–310.

Poincaré, H. (1899). Les méthodes nouvelles de la méchanique céleste. *Paris: Gauthier-Villars, 1892, 1893,| c1899*, 1.

Remillard, R. A. and McClintock, J. E. (2006). X-ray properties of black-hole binaries. *Annu. Rev. Astron. Astrophys.*, 44:49–92.

Saa, A. (2000). Chaos around the superposition of a monopole and a thick disk. *Phys. Lett. A*, 269(4):204–208.

Saa, A. and Venegeroles, R. (1999). Chaos around the superposition of a black-hole and a thin disk. *Phys. Lett. A*, 259(3):201–206.

Šácha, J. and Semerák, O. (2005). Toroidal source around a static black hole. *Czechosl. J. Phys.*, 55(2):139–155.

Schnittman, J. D. and Bertschinger, E. (2004). The harmonic structure of high-frequency quasi-periodic oscillations in accreting black holes. *Astrophys. J.*, 606(2):1098.

Semerák, O. and Suková, P. (2010). Free motion around black holes with discs or rings: between integrability and chaos–I. *Mon. Not. R. Astron. Soc.*, 404(2):545–574.

Semerák, O. and Suková, P. (2012). Free motion around black holes with discs or rings: between integrability and chaos–II. *Mon. Not. R. Astron. Soc.*, 425(4):2455–2476.

Semerák, O., Žáček, M., and Zellerin, T. (1999a). Test-particle motion in superposed Weyl fields. *Mon. Not. R. Astron. Soc.*, 308(3):705–717.

Semerák, O., Zellerin, T., and Žáček, M. (1999b). The structure of superposed Weyl fields. *Mon. Not. R. Astron. Soc.*, 308(3):691–704.

Semerák, O. (2015). Approximating light rays in the Schwarzschild field. *ApJ*, 800(1):77.

Seyrich, J. and Lukes-Gerakopoulos, G. (2012). Symmetric integrator for nonintegrable Hamiltonian relativistic systems. *Phys. Rev. D*, 86(12):124013.

Shakura, N. and Sunyaev, R. (1973). Black holes in binary systems. observational appearance. *Astron. & Astrophys.*, 24:337–355.

Shlesinger, M. F., Zaslavsky, G. M., and Klafter, J. (1993). Strange kinetics. *Nature*, 363(6424):31–37.

Sinai, Y. G. (1959). On the concept of entropy of a dynamical system. volume 124 of *Dokl. Akad. Nauk. SSSR*, pages 768–771.

Stoffer, D. (1995). Variable steps for reversible integration methods. *Computing*, 55(1):1–22.

Suková, P. (2009). *Chaos v pohybu kolem černých děr*. Master thesis, Charles University in Prague.

Suková, P. and Semerák, O. (2013). Free motion around black holes with discs or rings: between integrability and chaos–III. *Mon. Not. R. Astron. Soc.*, 436(2):978–996.

Takahashi, M. and Koyama, H. (2009). Chaotic motion of charged particles in an electromagnetic field surrounding a rotating black hole. *Astrophys. J.*, 693(1):472.

Takens, F. (1981). *Detecting strange attractors in turbulence*. Springer.

Tejeda, E. and Rosswog, S. (2013). An accurate Newtonian description of particle motion around a Schwarzschild black hole. *Mon. Not. R. Astron. Soc.*, 433(3):1930–1940.

Tejeda, E. and Rosswog, S. (2014). Generalized Newtonian description of particle motion in spherically symmetric spacetimes. *arXiv preprint, arXiv:1402.1171*.

Török, G., Abramowicz, M. A., Kluźniak, W., and Stuchlík, Z. (2005). The orbital resonance model for twin peak kHz quasi periodic oscillations in microquasars. *Astron. Astrophys.*, 436(1):1–8.

Vieira, W. M. and Letelier, P. S. (1996). Chaos around a Hénon-Heiles-inspired exact perturbation of a black hole. *Physical Rev. Lett.*, 76(9):1409.

Vieira, W. M. and Letelier, P. S. (1997). On the integrability of halo dipoles in gravity. *Phys. Lett. A*, 228:22–24.

Vieira, W. M. and Letelier, P. S. (1999). Relativistic and Newtonian core-shell models: analytical and numerical results. *Astrophys. J.*, 513(1):383.

Vokrouhlický, D. and Karas, V. (1998). Stellar dynamics in a galactic centre surrounded by a massive accretion disc—I. Newtonian description. *Mon. Not. R. Astron. Soc.*, 298(1):53–66.

Wegg, C. (2012). Pseudo-Newtonian potentials for nearly parabolic orbits. *ApJ*, 749(2):183.

Weyl, H. and Bach, R. (1922). Nene lösungen der einsteinschen gravitationsgleighungen. *Math. Z*, 13(13):119–142.

Witzany, V. (2013). *Chaos in Perturbed Black-Hole Fields*. Bachellor thesis, Charles University in Prague.

Witzany, V., Semerák, O., and Suková, P. (2015). Free motion around black holes with discs or rings: between integrability and chaos – IV. *Mon. Not. R. Astron. Soc.*, 451(2):1770–1794.

Wu, X. and Xie, Y. (2008). Resurvey of order and chaos in spinning compact binaries. *Phys. Rev. D*, 77(10):103012.

Wu, X. and Zhang, H. (2006). Chaotic dynamics in a superposed Weyl spacetime. *Astrophys. J.*, 652(2):1466.

Yoshida, H. (1990). Construction of higher order symplectic integrators. *Phys. Lett. A*, 150(5):262–268.

Zaslavsky, G. M. (2008). *Hamiltonian chaos and fractional dynamics*. Oxford Univ. Press.